

MOLECULAR AND PHYSICOCHEMICAL CHARACTERIZATION OF AEROSOLS  
RELEVANT TO THEIR ATMOSPHERIC FORMATION AND GROWTH

A Dissertation

by

MARIO ESTUARDO GÓMEZ HERNÁNDEZ

Submitted to the Office of Graduate and Professional Studies of  
Texas A&M University  
in partial fulfillment of the requirements for the degree of

DOCTOR OF PHILOSOPHY

Chair of Committee,	Renyi Zhang
Committee Members,	Donald R. Collins
	Simon North
	Emile Schweikert
Head of Department,	Francois Gabbai

December 2015

Major Subject: Chemistry

Copyright 2015 Mario Estuardo Gómez Hernández

## ABSTRACT

This dissertation is aimed at understanding the molecular composition and physical chemistry of secondary organic aerosols (SOA) and, in particular, the processes that lead to their formation and growth. Several analytical and experimental methods have been developed and employed to characterize the chemical composition of nano- to sub-micrometer-sized particles and to obtain kinetic data and physiochemical properties of SOA. The first part of this dissertation describes the development, calibration, and application of Thermal Desorption Chemical Ionization Ion Drift Mass Spectrometry (TD-ID-CIMS) designed for the collection and chemical analysis of nucleation to accumulation mode aerosols with sizes between 2 and 200 nm. The TD-ID-CIMS instrument has been applied to the analysis of collected nano- to sub-micrometer-sized aerosol samples or injected bulk solutions.

The uptake coefficient ( $\gamma$ ) and the Henry's law constant ( $H^*$ ) for the heterogeneous reaction of gas-phase glyoxal on liquid sulfuric acid surfaces have been obtained using a laminar flow reactor coupled to ion drift – chemical ionization mass spectrometry (ID-CIMS) detection. The results show that both the uptake coefficient and Henry's law constant increase with decreasing acid concentration and temperature, indicating a reaction mechanism of hydration followed by oligomerization for glyoxal on acidic media and suggesting an efficient aqueous reaction of glyoxal on hygroscopic particles leading to SOA formation.

The hygroscopicity, deliquescence, and cloud condensation nuclei activity of several alkylammonium carboxylate aerosols with sizes between 46 and 151 nm have been measured using a Hygroscopicity Tandem Differential Mobility Analyser (H-TDMA), a Condensation Particle Counter (CPC) and a Cloud Condensation Nuclei counter (CCN). Our results indicate that, dependent of their molecular functionality, alkylammonium carboxylate aerosols exhibit distinct hygroscopic, CCN, and deliquescent characteristics.

Finally, the heterogeneous conversion of sulfur dioxide to sulfate in the presence of gaseous nitrogen dioxide and ammonia has been investigated to evaluate sulfate formation under polluted environments. Experiments were performed utilizing a 1 m<sup>3</sup> chamber connected to a TDMA-CPC assembly and the TD-ID-CIMS instrument. Our results show that the extent of sulfate formation and particle growth is dependent on the gas concentrations of SO<sub>2</sub>, NO<sub>2</sub>, and NH<sub>3</sub>, but not sensitive to light. The results may lead to a better understanding of the formation of haze in polluted environments.

## DEDICATION

To God the Father from whom all blessings flow!

To Christ, redeemer of my soul!

To the Parakletos, comforter of my spirit!

To my parents, Hugo and Miriam for believing in me, and in my dreams.

To Hugo Eliseo, Gabriel Isaac and Christa Sofia, my best friends.

To my grandparents, Mario and Rosario, Eliseo (RIP) and Estela.

To the Presbyterian Church in the United States of America.

To my home country, Guatemala

To my host country, land of opportunity, The United States of America

And

To my wife Heydi Masiel, my better half!

## ACKNOWLEDGEMENTS

First and foremost, I would like to thank my dissertation, research, and career advisor Dr. Renyi Zhang. It has been a privilege to work with someone who is a gentleman, a scholar, a mentor, an inspiration, and a role model. I will never be able to thank Dr. Zhang enough for giving me the opportunity to join his research group. In his laboratory, I could conduct high impact research with global implications, and turn my career in the right direction. His exemplary work ethic, motivation, drive, intensity, and generosity will be my standard of performance in the years to come. Thank you Boss!

I would also like to thank past and present members of my dissertation committee: Dr. John Bevan, Dr. Sarah Brooks, Dr. Emile Schweikert, Dr. Simon North and Dr. Donald R. Collins. Their expertise, guidance, and advice are true reflections of the quality and spirit of the faculty at Texas A&M University. It has been an honor to have them in my dissertation committee. I must also thank Dr. Alexei Khalizov, a colleague and a friend who always had advice and technical insight regarding research challenges and scientific questions. I must also thank Dr. Donald R. Collins and the members of his research lab for sharing his research equipment and expertise with me for extended periods of time. I could not have completed two chapters of my dissertation without the advanced equipment that Dr. Collins graciously let me use without time limits. In that regard, Nathan Taylor and Chance Spencer were both instrumental in teaching me how to set up the instruments. I must also thank past and present members of Dr. Zhang's lab; coming to work everyday was a joy due to the great atmosphere in

our lab. We are blessed to share an environment of support, camaraderie, and friendship. We function like a family, seeking each other's benefit for the overall wellbeing of the lab. Thank you guys.

I want to also express my gratitude to William Seward and his staff at the Department of Chemistry machine shop. We are lucky to have William!!! Without him, my TD-ID-CIMS would be drawings on a computer, and this dissertation would not be a reality. I must also say thank you to William Merka at the glass shop for sharing his expertise, and always having an open door policy for us graduate students. Both the machine and glass shops at the Department of Chemistry are top-notch facilities that allow for ideas to become realities.

I must also say a big thank you to Sandra Manning and her staff at the graduate office in the Department of Chemistry. Throughout my entire time at Texas A&M, Sandy has been instrumental in completing all my documentation and requirements with the department and the office of graduate and professional studies. Thank you Sandy. I must also acknowledge Dr. Joanna Goodey-Pellois, Valery McLaughlin, Judy Ludwig, Angie Medina, Mary Morgan, Crystal King, Ron Carter, and Julie Zercher. Their service and attention to our needs make research possible.

Part of our development as graduate students in science is the teaching experience. To thus, I must thank Dr. Amber Schaefer and Dr. Tom Leung who directed me during my time as a teaching and instruction assistant at the First Year Program in Chemistry. Teaching chemistry to three thousand undergraduates is not an easy task. I was honored to work for Dr. Schaefer and Dr. Leung. Thank you for your support and

letters of recommendation. I must also thank Dr. Elmo Mawk for his support through my time teaching the senior level instrumental analysis class. I really enjoyed working with senior chemistry majors.

I must also thank my parents, Dr. Hugo and Miriam Gomez, my first role models and heroes. Their support through the years has been paramount to my success. Without their support and sacrifices, this dissertation, my education, and my future career would not be anything more than just dreams. Thank you mom and dad! I must also say thank you to my brothers Hugo and Gabriel, and my sister Christa. I am finally done with school.

On July 5<sup>th</sup> 2014, my life changed forever, I married the love of my life, my best friend, confidant, and the most beautiful woman in the world. I love you Heydi Masiel. Your support through my final years of graduate school gave me the boost and motivation to get this done. Thank you for understanding the long hours and the odd work schedule required to finish my experiments, manuscripts, and this dissertation. I love you, and I am blessed to have you at my side. Like our favorite song from Bacilos says: “Dejemoslo todo y vamonos para Miami!!!”

As a Christian and a man of faith, I believe that everything I do follows a purpose and a plan written in heaven. I hold to the conviction that science is the best method to understand the beauty of the vision of the creator for our universe. We are barely starting to scratch the surface. Therefore, I must place this dissertation at the feet of my master and savior, Jesus Christ. May this work be to the glory of the one who traded heaven for me. Thank you Master, I await your return.

## NOMENCLATURE

AcA	Acetic Acid
AdA	Adipic Acid
AP-CIMS	Atmospheric Pressure-Chemical Ionization Mass Spectrometry
AzA	Azelaic Acid
c-PA	cis-Pinonic Acid
DMA	Dimethylamine
CE	Collection Efficiency
CCN	Cloud Condensation Nuclei Counter
CPC	Condensed Particle Counter
EPC	Electrostatic Particle Collector
$D_p$	Mobility Diameter
H-TDMA	Hygroscopicity Tandem Differential Mobility Analyzer
NPF	New Particle Formation
MA	Methylamine
MaA	Malic Acid
p-TA	para-Toluic acid
TD-ID-CIMS	Thermal Desorption Ion-Drift Chemical Ionization Mass Spectrometry
OxA	Oxalic Acid
PM	Particulate Matter



PrPA	Propanoic Acid
SOA	Secondary Organic Aerosol
SA	Succinic Acid
SCCM	Standard Cubic Centimeter Per Minute
SLPM	Standard Liter Per Minute
TMA	Trimethylamine
VOC	Volatile Organic Compound

## TABLE OF CONTENTS

	Page
ABSTRACT .....	ii
DEDICATION .....	iv
ACKNOWLEDGEMENTS .....	v
NOMENCLATURE.....	viii
TABLE OF CONTENTS .....	x
LIST OF FIGURES.....	xii
LIST OF TABLES .....	xv
CHAPTER I INTRODUCTION.....	1
CHAPTER II DEVELOPMENT, CALIBRATION, AND APPLICATION OF A NOVEL THERMAL DESORPTION ION DRIFT CHEMICAL IONIZATION MASS SPECTROMETRY (TD-ID-CIMS) INSTRUMENT .....	6
Introduction.....	6
Experimental .....	11
Results and Discussion.....	17
Summary.....	35
CHAPTER III HETEROGENEOUS CHEMISTRY OF GLYOXAL ON ACIDIC SOLUTIONS. AN OLIGOMERIZATION PATHWAY FOR SECONDARY ORGANIC AEROSOL FORMATION .....	37
Introduction.....	37
Experimental .....	40
Results and Discussion.....	43
Summary.....	51

	Page
CHAPTER IV HYGROSCOPICITY, DELIQUESCENT, AND CLOUD CONDENSATION NUCLEI ACTIVITY OF ALKYLAMINIUM CARBOXYLATE AEROSOLS .....	53
Introduction.....	53
Experimental .....	57
Results and Discussion.....	63
Summary.....	75
CHAPTER V CONVERSION OF SULFUR DIOXIDE TO SULFATE UNDER NITROGEN DIOXIDE AND AMMONIA CONDITIONS .....	79
Introduction.....	79
Experimental .....	83
Results and Discussion.....	88
Summary.....	95
CHAPTER VI CONCLUSIONS.....	98
REFERENCES.....	104
APPENDIX VITA.....	126

## LIST OF FIGURES

FIGURE		Page
1	Schematic representation of the TD-ID-CIMS instrument .....	12
2	Desorption peaks of deposited samples by a micro-syringe on the platinum filament for different sulfuric acid masses using the $\text{CO}_3^-/\text{CO}_4^-$ reagent ion .....	18
3	Calibration of syringe-deposited samples on the platinum filament.....	19
4	Collection efficiency for ammonium sulfate particles as a function of the voltage applied on the platinum wire .....	23
5	Comparison of the integrated desorption peak areas between collected particles and syringe-deposited droplets of similar masses .....	25
6	Comparison of the integrated desorption peak areas between collected 10 nm particles and syringe-deposited droplets .....	26
7	TD-ID-CIMS of 2 nm aerosol particles in the positive (+) ion mode.....	28
8	TD-ID-CIMS analysis of adipic acid:DMA salt solution in the positive ion mode.....	30
9	TD-ID-CIMS analysis of azelaic acid:DMA salt solution in the positive ion mode.....	31
10	TD-ID-CIMS analysis of 20 nm sulfuric acid particles after exposure to isoprene oxide .....	32
11	Mechanism for the formation of polymers in sulfuric acid particles after exposure to isoprene oxide.....	34
12	Schematic illustration of the low-pressure fast flow reactor coupled to an ID-CIMS instrument.....	40

FIGURE	Page
13 (a) Temporal profile ( $I$ , relative intensity) of glyoxal when exposed to a 15 cm long vessel containing 75 wt % sulfuric acid at 253 K. Each drop in the signal corresponds to a 5 cm distance increment from 0 to 15 cm. The experiment is terminated by retracting the injector to its original position after approximately 150 seconds. (b) The signal intensity of glyoxal as a function of injector distance for the experiment shown in panel (a) .....	43
14 (a) Temporal profile ( $I$ , relative intensity) of glyoxal when exposed to a 15 cm long vessel containing 75 wt % sulfuric acid at 273 K. Each drop in the signal corresponds to a 5 cm distance increment from 0 to 15 cm. The experiment is terminated by retracting the injector to its original position after approximately 250 seconds. (b) The signal intensity of glyoxal as a function of injector distance for the experiment shown in panel (a) .....	45
15 Concentration dependence of the uptake coefficient ( $\gamma$ ) of glyoxal on sulfuric acid for 60, 75, and 93 wt % $\text{H}_2\text{SO}_4$ solutions at various temperatures .....	46
16 (a) and (b): Temporal profiles ( $I$ , relative intensity) of glyoxal when exposed to a 15 cm length of a vessel containing 60 and 75 wt % sulfuric acid at 273 K, respectively. (c) to (d): Plots of $1/\gamma$ vs $t^{1/2}$ for the temporal profiles in (a) and (b), respectively, for the exposure of the glyoxal to the acid reservoir. The lines are the linear least-square fit for each experiment .....	48
17 Depiction of the oligomerization of glyoxal and formation of SOA .....	50
18 Molecular structures of organic acids and alkylamine bases relevant to the alkylammonium carboxylate salts in this study .....	58
19 Hygroscopic growth factor (HGF) for alkylammonium carboxylate salts ....	64
20 Activation diameters ( $Dp_{50}$ ) of alkylammonium carboxylates .....	69
21 Comparison of the $\kappa$ values for derived from HGF and CCN results and the mixing rule .....	70
22 Measured HGF values at 90% RH as a function of acidity .....	73

FIGURE	Page
23 Mixing rule calculated $\kappa$ values .....	74
24 Schematic representation of the 1 m <sup>3</sup> Teflon lined Plexiglass chamber connected to TDMA, CPC, and TD-ID-CIMS .....	83
25 TD-ID-CIMS spectrum of ammonium sulfate standard solution.....	88
26 TD-ID-CIMS ionogram of sulfate in collected nanoparticles. Collection time = 40 minutes. Selected Ion Monitoring (SIM) for the sulfate ion at $m/z$ 96.....	89
27 TD-ID-CIMS of oxalic acid nanoparticles after exposure to sulfur dioxide, nitrogen dioxide, and ammonia at 65 % RH .....	90
28 Comparison of growth factor for 45 nm oxalic acid nanoparticles after exposure to gases at 65% RH.....	92
29 TD-ID-CIMS analysis of the aqueous condensation inside the Teflon Chamber .....	94

## LIST OF TABLES

TABLE	Page
1	Molecular structure, formula, molecular weight (MW), ion, sensitivity, detection limit, and correlation coefficient for all analytes measured by TD-ID-CIMS. Reagent ion used is (a) $\text{CO}_3^-/\text{CO}_4^-$ , (b) $\text{NO}_3^-$ , and (c) $\text{H}_3\text{O}^+$ ..... 21
2	Structure assignment for detected ions by TD-ID-CIMS in 20 nm sulfuric acid particles after exposure to isoprene oxide vapor ..... 33
3	Uptake coefficient ( $\gamma$ ) for the heterogeneous reaction of glyoxal on sulfuric acid for 60-93 wt% $\text{H}_2\text{SO}_4$ solutions at 253 to 273 K..... 47
4	Values of the $H^*$ for glyoxal on sulfuric acid for 60-93 wt% $\text{H}_2\text{SO}_4$ solutions at 263 and 273 K..... 49
5	Solubility and density of the weak organic acids utilized for HGF and CCN measurements ..... 59
6	Molecular weight (MW), HGF at 90% RH, and $\kappa$ values derived using three methods i.e., the mixing rule (MR) approximation, HGF results, and CCN results for aminium carboxylates. The $\kappa$ value from the HGF results is derived at 90% RH, and the $\kappa$ value from the CCN results is averaged at supersaturation ranging from 0.19 to 0.51%..... 67

# CHAPTER I

## INTRODUCTION

Atmospheric aerosols constitute one of the major frontiers in science today due to their abundance in the atmosphere, impact on human health, and direct and indirect influence on the planetary radiation balance.<sup>1</sup> However, the current understanding on their formation mechanism is limited, producing one of the largest uncertainties in climate predictions and atmospheric modeling.<sup>1</sup> By definition, atmospheric aerosols are solid/liquid microscopic particles suspended in the atmosphere with sizes spanning four orders of magnitude, from a few nanometers to 100  $\mu\text{m}$ .<sup>1,2</sup> In addition, aerosol particle concentrations can be as high as  $10^7$ - $10^8$   $\text{cm}^{-3}$  for urban and remote areas.<sup>2</sup>

Historically, the impact of atmospheric aerosols has been observed since ancient roman times as Seneca (ca. 60 AD) attributed atmospheric turbidity to volcanic gases and ash stating that “gloomy cold and stains darken the atmosphere of our region”.<sup>3</sup> More recently, in the 1700’s, Benjamin Franklin wrote that the “year without a summer” may have been attributed to a volcanic eruption in Iceland in the year 1783.<sup>3</sup> In the year 1883, red sunsets were reported around the globe, prompting the British Royal Society to call for a scientific competition to explain the global phenomena. Johann Kiessling, won the competition by providing data linking the red sunsets to stratospheric aerosol from the Krakatoa volcanic eruption of 1883, thus also discovering global circulation in the atmosphere.<sup>3,4</sup> These are only a few examples of the historical impact and recorded observations of the effect of aerosols on human society and the planet.



Atmospheric aerosols are divided into two major categories: primary and secondary particles.<sup>5,6</sup> Primary aerosols are emitted into the atmosphere from either natural (biogenic) or artificial (anthropogenic) sources. Natural sources may include sea salt aerosols from ocean and sea sprays, plants and animal activity, mineral dust from volcanic eruptions, and sandstorms from deserts around the world.<sup>2</sup> Artificial sources may include vehicular emissions, industrial plant activities, and urban construction. Secondary aerosols are produced by the nucleation of gas-phase species such as sulfuric acid, ammonia, water, and volatile organic compounds (VOCs).<sup>7-10</sup> Such phenomena has been observed in urban, remote, marine, and forested sites,<sup>11</sup> except at the amazon region, a tropical rain forest with high isoprene emissions.<sup>12,13</sup>

Currently, new particle formation (NPF) is understood as a two-step process. First, gas-phase species must nucleate to form a “critical nucleus” with diameters as low as 1.4 nm and containing as few as two molecules.<sup>1,14</sup> Second, the nucleus must grow to detectable sizes (>2-3 nm) while competing with removal of the newly nucleated particles by coagulation with pre-existing aerosols.<sup>1,14</sup> Considering that the nucleation process represents a transition from the gas-phase to the particle-phase, the nucleation process involves a decrease in entropy ( $\Delta S < 0$ ) and enthalpy ( $\Delta H < 0$ ) for the nucleating system. Although the first law of thermodynamics favors a decrease in enthalpy, the second law of thermodynamics does not favor the spontaneous decrease of entropy (disorder) in a system. Therefore, a free energy barrier  $\Delta G$  ( $\Delta G = \Delta H - T\Delta S > 0$ ) is involved and must be crossed before the transition to the particle-phase and

subsequent growth become spontaneous. Such energy barrier represents a major limitation to new particle formation and growth.

Another significant limitation to nucleation and growth of aerosols is the Kelvin (curvature) effect, which says that “*the vapor pressure over a curved surface interface always exceeds that of the same substance over a flat surface*”.<sup>2</sup> Thus, the Kelvin effect provides an elegant thermodynamic explanation for the elevated saturation vapor pressure over small particles: that as the particle diameter decreases, equilibrium vapor pressure increases. The Kelvin effect is expressed by the following equation:

$$pa = p_A^o \exp\left(\frac{2\sigma M}{RT\rho_l r}\right) \quad (1.1)$$

where  $p_A^o$  is the vapor pressure of A over a flat surface,  $\sigma$  is the surface tension,  $M$  is the molecular weight of A,  $R$  is the gas constant,  $T$  is the temperature of the system,  $\rho_l$  is the liquid-phase density of A, and  $r$  is the radius of the particle. However, the condensation of gas-phase molecules on a particle surface takes place when the ambient partial pressure of the gas-phase species is higher than the saturation vapor pressure over the particle. Considering that the saturation vapor pressure of the molecules surrounding the nanoparticle is dependent on temperature and both, the particle diameter and chemical composition; complete information of the chemical composition of the critical nuclei is of paramount importance in atmospheric chemistry.

Atmospheric aerosols directly affect human health. For example, 100 nm particles penetrate respiratory airways deeply into the lungs.<sup>15</sup> In addition, some recent

studies have discussed the link between mortality rate and human longevity to reductions in ambient aerosol loadings.<sup>16</sup> Atmospheric aerosols directly affect climate by absorption and scattering of solar radiation.<sup>2</sup> In addition, aerosols indirectly affect the Earth energy budget by acting as cloud condensation nuclei promoting cloud formation and altering cloud properties.<sup>17</sup> Therefore, changes in the chemical composition of aerosols also alter the effects of aerosols on climate and human health. Thus, a better understanding on the chemical composition of aerosols is of paramount importance.

The present dissertation describes laboratory studies regarding the chemical composition, formation, growth, and physicochemical properties of secondary organic aerosol (SOA), a significant segment of atmospheric aerosols. Chapter II describes the development, calibration, and application of a novel thermal desorption ion-drift chemical ionization mass spectrometry (TD-ID-CIMS) instrument for nucleation to accumulation mode aerosols. Our TD-ID-CIMS is an analytical technique that provides chemical information on the composition of aerosol particles with diameters as small as 2 nm, and with sample loads as low as 0.1 ng. Therefore, at such small particle sizes, TD-ID-CIMS allows for the elucidation of the chemical composition of aerosol particles near the critical nuclei diameter generated by the oxidation of VOCs in chamber studies. In our laboratory, TD-ID-CIMS has also been utilized to identify the products of the reactions of epoxides and sulfuric acid nanoparticles, and the chemical composition of alkylaluminium carboxylates after evaporation.

Chapter III discusses the heterogeneous chemistry of glyoxal on sulfuric acid surfaces by measuring the temperature and concentration dependence of the uptake

coefficient ( $\gamma$ ) and Henry's Law constant ( $H^*$ ) utilizing a low-pressure fast flow laminar reactor coupled to an ion drift-chemical ionization mass spectrometer. Our measurements offer insight into a hydration driven dicarbonyl oligomerization pathway for the formation of secondary organic aerosols (SOA).

Chapter IV discusses the hygroscopicity and cloud condensation nuclei activity (CCN) of alkylammonium carboxylate aerosols. Experiments were conducted on a tandem differential mobility analyzer (TDMA) and a cloud condensation nuclei counter coupled to a condensation particle counter (CPC). Atmospheric alkylammonium carboxylates are the products of gas-phase reactions between weak organic acids and alkylamine bases, and thus constitute a significant segment of organic nitrogen containing species in the atmosphere. These newly formed salts may in turn condense into the particle phase to form SOA with varied hygroscopic and CCN characteristics dependent on their chemical composition. In addition, we have derived the hygroscopicity parameter ( $\kappa$ , kappa) for all our studied ammonium carboxylate salts under three methods: hygroscopic growth factor, cloud condensation nuclei, and the mixing rule approximation.

Chapter V discusses experiments regarding the conversion of sulfur dioxide ( $\text{SO}_2$ ) into sulfate ( $\text{SO}_4^{2-}$ ) in the presence of nitrogen dioxide ( $\text{NO}_2$ ) and ammonia ( $\text{NH}_3$ ). Such experiments may offer an insight into the accelerated formation of atmospheric sulfate during episodes of intense haze formation in highly polluted places such as Beijing, China. Chapter VI summarizes the results from chapter II-V, offering concluding remarks and potential future research directions.

CHAPTER II  
DEVELOPMENT, CALIBRATION, AND APPLICATION OF A NOVEL  
THERMAL DESORPTION ION DRIFT CHEMICAL IONIZATION  
MASS SPECTROMETRY (TD-ID-CIMS) INSTRUMENT\*

**Introduction**

Atmospheric aerosols originated from natural and anthropogenic sources exhibit a broad range of impacts on the atmosphere. In particular, fine aerosols (i.e., particulate matter or PM with the aerodynamic diameter smaller than 2.5  $\mu\text{m}$ ) profoundly impact human health, visibility, ecosystem, weather, and climate.<sup>18-21</sup> For example, the adverse effects of PM on human health have been clearly demonstrated, ranging from aggravating allergies to the development of serious chronic diseases and premature death.<sup>22</sup> Also, aerosols modify the lifetime and albedo of clouds, precipitation, and lightning, modulate photochemistry, promote multiphase chemistry, degrade local, regional, and global air quality, and impact the Earth energy budget directly by interfering with the solar radiative transfer and indirectly by influencing cloud formation.<sup>18-21,23,24</sup> Currently, the direct and indirect radiative forcings by aerosols represent the largest uncertainty in climate projections.<sup>18</sup>

---

\* Part of this chapter is reprinted with permission from Lavi, A.; Segre, E.; Gomez-Hernandez, M.; Zhang, R.; Rudich, Y. Volatility of Atmospherically Relevant Alkylammonium Carboxylate Salts. *The Journal of Physical Chemistry A*, **2015**, 119 (19), pp 4336–4346. Copyright 2014 American Chemical Society. Part of this chapter is reprinted with permission from Xu, W.; Gomez-Hernandez, M.; Guo, S.; Secret, J.; Marrero-Ortiz, W.; Zhang, A. L.; Zhang, R. Acid-catalyzed reactions of epoxides for atmospheric nanoparticle growth. *Journal of the American Chemical Society*. **2014**, 136, 44,15477-15480. Copyright 2014 American Chemical Society.

The atmospheric effects of aerosols are largely dependent on the particle properties, including the number concentration, size, and chemical composition, which are related to their formation pathways.<sup>14</sup> Aerosols are emitted directly into the atmosphere (primary) or formed in the atmosphere through gas-to-particle conversion (secondary). Secondary aerosol formation includes nucleation to form nano-sized (nucleation mode) particles and their subsequent growth to sub- $\mu\text{m}$  (accumulation mode) particles, and their compositions consist of a complex mixture of various chemical constituents, including a large mass fraction of inorganics and organics.<sup>14, 7, 1</sup> Because of the complexities in the formation and chemical compositions, measurements of aerosols under diverse environmental conditions represent a major challenge to quantify their abundance and decipher their chemical identity, which requires a synergy of different highly advanced analytical approaches.<sup>14, 25</sup>

Recently, mass spectrometry has emerged as a promising tool to address the analytical challenges imposed by atmospheric aerosol measurements.<sup>26-30</sup> Mass spectrometry offers a fast responding, robust, versatile, sensitive, and accurate analytical platform for measuring the chemical compositions of aerosols. Currently, aerosol analysis by mass spectrometry is divided into two categories, i.e., off-line and on-line measurements.<sup>26, 27</sup> While both modes offer several advantages, the drawbacks of both approaches hinder efforts to obtain a comprehensive understanding of the formation, growth, and impacts of aerosols in the atmosphere. For example, off-line methods typically suffer from a long collection time that hinders real-time measurements, affecting the temporal resolution of the analysis. On-line aerosol mass spectrometry

(AMS) is capable of measuring the size-resolved particle chemical composition with a high time resolution (seconds to minutes), high sensitivity, and low detection limit.<sup>30-34</sup> There exist two common types of online AMS, i.e., laser desorption/ionization mass spectrometry (LDI-MS) and thermal desorption electron impact ionization mass spectrometry (TD-EI-MS).<sup>35</sup> The major difference between the two types of AMS lies in particle vaporization and ionization: LDI-MS is used for analysis of individual aerosol particles by identification of the chemical particle classes associated with subsets of the particles, while TD-EI-MS is usually used for quantitative determination of non-refractory aerosol components.

A commercial AMS developed by the Aerodyne Res. Inc. has been widely applied for ambient aerosol measurements.<sup>36-38</sup> For the Aerodyne AMS, aerosols are focused into a narrow beam by an aerodynamic lens and transmitted into a detection chamber, where they are impacted on a heated surface. Vaporized aerosol species are ionized by electron impact and analyzed via mass spectrometry. The particle time-of-flight from a mechanical beam chopper to the vaporizer is measured to obtain chemically speciated size distributions. The Aerodyne high-resolution time-of-flight aerosol mass spectrometry (HR-ToF-AMS) achieves the MS resolution ranging from 2500 (in V-mode) or 4500 to 5000 (in W-mode), where the V and W represent the path of the ions in the flight chamber. The high mass resolution allows the separation of each unit mass peak into separate contributions for specific elemental compositions based on small differences in mass defects.

On the other hand, the currently available on-line AMS methods still suffer from significant fragmentation of the analytes, because of the evaporation and ionization techniques utilized (i.e., LDI-MS or TD-EI). In addition, measurements of nucleation mode particles by on-line AMS are difficult, because of their significantly smaller masses for efficient detection and quantification. A nano-aerosol mass spectrometer (NAMS) has been developed by Johnston and co-authors for real-time characterization of sub-10-nm aerosols.<sup>39</sup> The NAMS approach includes an aerodynamic inlet, quadrupole ion guide, quadrupole ion trap, and time-of-flight (TOF) mass analyzer; charged particles are introduced into the aerodynamic inlet, transmitted by the ion guide, and captured in the ion trap, and analyzed by the TOF-MS. In addition, semi-online approaches, which collect particles for a sufficient amount and use soft evaporation/ionization techniques, have the advantages of analyzing nanoparticles and minimizing analyte fragmentation. For example, thermal desorption - chemical ionization mass spectrometry (TD-CIMS) has been developed for the analysis of the chemical composition of down to sub-20 nm ultrafine aerosols.<sup>40-42</sup> The TD-CIMS developed by Smith and co-workers combines an electrostatic precipitator for particle separation and collection with CIMS detection, with a high sensitivity for down to 10 nm particles. In addition, Held et al. have reported the application of Thermal Desorption Ion Trap Mass Spectrometry for the analysis of ultrafine aerosol particles.<sup>43</sup>

Because of its soft ionization, selectivity, and high sensitivity, CIMS has been widely employed in atmospheric chemistry research, including laboratory kinetic investigations and field trace gas measurements.<sup>44-46</sup> In the CIMS method, a neutral



species is ionized by a reagent ion to yield the product ion, which is then analyzed by a mass spectrometer for identification and quantification. An ion drift chemical ionization mass spectrometry (ID-CIMS) technique has been developed to detect and quantify various organic and inorganic trace species.<sup>47, 48</sup> The key components of the ID-CIMS system include an ionization source to produce the reagent ions, a drift tube for the ion–molecule reaction and guiding the reagent and product ions, and a mass spectrometer for analysis of the reagent and product ions. Among several advantages, the ID-CIMS method allows for quantification of analytes without the necessity of calibration using authentic samples.

Currently, the development of more advanced aerosol analytical techniques is still required to achieve the highest level of chemical speciation and to identify and quantify the diverse organic and inorganic constituents from molecular clusters, nucleation, to accumulation mode particles. In this paper we describe the design and calibration of thermal desorption - ion drift - chemical ionization mass spectrometry (TD-ID-CIMS), which includes an integrated differential mobility analyzer and condensation particle counter system for charging and size separation, an electrostatic particle collector (EPC) for collection and thermal desorption of particles, and ID-CIMS for generation of reagent ions, ion-molecular reactions between reagent and product ions, and detection of product ions. The performance of this instrument is evaluated to establish the collection efficiency, sensitivity, and detection limit for a broad range of particle sizes and chemical compositions using various reagent ions. Additional

qualitative applications of this instrument for detection of nano-sized organic and inorganic aerosols can be found in our previous publications.<sup>9, 10, 49-51</sup>

## **Experimental**

Fig. 1 depicts the schematic of the TD-ID-CIMS instrument. The TD-ID-CIMS consisted of several components, including a combined atomizer, differential mobility analyzer (DMA), and condensation particle counter (CPC) system for particle production, size-separation, and charging, an electrostatic particle collector (EPC) for collection and thermal desorption (TD) of particles, and ID-CIMS for generation of reagent ions, ion-molecular reaction, and detection of product ions.

Briefly, aerosols generated by the atomizer were first size-selected and charged by the DMA, and subsequently introduced into the collection chamber. The charged particles were deposited on the EPC, which was oppositely charged with a DC voltage. Once sufficient deposited particle mass was collected on the EPC, the EPC was pushed to the front region of the drift tube, and an AC voltage was applied to the EPC to heat the filament to a temperature of about 350°C and to evaporate the collected mass. Within the drift tube, reagent ions were generated and the ion-molecular reactions between the neutral analytes and reagent ions occurred to form the product ions. The product ions were then detected and analyzed by a triple quadrupole MS (QqQ).

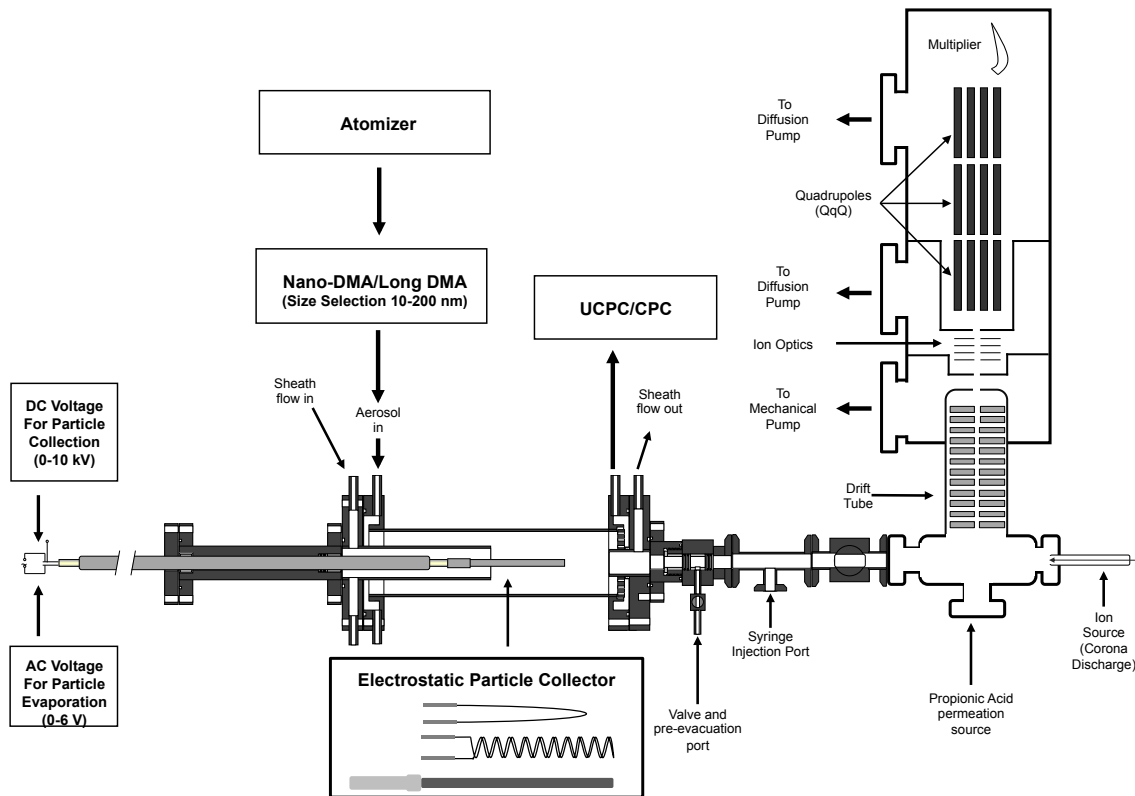


**Figure 1. Schematic representation of the TD-ID-CIMS instrument. The insert at the bottom depicts three different designs of the electrostatic particle collector (EPC), i.e., a platinum wire (top), a nichrome coil (middle), and a stainless steel rod (bottom). Samples were collected in the collection chamber or directly deposited using a micro-syringe on the EPC. The EPC was then slid into the front region of the drift tube, and the collected or injected samples were vaporized by resistive heating. Reagent ions produced by the corona discharge reacted with the analytes throughout the drift tube, which consisted of 24 stainless steel conductive rings. Product ions were transferred to the mass spectrometer (MS) through a pinhole and ion optics before being analyzed by a triple quadrupole (QqQ) MS.**

A commercial continuous-flow atomizer (TSI 3076) was employed to produce aerosols in the size range of 10 to 200 nm. Particles were size-selected and detected using a nano DMA (nDMA 308500, TSI, Incorporated) coupled to an ultrafine CPC (UCPC 3025A, TSI, Incorporated) for nucleation mode particles (10 to 20 nm) and a long DMA (DMA 3081, TSI, Incorporated) and a CPC (CPC 3760A, TSI, Incorporated) for accumulation mode particles (20 to 200 nm). The DMA-CPC systems were controlled by LabVIEW software through National Instruments data acquisition interface cards.

Within the collection chamber, the EPC was concentrically located within a stainless steel cylindrical housing (1" outer diameter). Aerosols were introduced to the collection chamber with a N<sub>2</sub> flow of 1 slpm, and a sheath flow of about 0.5 slpm was introduced into the stainless steel EPC housing to maintain a laminar flow condition in the collection chamber. The cylindrical housing and the sheath flow protected the EPC from possible contamination by gaseous species in the aerosol flow. Size-selected and charged particles were introduced to the stainless steel collection chamber and deposited on the EPC. Three designs were considered for the filament of the EPC, including a platinum wire (0.01" diameter and 1.7" length), a nichrome coil (0.02" diameter and 2.4" length), and cylindrical stainless steel rod (0.20" diameter and 3.9" length). To achieve sensitive and reproducible results, a rapid rate of heating to a high temperature (about 350°C) was desirable for efficient thermal desorption of the collected mass. Also, an efficient cooling for the EPC was necessary to allow for experiments conducted in a timely fashion. As to be discussed below in the results section, the platinum wire worked

efficiently for nucleation mode particles, while the nichrome coil was preferred for accumulation mode particles. Although the cylindrical stainless steel rod also exhibited high collection efficiency because of a large collecting surface area, its large thermal inertia proved to be inefficient for heating of the collected mass and cooling of the EPC. The heating and cooling times for the platinum wire and the nichrome coil were about 5 and 10 seconds during typical experiments. The AC voltage applied to the EPC for evaporation was about 2.1 and 4.5 V for the platinum wire and the nichrome coil, respectively. For aerosol collection, a high DC voltage (1-10 kV) was applied to the EPC, and the collection time for a desirable sample mass (0.1-10 ng) was dependent of the particle size. For example, the collection time was about a few minutes for accumulation mode particles, but up to a few hours for nucleation mode particles. The exposure length of the EPC to the aerosol flow (i.e., extension over the housing) was adjusted to achieve the maximal collection efficiency, which was also depended of the particle size, voltage, and geometry of the filament.

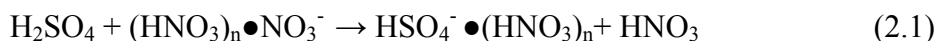
The particle collection efficiency of the EPC was determined by the UCPC/CPC, which was located at the end of the collection chamber, on the basis of the difference in particle counts with and without the DC voltage applied to the EPC. The mass of collected particles on the EPC was estimated by considering the measured particle collection efficiency, the particle size and density, and the flow velocity in the collection chamber. Alternatively, samples of known chemical compositions and masses were directly deposited on the EPC through the syringe injection port for the calibration purpose.

The drift tube typically operated at a pressure of about 0.5 Torr. Positive or negative reagent ions were produced by a corona discharge device. The voltages of about -740 V and 1300 V were applied to the corona needle for the negative and positive modes, respectively, while the discharge electrode was grounded. In the drift tube, the neutral analyte was chemically ionized by the ion-molecule reactions with the reagent ions, yielding the product ions with low fragmentation. The drift tube was composed of 24 stainless steel rings connected in series and with 1-M $\Omega$  resistors between the rings, and each stainless steel rings had an internal diameter of 1.4 cm. The first ring of the drift tube was charged to -116 V in the negative mode and 60 V in the positive mode, while the last ring was grounded, to achieve maximal ion transmission efficiency. By maintaining an appropriate electrical field in the drift tube, undesirable cluster ions are effectively suppressed.<sup>52</sup> Also, the ID-CIMS method allows for the quantification of the gas-phase concentrations without the necessity of calibration, since the ion-molecule reaction time is precisely controlled within the drift tube and ion-molecule reaction rate constants can be accurately determined experimentally or theoretically.<sup>53</sup>

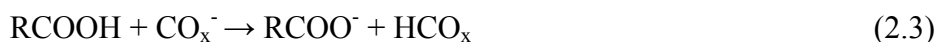
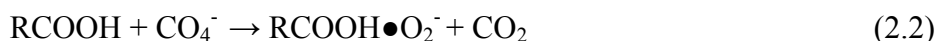
Reagent and product ions entered the mass spectrometer through a pinhole with an aperture of 0.2 mm, which was biased at -6 V in the negative mode and 60 V in the positive mode. All mass spectrometry experiments were performed using an Extrel ELQ 400 (Extrel CMS, Pittsburgh, PA) mass spectrometer equipped with a triple quadrupole (QqQ). The QqQ allows for the MS/MS application with potentially added identification of the analyte, i.e., using the first quadrupole (Q1) for mass selection, the second quadrupole (Q2) for collision dissociation or addition, and the third quadrupole (Q3) for

MS analysis. For the TD-ID-CIMS experiments in the present work, the Q3 was employed as the mass filter, while Q1 and Q2 were tuned for optimal ion transmission.

Three different types of ion-molecule reactions were employed for analysis of various organic and inorganic species. Sulfuric acid was detected using the  $\text{NO}_3^-$  reagent ion, according to the following ion-molecular reaction,



In the present work, sulfuric acid was detected as  $\text{HSO}_4^-$  (97 amu), i.e., with  $n = 0$ . Alternatively, the  $\text{CO}_3^-/\text{CO}_4^-$  ion was used to ionize sulfuric acid, also yielding the  $\text{HSO}_4^-$  product ion. Organic acids (p-toluic, oleic, stearic, and succinic acids) were ionized by the  $\text{CO}_3^-/\text{CO}_4^-$  reagent ion, according to the following ion-molecule reaction schemes,



where  $x = 3$  or  $4$ . In addition, the hydronium ion ( $\text{H}_3\text{O}^+$ ) was employed to ionize dimethylaminium acetate and dimethylaminium sulfate, both leading to the protonated dimethylamine fragment,  $(\text{CH}_3)_2\text{NH}_2^+$  (46 amu).

Calibration of the TD-ID-CIMS was performed by directly depositing a droplet of a known mass and chemical composition onto the tip of the EPC using a glass micro-syringe. Liquid solutions were prepared by the standard dissolution procedure to produce a concentration of 1000 ng/ $\mu\text{L}$ . A Mettler-Toledo analytical balance was utilized to measure the mass of the pure analytes before dilution in the solvent (water). Solutions were then prepared using clean and oven-dried volumetric glassware, and the concentrations were 10, 7, 5, 3, 1, 0.7, 0.5, 0.3, and 0.1 ng/ $\mu\text{L}$ . The micro-syringe was

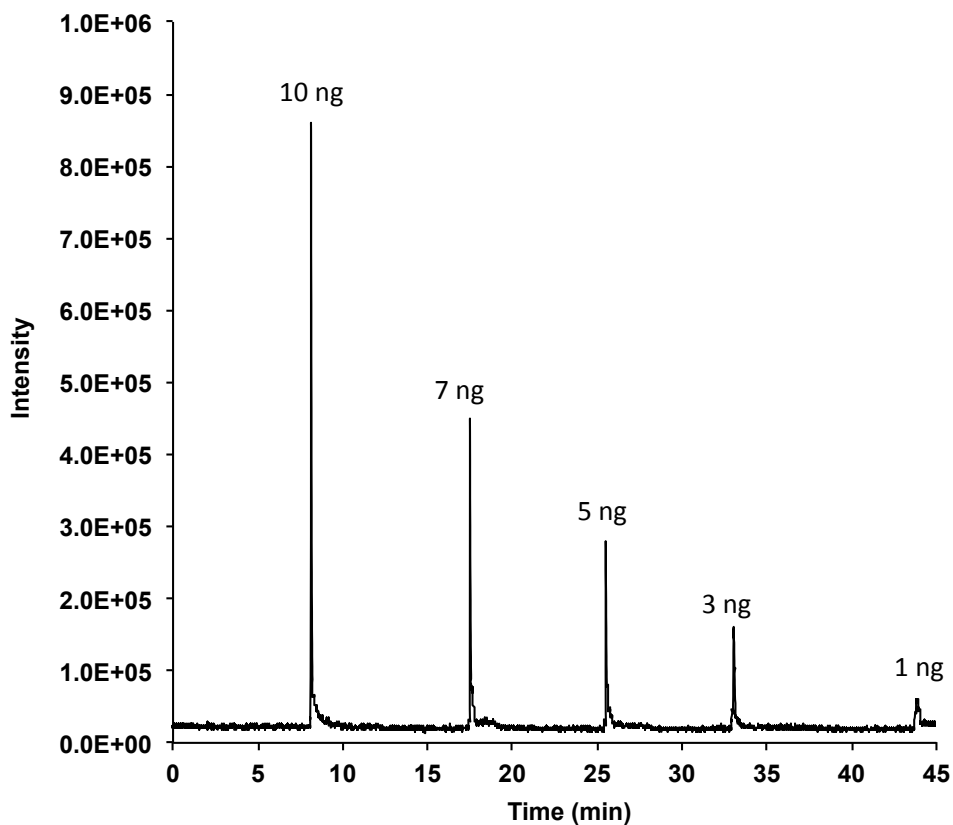
utilized to deposit 1  $\mu\text{L}$  droplet of the sample solution onto the EPC. A stream of  $\text{N}_2$  gas (12 slpm) was utilized to dry the deposited droplet, and the sample was then introduced to the drift tube region and subjected to resistive heating to vaporize the analyte, which was subsequently ionized and analyzed by the ID-CIMS.

In addition, to account for possible variations in the MS signal intensity between replicate experiments (i.e., drifts in the background signal, reagent ion, corona discharge efficiency, etc.), a constant propionic acid ( $\text{C}_3\text{H}_6\text{O}_2$ ) flow from a propionic acid permeation source (294 nmoles/s at  $32^\circ\text{C}$ ) was introduced to the ID-CIMS prior to each measurement. Propionic acid was ionized using the  $\text{H}_3\text{O}^+$  or  $\text{CO}_3^-/\text{CO}_4^-$  reagent ion, yielding the product ion of  $\text{C}_3\text{H}_6\text{O}_2\cdot\text{H}^+$  (75 amu) or  $\text{C}_3\text{H}_6\text{O}_2\cdot\text{O}_2^-$  (106 amu), respectively. The observed propionic acid signal was employed to correct the variation in the MS signal intensity between different measurements, which was typically less than 10%.

## Results and Discussion

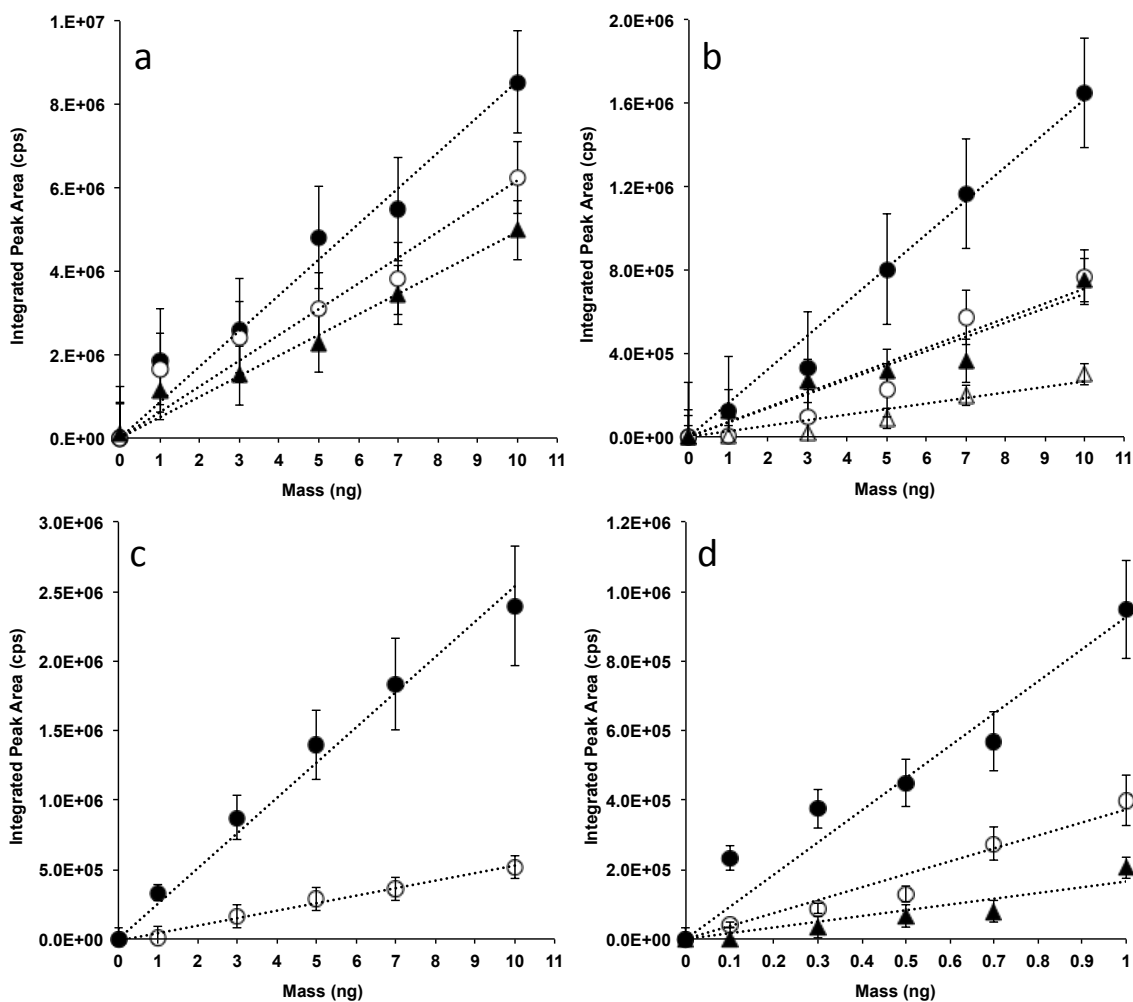
Fig. 2 illustrates a typical ionogram for syringe-deposited sulfuric acid samples in the mass range from 1 to 10 ng measured using the  $\text{CO}_3^-/\text{CO}_4^-$  reagent ion. The experiments were performed by depositing a droplet of 1  $\mu\text{L}$  volume of sulfuric acid solutions on the platinum wire, and the dried mass was determined from the sample volume and sulfuric acid concentration. Each peak in the ionogram corresponds to thermal desorption of a sample, and the peak area is integrated to quantify the total amount of the desorbed mass. It is evident from Fig. 2 that the intensity of the desorption peaks well correlate with the deposited sample masses.





**Figure 2. Desorption peaks of deposited samples by a micro-syringe on the platinum filament for different sulfuric acid masses using the  $\text{CO}_3^-/\text{CO}_4^-$  reagent ion.**

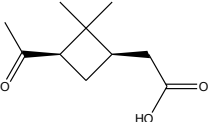
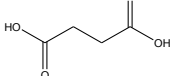
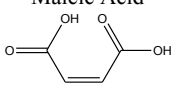
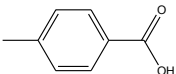
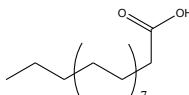
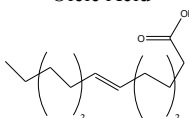
Fig. 3 shows calibration of syringe-deposited samples for various organic (organic acids, dimethylaminium sulfate, and dimethylaminium estate) and inorganic (sulfuric acid, ammonium sulfate, and ammonium bisulfate) species on the platinum filament using the three reagent ions.



**Figure 3. Calibration of syringe-deposited samples on the platinum filament. (a) sulfuric acid (solid circles), ammonium sulfate (open circles), ammonium bisulfate (solid triangles) masses using the  $\text{CO}_3^-/\text{CO}_4^-$  reagent ion, (b) p-toluic acid (solid circles), oleic acid (open circle), and stearic acid (solid triangles), and succinic acid (open triangles) masses using the  $\text{CO}_3^-/\text{CO}_4^-$  reagent ion, (c) dimethylaminium sulfate (solid circles) and dimethylaminium acetate (open circle) masses using the  $\text{H}_3\text{O}^+$  reagent ion, and (d) maleic acid (solid circles), cis-pinonic acid (open circles), and p-toluic acid (solid triangles) with sub-nanogram masses (< 1 ng) using the  $\text{CO}_3^-/\text{CO}_4^-$  reagent ion. Each point represents the average of three experiments, and the uncertainty reflects the random error of the measurements ( $1\sigma$ ).**

Most of the experiments were performed in the mass range of 1 to 10 ng (Figs. 3A-C), and additional measurements were conducted in the mass range of 0.1 to 1 ng for selected organic acids (Fig. 3D). Figure 3 shows a good linearity between the integrated peak area and the deposited mass for all species investigated and reagent ions used, with the correlation coefficient ( $R^2$ ) in the range of 0.95 to 0.99. The sensitivity and detection limit of the TD-ID-CIMS were estimated from the slope of the lines in Fig. 3 and three times of the signal to noise ratio (S/N) for the smallest mass deposited of each species, respectively. Table 1 summarizes the molecular structures, ion assignments, sensitivities, detection limits, and the correlation coefficients for all species calibrated by TD-ID-CIMS using the three reagent ions. The TD-ID-CIMS exhibits somewhat different performances for the various organic and inorganic species, dependent of the reagent ions. For example, using the  $\text{CO}_3^-/\text{CO}_4^-$  reagent ion, the TD-ID-CIMS is more sensitive to sulfuric acid than to ammonium sulfate and bisulfate, but with comparable detection limits among the three inorganic sulfate forms (Fig. 3A and Table 1). The use of the  $\text{NO}_3^-$  reagent ion yields both a higher sensitivity and lower detection limit for sulfuric acid than those using the  $\text{CO}_3^-/\text{CO}_4^-$  reagent ion. Among the organic acids (Figs. 3B and 3D and Table 1), malic acid exhibits the highest sensitivity, while cis-pinonic acid shows the lowest detection limit using the  $\text{CO}_3^-/\text{CO}_4^-$  reagent ion. Also, the linearity between the integrated peak area and sample mass is similar for selected organic acids with high (1 to 10 ng) and low (0.1 to 1 ng) masses, with comparable correlation coefficients. For p-toluic acid, for example, the same linearity extends from 0.1 to 10 ng.

**Table 1. Molecular structure, formula, molecular weight (MW), ion, sensitivity, detection limit, and correlation coefficient for all analytes measured by TD-ID-CIMS. Reagent ion used is (a)  $\text{CO}_3^-/\text{CO}_4^-$ , (b)  $\text{NO}_3^-$ , and (c)  $\text{H}_3\text{O}^+$ .**

Analyte	Formula (MW)	Ion (m/z)	Sensitivity ( $\times 10^4$ ) (cps/ng)	Detection Limit ( $\times 10^{-1}$ ) (ng)	$R^2$	
Sulfuric Acid	$\text{H}_2\text{SO}_4$ (98.1)	$\text{HSO}_4^-$ (97.1)	74.6 <sup>a</sup> 199.1 <sup>b</sup>	1.2 <sup>a</sup> 0.3 <sup>b</sup>	0.97 <sup>a</sup> 0.99 <sup>b</sup>	
Ammonium Sulfate	$(\text{NH}_4)_2\text{SO}_4$ (132.1)	$\text{HSO}_4^-$ (97.1)	49.1 <sup>a</sup>	1.3 <sup>a</sup>	0.95 <sup>a</sup>	
Ammonium Bisulfate	$(\text{NH}_4)\text{HSO}_4$ (115.1)	$\text{HSO}_4^-$ (97.1)	44.1 <sup>a</sup>	1.2 <sup>a</sup>	0.97 <sup>a</sup>	
<i>cis</i> -Pinonic acid		$\text{C}_{10}\text{H}_{16}\text{O}_3$ (184.2)	$\text{C}_{10}\text{H}_{16}\text{O}_3 \cdot \text{O}_2^-$ (216.2)	35.1 <sup>a</sup>	0.1 <sup>a</sup>	0.99 <sup>a</sup>
Succinic Acid		$\text{C}_4\text{H}_6\text{O}_4$ (118.1)	$\text{C}_4\text{H}_5\text{O}_4^-$ (117.1)	4.5 <sup>a</sup>	5.6 <sup>a</sup>	0.99 <sup>a</sup>
Maleic Acid		$\text{C}_4\text{H}_4\text{O}_4$ (116.1)	$\text{C}_4\text{H}_3\text{O}_4^-$ (115.1)	59.4 <sup>a</sup>	1.0 <sup>a</sup>	0.99 <sup>a</sup>
Toluic Acid		$\text{C}_8\text{H}_8\text{O}_2$ (136.1)	$\text{C}_8\text{H}_8\text{O}_2 \cdot \text{O}_2^-$ (168.1)	17.6 <sup>a</sup>	2.6 <sup>a</sup>	0.99 <sup>a</sup>
Stearic Acid		$\text{C}_{18}\text{H}_{36}\text{O}_2$ (284.5)	$\text{C}_{18}\text{H}_{36}\text{O}_2 \cdot \text{O}_2^-$ (316.5)	6.4 <sup>a</sup>	0.9 <sup>a</sup>	0.89 <sup>a</sup>
Oleic Acid		$\text{C}_{18}\text{H}_{34}\text{O}_2$ (282.5)	$\text{C}_{18}\text{H}_{34}\text{O}_2 \cdot \text{O}_2^-$ (314.5)	9.0 <sup>a</sup>	0.6 <sup>a</sup>	0.96 <sup>a</sup>
Dimethyl Aminium Acetate	$\text{NH}(\text{CH}_3)_2\text{CH}_3\text{COOH}$ (105.1)	$(\text{CH}_3)_2\text{NH}_2^+$ (46.1)	5.5 <sup>c</sup>	6.3 <sup>c</sup>	0.98 <sup>c</sup>	
Dimethyl Aminium Sulfate	$(\text{NH}(\text{CH}_3)_2)_2\text{H}_2\text{SO}_4$ (188.2)	$(\text{CH}_3)_2\text{NH}_2^+$ (46.1)	22.9 <sup>c</sup>	2.7 <sup>c</sup>	0.99 <sup>c</sup>	

In addition, dimethylaminium sulfate has a higher sensitivity and lower detection limit than those of dimethylaminium acetate using the  $\text{H}_3\text{O}^+$  reagent ion. The sensitivity for the various organic and inorganic species using the different reagent ions is dependent of the ion-molecule reaction rate constants, ion transmission efficiency of the drift tube and the MS optics, and the background signal, while the detection limit is more dependent of the background signal, which is related to the mass range and the use of the reagent ions.

In our experiments, the background signal is typically lower for the  $\text{NO}_3^-$  reagent ion than those for the  $\text{CO}_3^-/\text{CO}_4^-$  and  $\text{H}_3\text{O}^+$  reagent ions, explaining the highest sensitivity and a lower detection limit for sulfuric acid using the  $\text{NO}_3^-$  reagent ion. For comparison, our TD-ID-CIMS exhibits a sensitivity similar to, but a higher detection limit than those reported by Voisin et al.<sup>40</sup> In that previous work, a radioactive material ( $^{231}\text{Am}$ ) emitting  $\alpha$  particles was employed to ionize the buffer gas mixture to form nitrogen and oxygen ions and to yield  $\text{H}_3\text{O}^+$ ,  $\text{O}_2^-$ , and  $\text{CO}_3^-$  as the reagent ions, likely corresponding to lower background signals than those from the corona discharge ion source.<sup>47, 48</sup>

To evaluate the collection efficiency of the EPC for particles of different sizes, experiments were performed to identify the maximal exposure length and voltage for the platinum and nichrome filaments. For experiments using the platinum filament for nucleation mode particles (Fig. 4A), the collection efficiency increases with the increasing exposure length and voltage of the filament and decreasing particle size.

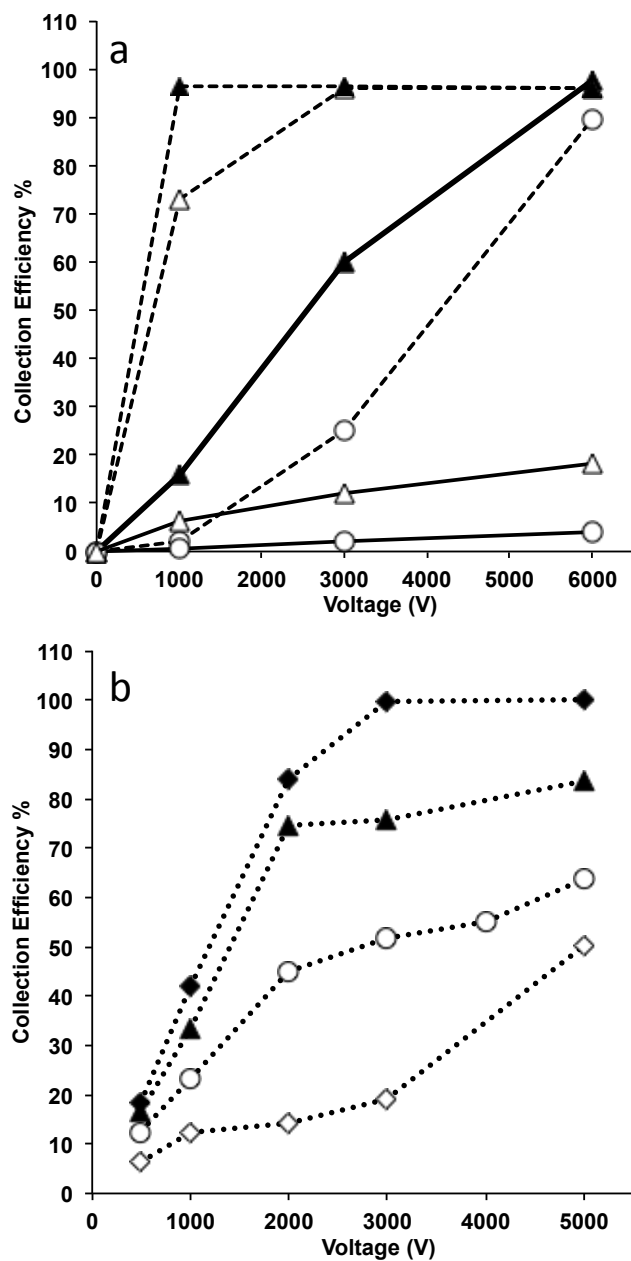
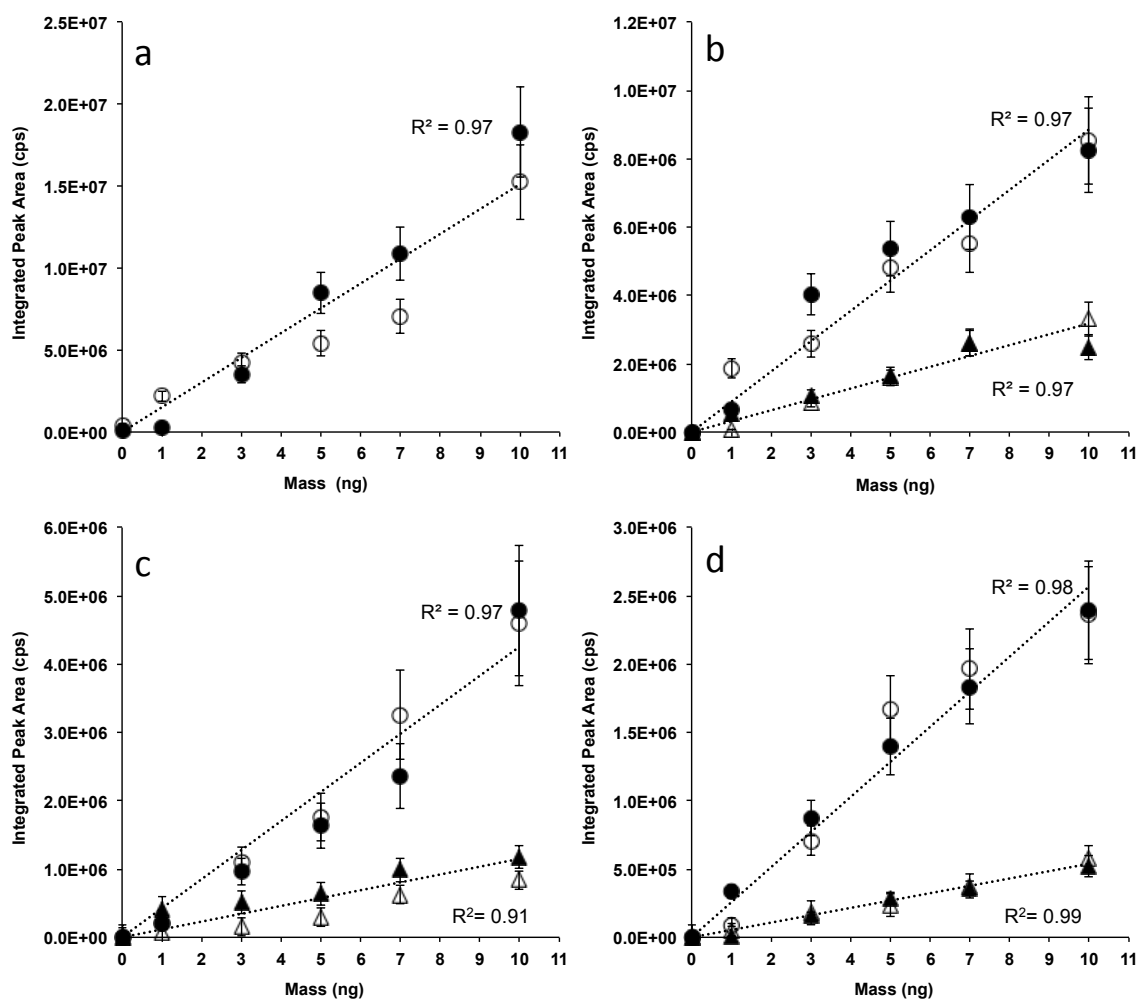


Figure 4. Collection efficiency for ammonium sulfate particles as a function of the voltage applied on the platinum wire. (A) and the nichrome coil (B). In (A), 10 nm (dashed lines) and 40 nm (solid lines) particles were collected with different exposed lengths of the EPC (relative to the tip of the EPC housing cylinder): 4 cm (solid triangles), 2 cm (open triangles), and 0 cm (open circles). In (B), 80 nm (solid squares), 100 nm (solid triangles), 150 nm (open circles), and 200 nm (open diamonds) particles were collected on the nichrome coil with a 4 cm exposed length.

For example, for 10 nm particles and 2 cm exposure length, a collection efficiency of greater than 70% is achieved at 1 kV, and for 40 nm particles and 4 cm exposure length, a collection efficiency of 60% is achieved at 3kV. On other hand, for a shorter exposure length and larger particles, a higher voltage ( $> 4\text{kV}$ ) is required to achieve a sufficient collect efficiency, but likely induces undesirable discharge within the collection chamber, which subsequently decreases the collection efficiency.

Similarly, for accumulation mode particles using the nichrome coil (Fig. 4B), the collection efficiency decreases with the increasing particle particles, but increases with increasing voltage at a fixed exposure length of 4 cm. For 80, 100, 150, and 200 nm particles at 3 kV, the collection efficiencies are 100, 75, 50, and 20%, respectively. For larger particles ( $> 200\text{ nm}$ ), a longer exposure length or a higher voltage is required to achieve a sufficient collection, and the higher voltage may cause discharge inside the collection chamber. Furthermore, the nichrome coil is unsuitable for collection of nucleation mode particles, possibly because of the combination of a smaller particle mass and complex geometry of the coil, leading to lower collection efficiency. Hence, our results demonstrate that a collection efficiency of larger than 50% is achieved with an exposure length of 4 cm and voltage of 3 kV using the platinum filament for the nucleation mode ( $\leq 40\text{ nm}$ ) particles and using the nichrome coil for accumulation mode (40-150 nm) particles. Those configurations were employed for all measurements of collected particles. Fig. 5 (a-d) shows the comparison of the integrated peak areas as a function of the particle masses between collected particles and syringe-deposited droplets.



**Figure 5.** Comparison of the integrated desorption peak areas between collected particles and syringe-deposited droplets of similar masses. (A) collected 40 nm sulfuric acid particles (open cycles) and syringe-deposited droplet (solid circles) using the  $\text{NO}_3^-$  reagent ion; (B) collected 40 nm sulfuric acid particles (open cycles), syringe-deposited droplet (solid circles), collected 40 nm succinic acid particles (open triangles), syringe-deposited succinic acid droplet (solid triangles) using the  $\text{CO}_3^-/\text{CO}_4^-$  reagent ion; (C) collected 200 nm ammonium sulfate particles (open cycles), syringe-deposited ammonium sulfate droplet (solid circles), collected 200 nm oleic acid particles (open triangles), syringe-deposited oleic acid droplet (solid triangles) using the  $\text{CO}_3^-/\text{CO}_4^-$  reagent ion; (D) collected 40 nm dimethylaminium sulfate particles (open cycles), syringe-deposited dimethylaminium sulfate droplet (solid circles), collected 40 nm dimethylaminium acetate particles (open triangles), syringe-deposited dimethylaminium acetate droplet (solid triangles) using the  $\text{H}_3\text{O}^+$  reagent ion. The lines represent linear regression over both collected particles and syringe-deposited samples for each species. Each point represents the average of three experiments, and the uncertainty reflects the random error of the measurements ( $1\sigma$ ).



Experiments were conducted with particles of different compositions (i.e., sulfuric acid, succinic acid, oleic acid, ammonium sulfate, oleic acid, dimethylaminium sulfate, and dimethylaminium acetate) and particle sizes (i.e., 40, and 200 nm) using the three reagent ions. The collected particle mass was estimated on the basis of the measured collection efficiency (Fig. 4), along with the particle size and density, and the flow rate in the collection chamber. For all measurements in Fig. 5, the correlation coefficients of the measured integrated peaks between collected particles and syringe-deposited droplets are in the range of 0.91 and 0.99, showing a good linearity between the desorption peak area and particle mass and agreement between those two methods.

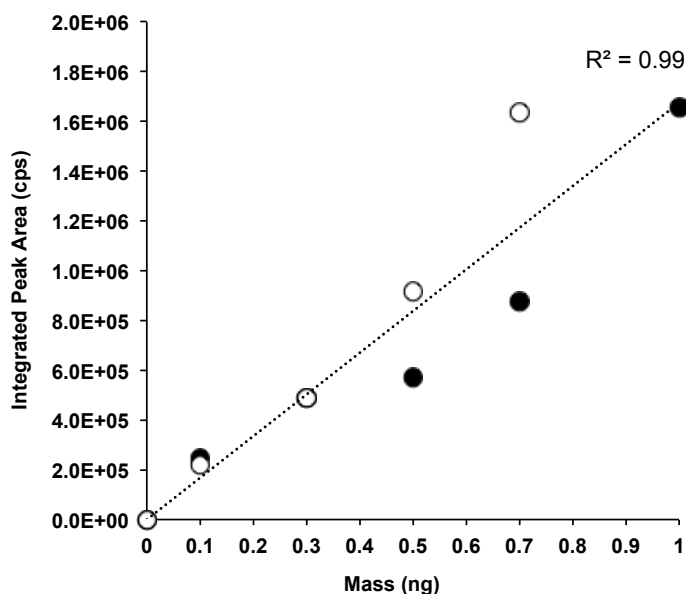


**Figure 6. Comparison of the integrated desorption peak areas between collected 10 nm particles and syringe-deposited droplets. Collected particles (open circles) and syringe-deposited droplet (solid circles) of ammonium sulfate using the  $\text{CO}_3^-/\text{CO}_4^-$  reagent ion. The lines represent linear regression over both collected particles and syringe-deposited samples.**

Figure 6 illustrates the correlation of collected particles and syringe-deposited calibrations, showing a linear correlation of 0.99 for the average of both sets for 10 nm ammonium sulfate particles using the  $\text{CO}_3^-/\text{CO}_4^-$  reagent ion scheme. The results also indicate that the sensitivity and detection limit obtained by using the syringe-deposited sample droplets are applicable to those for collected particles. In addition, such calibration demonstrates the capability of the TD-ID-CIMS instrument in quantifying aerosols from the nucleation to accumulation mode particles.

In our laboratory, we have also utilized our TD-ID-CIMS in other research projects aimed at studying the chemical composition and formation of SOA. Such projects include analysis of the chemical composition of critical nuclei clusters (2 nm particles) for new particle formation, chemical composition of alkylammonium carboxylate salts after evaporation, and acid-catalyzed reactions of epoxides for atmospheric particles growth. Here we provide a brief description of the application of TD-ID-CIMS in such projects to illustrate the analytical capabilities of our instrument in the study of SOA formation and composition.

## New Particle Formation Studies

Figure 7 shows mass spectra for 2 nm particles analyzed by TD-ID-CIMS. In our experiments,  $\alpha$ -pinene was oxidized by hydrogen peroxide inside a nucleation chamber yielding particles containing several organic compounds. The particles were generated in the nucleation chamber and collected on our platinum filament in our EPC for 3 hours. Particles were size selected by a nano-TDMA before entering our TD-ID-CIMS for analysis in the positive ion mode. For ionization, we utilized a proton transfer reaction ionization scheme.

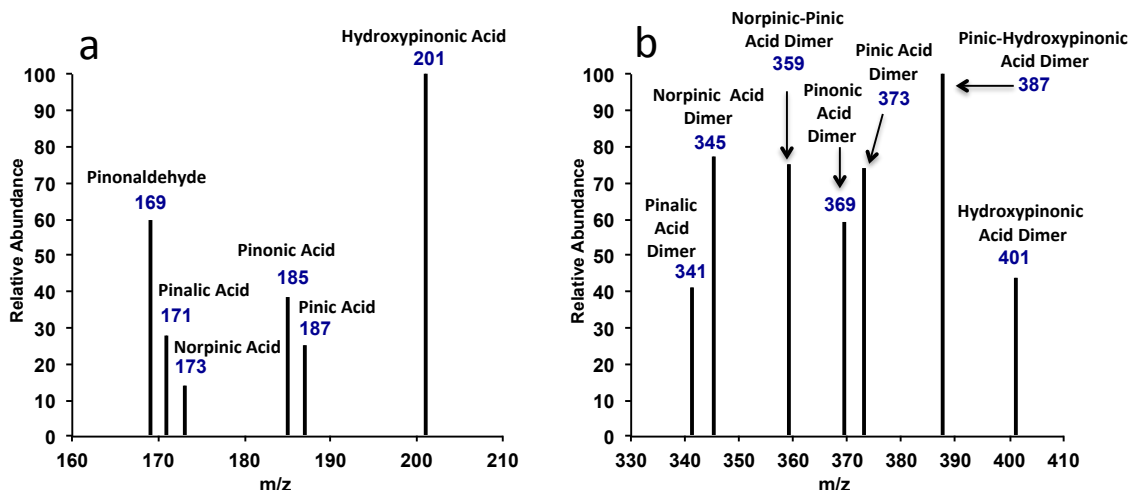


Figure 7. TD-ID-CIMS of 2 nm aerosol particles in the positive (+) ion mode. Analysis was performed utilizing proton transfer reaction (PTR-MS) ionization. Panel a depicts the monomer mass region. Panel b depicts the dimer mass region.

For example, Figure 7a illustrates the presence of different organic compounds generated by the oxidation of  $\alpha$ -Pinene. In the measurements, we have detected  $m/z = 169$ , which has been assigned to pinonaldehyde. In addition,  $m/z = 171, 173, 185, 187,$

and 201 correspond to pinalic, norpinic, pinonic, pinic, and hydroxypinonic acids respectively. Figure 7b depicts the mass region [ $m/z = 330-410$ ] of the dimers produced from the oxidation of  $\alpha$ -pinene in the chamber. Our TD-ID-CIMS analysis detected only the dimers of the organic acids, without detecting pinonaldehyde dimers. Furthermore, TD-ID-CIMS analysis shows the presence of both, homomolecular and heteromolecular acidic dimers, mainly for diprotic acids such as pinic and norpinic acid. These results highlight the analytical prowess of our TD-ID-CIMS, as it is the first instrument in the world that can successfully analyze the chemical composition of 2 nm aerosol particles. TD-ID-CIMS thus exploits the benefits of “soft” ionization generating mass spectrometry data with low fragmentation, and retention of the molecular structure of the analytes.

#### *Chemical Composition of Alkylammonium Carboxylates*

We have analyzed the chemical composition of alkylammonium salts after evaporation to elucidate their composition, volatility, and stability in the gas-phase as part of a study in collaboration with Lavi et al.<sup>51</sup> Briefly, a 1.5  $\mu$ L droplet of the salt solution was deposited on a platinum filament and dried with a stream of dry nitrogen. The filament was then subjected to resistive heating up to 600 K to evaporate the deposited sample. The hydronium ions ( $H_3O^+$ ) were employed for the proton-transfer reactions in the drift tube, and the reagent and products were detected using CIMS.

Figure 8 depicts the TD-ID-CIMS spectrum of dimethylammonium adipate, which consists of adipic acid (MW 146.14 g/mol) and two dimethylamine (MW 45.08 g/mol)

entities. The presence of the  $[\text{adipic acid}+2\text{DMA}+\text{H}]^+$  ion at  $m/z$  237, is clear even after the salt was evaporated up to 600 K. In addition,  $[\text{adipic acid}+\text{DMA}+\text{H}]^+$  at  $m/z$  192 having a higher intensity than that of  $[\text{adipic acid}+\text{H}]^+$  at  $m/z$  147 was observed. Interestingly, we also observed a signal at  $m/z$  165, which corresponds to the  $[\text{adipic acid}+\text{H}_2\text{O}+\text{H}]^+$  ion. Therefore, the presence of the salt ions in the mass spectrum suggests that the salt is stable after vaporization.

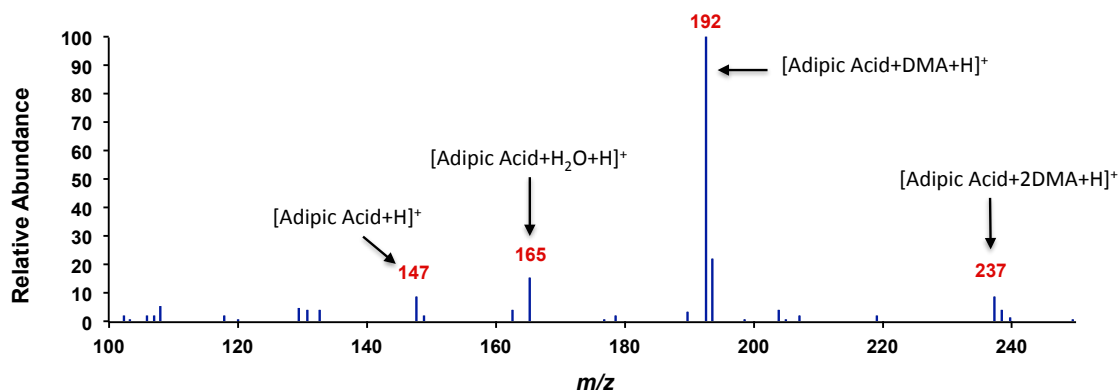


**Figure 8.** TD-ID-CIMS analysis of adipic acid:DMA salt solution in the positive ion mode. The  $m/z$  147 signal corresponds to  $[\text{adipic acid}+\text{H}]^+$ , while the peak at  $m/z$  165 corresponds to  $[\text{adipic acid}+\text{H}_2\text{O}+\text{H}]^+$ , mass at  $m/z$  192 corresponds to  $[\text{adipic acid}+\text{DMA}+\text{H}]^+$ , and mass at  $m/z$  237 corresponds to  $[\text{adipic acid}+2\text{DMA}+\text{H}]^+$ .

Figure 9 illustrates the TD-ID-CIMS spectrum of dimethylaminium azelate, which consists of azelaic acid (MW 188.22 g/mol) and two dimethylamine (MW 45.08 g/mol) entities. The obtained spectrum shows the presence of  $[\text{azelagic acid}+\text{DMA}+\text{H}]^+$  at  $m/z$  234, confirming the presence of the salt in the gas phase. For the azelaic acid:DMA salt, three major peaks were observed:  $[\text{azelagic acid}+\text{H}]^+$  at  $m/z$  189,  $[\text{azelagic acid}+\text{H}_2\text{O}+\text{H}]^+$  at  $m/z$  207, and  $[\text{azelagic acid}-\text{H}_2\text{O}+\text{H}]^+$  at  $m/z$  171. The presence of the  $[\text{azelagic acid}+\text{DMA}+\text{H}]^+$  ion suggests that the alkylaminium carboxylate salt (2:1) is

stable after thermal desorption even though  $m/z$  279 corresponding to the  $[\text{azelaic acid}+2\text{DMA}+\text{H}]^+$  ion is absent. The absence of  $m/z$  279 may be attributed to lack of proton transfer from the  $\text{H}_3\text{O}^+$  reagent ion to the azelaic acid+2DMA. Our mass spectrometry results show little impurities in the samples after evaporation. Hence, we suggest that the alkylaluminium dicarboxylate salts are stable after evaporation.

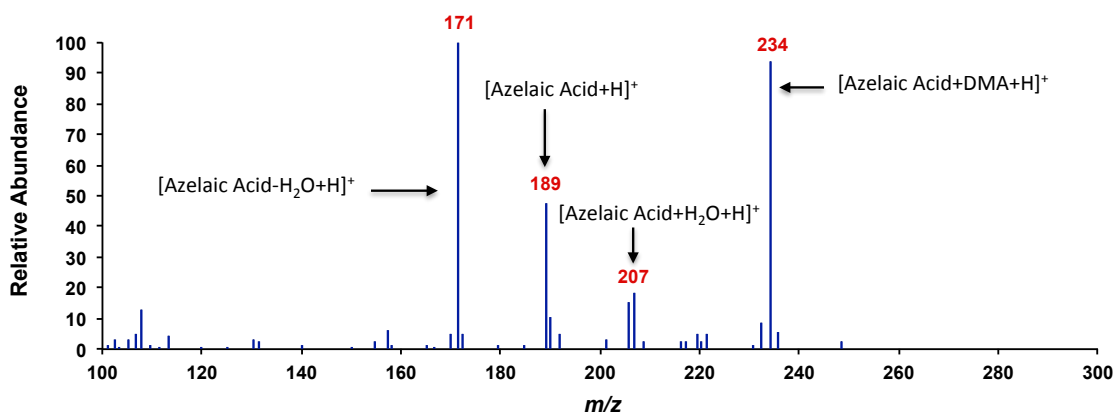


**Figure 9.** TD-ID-CIMS analysis of azelaic acid:DMA salt solution in the positive ion mode. The peak at  $m/z$  171 corresponds to  $[\text{azelaic acid}-\text{H}_2\text{O}+\text{H}]^+$ , while the signal at  $m/z$  189 corresponds to  $[\text{azelaic acid}+\text{H}]^+$ , signal at  $m/z$  207 corresponds to  $[\text{azelaic acid}+\text{H}_2\text{O}+\text{H}]^+$ , and at  $m/z$  234 corresponds to  $[\text{azelaic acid}+\text{DMA}+\text{H}]^+$ .

Our TD-ID-CIMS results indicate that both, dimethylaluminium adipate and dimethylaluminium azelate are stable in the gas-phase without decomposing into the acid and base precursors. Therefore, our TD-ID-CIMS instrument has the capabilities to analyze not only collected particles, but also samples composed of SOA precursors in the liquid phase loaded unto the injection port.

*Acid-Catalyzed Reactions of Epoxides for Atmospheric Particle Growth*

We have also utilized our TD-ID-CIMS for the analysis of acid-catalyzed reactions of epoxides for atmospheric nanoparticle growth.<sup>49</sup> Figure 10 depicts the TD-ID-CIMS spectra of 20 nm sulfuric acid nanoparticles collected on a platinum filament after the exposure to isoprene oxide.

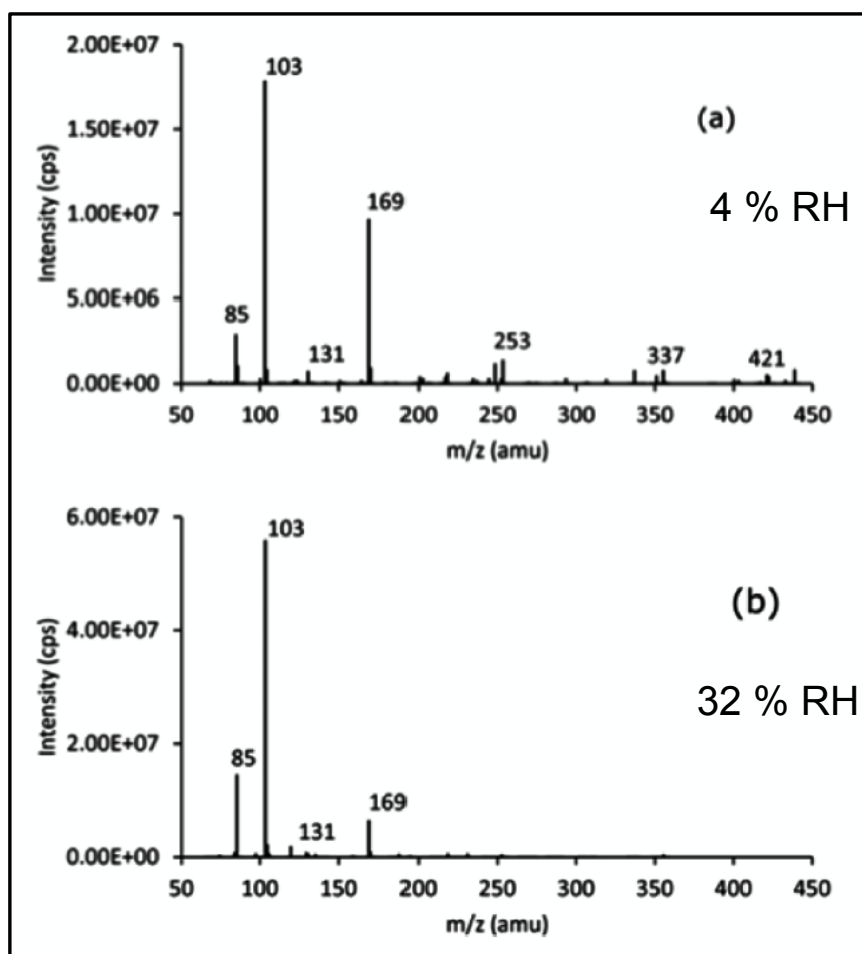


Figure 10. TD-ID-CIMS analysis of 20 nm sulfuric acid particles after exposure to isoprene oxide. Panel (a) shows results at 4 % RH. Panel (b) shows results at 32% RH.

The peak assignments for the products heterogeneous reactions of epoxides on sulfuric acid nanoparticles are summarized in Table 2.

**Table 2. Structure assignment for detected ions by TD-ID-CIMS in 20 nm sulfuric acid particles after exposure to isoprene oxide vapor.**

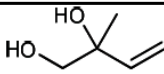
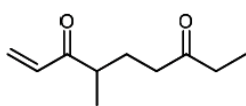
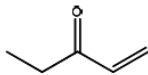
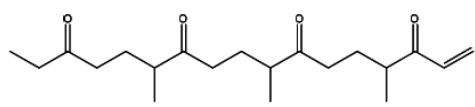
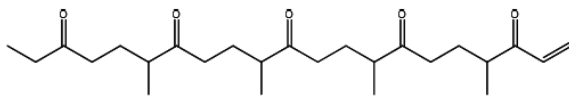
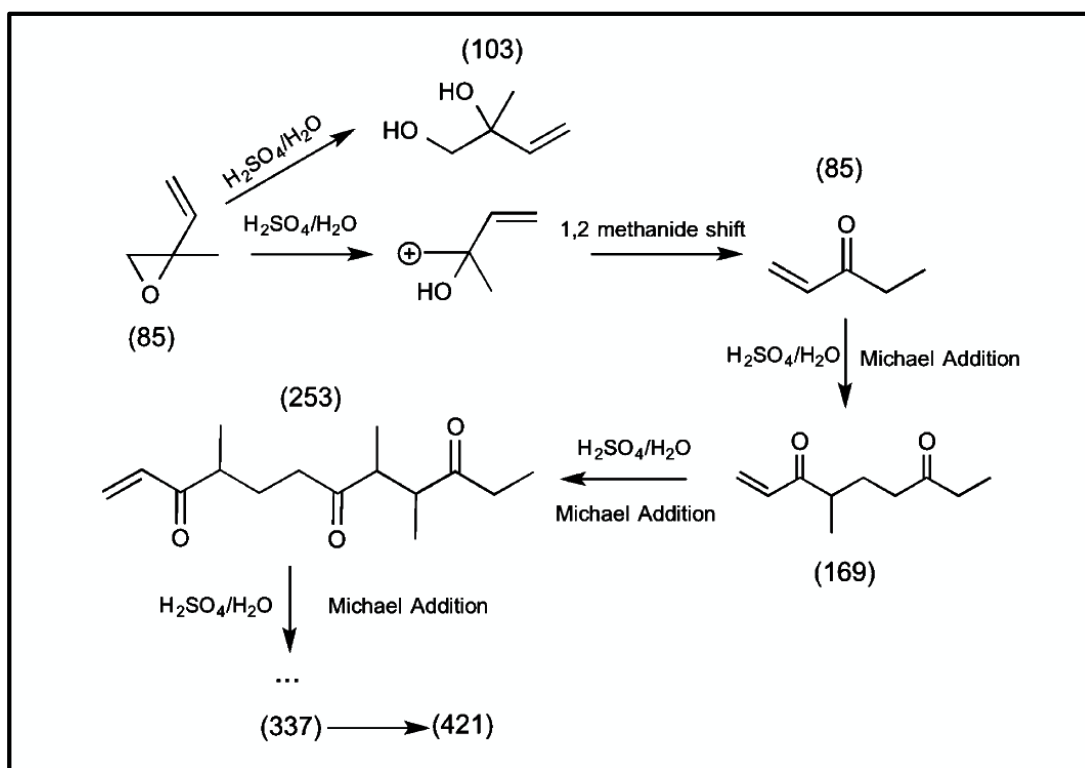
Isoprene oxide	103	
(a) and (b)	169	
	85	
	337	
	421	

Figure 11 depicts the reaction leading to polymerization from isoprene oxide, the  $\alpha,\beta$ -unsaturated ketone formed through 1,2-methanide shift polymerizes via the Michael addition in the presence of sulfuric acid,<sup>54</sup> and the resulting polymers are detected by the TD-ID-CIMS at  $m/z$  of 169, 253, 337, and 421 for dimer, trimer, tetramer, and pentamer, respectively. Organosulfates are not identified for isoprene oxide, since their formation is suppressed by polymerization.





**Figure 11. Mechanism for the formation of polymers in sulfuric acid particles after exposure to isoprene oxide.**

In the acid-catalyzed reactions of epoxides for atmospheric nanoparticle growth we also utilized our TD-ID-CIMS to analyze the composition of sulfuric acid nanoparticles after exposure to budatiene diepoxide, and  $\alpha$ -pinene oxide. A full discussion can be found in the recent contribution by Xu et al.<sup>49</sup>

These three recent applications of our TD-ID-CIMS showcase the capabilities of our new analytical technique to conduct cutting-edge measurements for the analysis of SOA composition and formation.

## Summary

We have described the design and calibration of a TD-ID-CIMS instrument, which consists of a combined atomizer, DMA, and CPC system, an EPC, and ID-CIMS. Particles generated by the atomizer are charged and size-selected by the DMA, electrostatically deposited on and resistively evaporated by the EPC, and subsequently ionized and analyzed by the ID-CIMS. Experimental results are presented to evaluate the performance and to establish the collection efficiency, sensitivity, and detection limit of the instrument for a broad range of particle sizes and chemical compositions using various reagent ions.

In our instrument, high collection efficiency ( $> 50\%$ ) is achieved for both nucleation and accumulation particles (10-150 nm) using a platinum wire and a nichrome coil, respectively. The TD-ID-CIMS exhibits soft desorption and ionization for most organic (six organic acids) and inorganic (sulfuric acid, ammonium sulfate, and ammonium bisulfate) compounds, since those species are selectively ionized by the reagent ions ( $\text{CO}_3^-/\text{CO}_4^-$ ,  $\text{NO}_3^-$ , or  $\text{H}_3\text{O}^+$ ) with little fragmentation (with the exception for dimethylammonium sulfate and acetate using  $\text{H}_3\text{O}^+$ ). Calibration of collected particles and syringe-deposited droplets shows a marked agreement, illustrating the highly quantitative feature of the instrument.

Our results reveal that the TD-ID-CIMS instrument is capable of analyzing and quantifying nucleation to accumulation mode particles, with the advantages of soft vaporization and ionization and high collection efficiency, selectivity, and sensitivity for a variety of organic and inorganic species down to sub-nanogram levels. Ongoing work

in our group includes quantification of collected particles on the basis of the ion-molecule rate constants theoretically determined for various organic and inorganic species and ambient monitoring of aerosols using the TD-ID-CIMS method.

We have also demonstrated the capabilities of TD-ID-CIMS to analyze aerosols in laboratory studies regarding new particle formation, chemical composition of alkylammonium carboxylates, and acid-catalyzed reactions of epoxides for atmospheric nanoparticle growth. For the new particle formation studies, our TD-ID-CIMS has successfully collected particles as small as 2 nm, produced from chamber experiments. Our results show the formation of several weak organic acids present in the collected particles as result of the oxidation of alpha-pinene by hydrogen peroxide. In addition, the TD-ID-CIMS has confirmed that alkylammonium carboxylates evaporate as molecular complexes, without decomposing into the acid and base components. Finally, we have demonstrated that the mechanism for the acid-catalyzed reactions of epoxides are dependent on relative humidity, thereby impacting the formation of organosulfates and polymers, which may lead to particle growth and formation of SOA. Overall, the TD-ID-CIMS offers a versatile, robust, and sensitive platform for the study of atmospheric aerosols.

CHAPTER III  
HETEROGENEOUS CHEMISTRY OF GLYOXAL ON ACIDIC SOLUTIONS  
AN OLIGOMERIZATION PATHWAY FOR SECONDARY ORGANIC  
AEROSOL FORMATION\*

**Introduction**

In addition to his pioneering work in the understanding of stratospheric ozone depletion by man-made chlorofluorocarbons (CFCs) and atmospheric chemistry in general,<sup>55,56</sup> Mario J. Molina's research has made fundamental advances to the aerosol chemistry both in the troposphere<sup>57</sup> and stratosphere.<sup>58,59</sup> Atmospheric aerosols exert important impacts on visibility, human health, air quality, weather, and climate.<sup>60</sup> In particular, aerosols modify the Earth's energy budget directly by scattering and absorbing the incoming solar radiation and indirectly by modifying cloud formation. Currently, the direct and indirect radiative effects of aerosols represent the largest uncertainty in projections of future climate by atmospheric models.<sup>19,21,60</sup> Part of the uncertainty in assessing the aerosol radiative forcings is attributable to the complex processes leading to aerosol formation: the current understanding of the formation mechanisms of atmospheric aerosols is highly limited.<sup>1,7</sup>

Aerosols can be directly emitted (primary) or formed through the gas-particle conversion process (secondary) in the atmosphere. The primary aerosol sources include

---

\* This chapter is reprinted with permission from Gomez, M.E.; Lin, Y.; Guo, S.; Zhang, R. Heterogeneous Chemistry of Glyoxal on Acidic Solutions. An Oligomerization Pathway for Secondary Organic Aerosol Formation. *The Journal of Physical Chemistry A*. **2015**, 119 (19), pp. 4457–4463. Copyright 2015 American Chemical Society.

emissions from combustion, road or wind-blown dust, and plants, while the secondary formation processes include nucleation and growth by multi-phase chemical processes. Previous studies have shown that heterogeneous reactions of organic molecules, such as alkylamines, epoxides, and carbonyls, may contribute significantly to formation of secondary organic aerosols (SOA) by acid-base, acid-catalyzed, and hydration reactions, respectively.<sup>23,24,58,61-64</sup> For example, smaller  $\alpha$ -dicarbonyls (i.e., glyoxal and methylglyoxal) have been shown to form from atmospheric photochemical oxidations of anthropogenic (toluene, xylenes, or trimethylbenzenes) and biogenic (isoprene) hydrocarbons and to participate in the SOA formation.<sup>46,65-72</sup> Formation of glyoxal has been suggested as the consequence of the oxidation-driven ring fragmentation of aromatic hydrocarbons<sup>46,69-72</sup> and the oxidation of isoprene.<sup>73,74</sup> The gas-phase concentrations of glyoxal have been reported to range from less than 20 to 350 parts per trillions (ppt) in rural areas and from 0.15 to 2 parts per billions (ppb) in urban areas,<sup>75-77</sup> and the global source of glyoxal is estimated at 45 Tg yr<sup>-1</sup> (ref 78). The gas-phase chemistry of glyoxal includes photolysis and the reaction with OH, leading to an atmospheric lifetime of a few hours.<sup>77</sup> Other possible loss processes of glyoxal include dry deposition and heterogeneous reactions on aerosol surfaces. For example, the presence of glyoxal in the particle-phase has been identified from atmospheric field measurements.<sup>68</sup> Fu et al. have calculated a global SOA source of 2.6 TgC yr<sup>-1</sup> from the irreversible uptake of glyoxal, with up to 90 % resulted from cloud processing.<sup>78</sup> In addition, the measured glyoxal concentrations in Mexico City have been shown to be

significantly below those predicted, indicating a possible missing sink for gas-phase glyoxal that is likely linked to SOA.<sup>79</sup>

Several laboratory studies have investigated the heterogeneous interaction of glyoxal with atmospheric particulate matter.<sup>80-90</sup> A previous study by Ip et al.<sup>80</sup> has reported the effective Henry's Law constant ( $H^*$ ) of  $1.6 \times 10^6 \text{ M atm}^{-1}$  for glyoxal in water at neutral pH and at 278 K, whereas the  $H^*$  value decreases to  $4.2 \times 10^5$ ,  $1.5 \times 10^5$ ,  $5.0 \times 10^4 \text{ M atm}^{-1}$  at 298, 308, 318 K, respectively. The uptake coefficient ( $\gamma$ ) of glyoxal on aqueous aerosols and liquid droplets has also been investigated. For example, previous laboratory studies have measured the  $\gamma$  values of  $8 \times 10^{-4}$  to  $7.3 \times 10^{-3}$  on aqueous inorganic aerosols<sup>88</sup> and  $1 \times 10^{-3}$  to  $2 \times 10^{-2}$  on cloud droplets/ice crystals,<sup>89</sup> with a larger  $\gamma$  on more acidic particles ( $> 2.3 \times 10^{-3}$ ) and at a lower temperature ( $> 10^{-3}$ ). In addition, Zhou et al.<sup>87</sup> have studied the formation of gas-phase carbonyls as products of the heterogeneous oxidation of polyunsaturated fatty acids in the air-water interface and the sea surface microlayer. In our previous experiments, the uptake of methylglyoxal on liquid sulfuric acid has been measured at different temperatures and relative humidities, showing a reaction mechanism of hydration and oligomerization that increases with decreasing acidity and temperature.<sup>63</sup>

In this study, we have investigated the heterogeneous interaction of glyoxal on liquid sulfuric acid surfaces, a relevant model system for atmospheric aerosols. The uptake coefficient,  $\gamma$ , and effective Henry's Law constant,  $H^*$ , of glyoxal have been measured on 60-93 wt %  $\text{H}_2\text{SO}_4$  and in the temperature range of 253-273 K. Our measurements provide an elucidation on the kinetics and mechanism of glyoxal uptake

on aqueous acidic solutions. The atmospheric implications of our experimental results are discussed.

## Experimental

The uptake experiments were performed using a low-pressure laminar fast flow reactor coupled to an ion drift - chemical ionization mass spectrometer (ID-CIMS),<sup>47</sup> similar to those employed in our previous studies.<sup>23,61-64</sup> Figure 12 provides a schematic representation of the experimental setup.

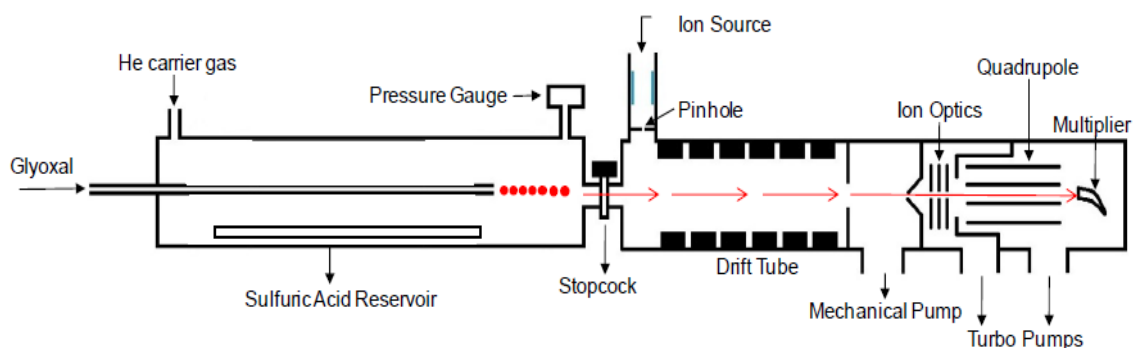


**Figure 12. Schematic illustration of the low-pressure fast flow reactor coupled to an ID-CIMS instrument.**

Glyoxal with a concentration of 100 ppm (parts per million) was prepared in a 4 L glass bulb pressurized to 800 Torr, and was introduced into the flow reactor by a moveable 45 cm long stainless steel tubing. Aqueous sulfuric acid solutions were deposited on a semicircular Pyrex® glass reservoir of 15 cm long, 2 cm wide, and 0.7 cm deep to provide a flat liquid surface with the acid concentrations between 60 - 93 wt %. The inner diameter and the length of the low-pressure laminar fast flow reactor were

1.25 and 50 cm, respectively. The temperature of the flow reactor was maintained and controlled by circulating methylene glycol through the outer jacket of the flow reactor, isolated from room temperature using insulating foam. All carrier gas flows were monitored utilizing calibrated electronic mass flow meters. The flow reactor was operated at a pressure of 2.5 Torr with a flow average velocity of  $856 \text{ cm s}^{-1}$ , and the typical flow rate in the flow reactor was maintained at 3 SLPM (standard liter per minute) for helium. The composition of the acid solutions was checked before and after experiments by titration with standardized sodium hydroxide. Commercially available glyoxal trimer dihydrate (Aldrich) was processed to produce pure glyoxal monomer. Briefly, glyoxal trimer dihydrate 97% (GTD) reacted with phosphorous pentoxide ( $\text{P}_2\text{O}_5$ ) in a 150 mL round bottom flask heated for 45 minutes. The flask was directly connected to a solid salt trap with 50% potassium carbonate ( $\text{K}_2\text{CO}_3$ ) and 50% phosphorous pentoxide ( $\text{P}_2\text{O}_5$ ) to dry the glyoxal sample. A flow containing glyoxal was then directed to a cold trap (a 3 way glass bubbler) immersed in liquid nitrogen ( $\text{N}_2$ ) and the glyoxal sample was allowed to condense. After removal from the liquid nitrogen reservoir, the cold trap was immersed in an acetone/dry ice bath for 2 hours to remove impurities. The final glyoxal sample was in a green crystalline form deposited in the bottom of the cold trap. The glyoxal sample was then stored in a freezer at  $-20^\circ\text{C}$ . The 4 L glass bulb containing gaseous glyoxal was prepared by successive dilutions of the glyoxal vapor with high purity helium, down to 100 ppm.

Glyoxal was detected by the ID-CIMS to obtain the kinetic data upon exposing glyoxal to the sulfuric acid surfaces. The oxygen reagent anion ( $\text{O}_2^-$ ), formed by using a



corona discharge device, ionized glyoxal to produce the glyoxal-oxygen adduct ion ( $\text{O}_2^- \cdot \text{C}_2\text{O}_2\text{H}_2$  at  $m/z = 90.4$ ), which was subsequently detected by ID-CIMS. The ion-molecule reactions took place in the drift tube at a low pressure of  $< 2.5$  Torr. The glyoxal-oxygen adduct ion signal at  $m/z = 90.4$  was monitored in real time as glyoxal molecules were injected into the system. The stainless steel injector was retracted over an increasing area of sulfuric acid, allowing glyoxal molecules to be exposed to the sulfuric acid surfaces. Subsequently, the ionograms were recorded and processed. From the changes in the glyoxal signal after sulfuric acid exposure monitored by the ID-CIMS, the time-dependent uptake coefficient  $\gamma(t)$  of glyoxal on sulfuric acid is calculated:<sup>45,91-92</sup>

$$\gamma(t) = \frac{4k}{\omega} \left( \frac{V}{A} \right) \quad (3.1)$$

where  $k$  is the first-order rate coefficient,  $V$  is the internal volume of the flow reactor,  $A$  represents the geometric area of the exposed acid liquid, and  $\omega$  is the molecular mean thermal speed. The effective Henry's Law constant,  $H^*$ , is determined from the time-dependent uptake coefficient:

$$\frac{1}{\gamma(t)} = a + bt^{1/2} \quad (3.2)$$

where  $a$  is a constant that parameterizes the accommodation coefficient and the time-independent aqueous reaction rate constant and  $b = \omega/4H^*RT(D_l/\pi)^{1/2}$ . Hence, equation 2 allows the calculation of  $H^*$  from the time-dependent uptake coefficient, where  $D_l$  is the liquid-phase diffusion coefficient,  $R$  is the gas constant, and  $T$  is the temperature. The liquid-phase diffusion coefficient  $D_l$  is calculated following Klassen et al.<sup>93</sup> All

measurements were repeated at least 3 times to obtain the experimental random error ( $1\sigma$ ). The estimated systematic uncertainty in our measurements was about  $\pm 30\%$ .

## Results and Discussion

Figure 13 illustrates a typical experiment of glyoxal uptake on sulfuric acid solution of 75 wt % at 253 K.

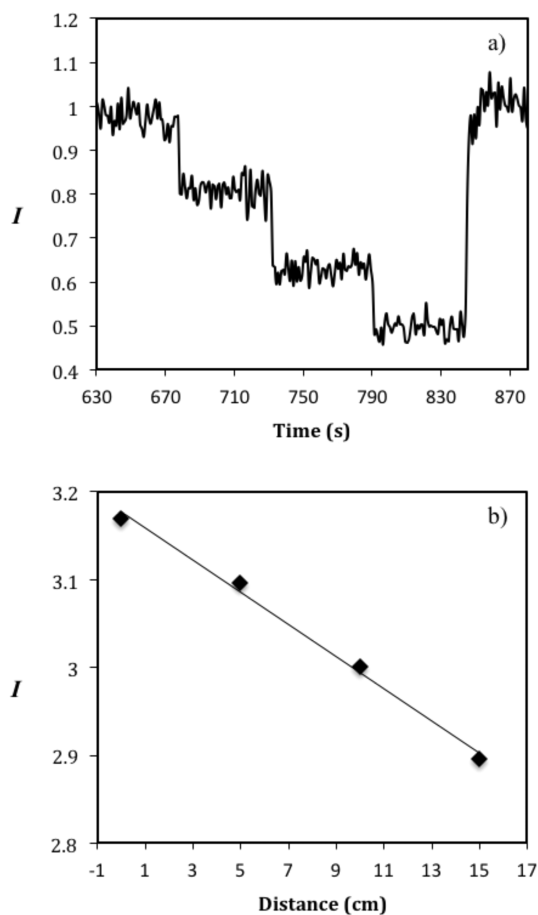
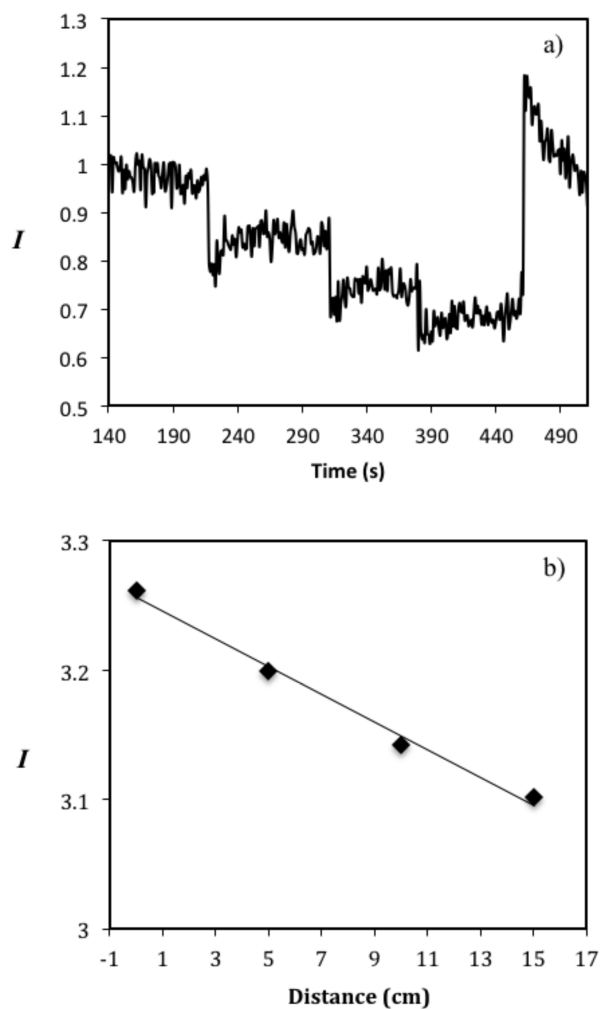


Figure 13. (a) Temporal profile ( $I$ , relative intensity) of glyoxal when exposed to a 15 cm long vessel containing 75 wt % sulfuric acid at 253 K. Each drop in the signal corresponds to a 5 cm distance increment from 0 to 15 cm. The experiment is terminated by retracting the injector to its original position after approximately 150 seconds. (b) The signal intensity of glyoxal as a function of injector distance for the experiment shown in panel (a).

As the injector is retracted successively, the glyoxal signal decreases stepwise as a function of the exposure length. The glyoxal signal does not recover at each exposure distance. After the injector is pushed to its original position, the glyoxal signal returns to the original level without desorption. Hence, the uptake of glyoxal on 75 wt% H<sub>2</sub>SO<sub>4</sub> at 253 K is characteristic of an irreversible reaction. Figure 13b shows a linear relation between the glyoxal signal intensity (*I*, arbitrary units) and the injector position, yielding a  $\gamma$  value of  $1.03 \times 10^{-2}$  for glyoxal uptake on 75 wt % H<sub>2</sub>SO<sub>4</sub> at 253 K.

In contrast, as the temperature increases, the uptake profile shows an increasingly reversible character. As depicted in Figure 14a for glyoxal uptake by a 75 wt% H<sub>2</sub>SO<sub>4</sub> solution at 273 K, the glyoxal signal at each exposure distance shows a significant recovery. After the experiment is terminated and the injector is returned to its original position, a desorption peak is observed before the glyoxal signal returns to its original level.

Figure 14b also shows a linear relation between stabilized glyoxal signal at each step and the injector position, yielding a  $\gamma$  value of  $5.26 \times 10^{-3}$  for 75 wt % H<sub>2</sub>SO<sub>4</sub> at 273 K. For more diluted solutions (i.e., 60 wt %), the uptake exhibits little reversible behavior, even at 273 K. In contrast, reversible uptake pattern is consistently observed for experiments performed on concentrated H<sub>2</sub>SO<sub>4</sub> (75-93 wt %) at the temperatures of 263-273 K.



**Figure 14. (a) Temporal profile ( $I$ , relative intensity) of glyoxal when exposed to a 15 cm long vessel containing 75 wt % sulfuric acid at 273 K. Each drop in the signal corresponds to a 5 cm distance increment from 0 to 15 cm. The experiment is terminated by retracting the injector to its original position after approximately 250 seconds. (b) The signal intensity of glyoxal as a function of injector distance for the experiment shown in panel (a).**

Figure 15 depicts the measured uptake coefficient of glyoxal on different sulfuric acid concentrations and at various temperatures. As shown in Figure 15, the measured  $\gamma$  value increases when the acid becomes more dilute and temperature is lower. The highest uptake coefficient of  $1.2 \times 10^{-2}$  is measured for 60 wt %  $\text{H}_2\text{SO}_4$  at 253 K, and the lowest value of  $2.5 \times 10^{-3}$  is measured for 93 wt %  $\text{H}_2\text{SO}_4$  at 273 K. For 60-93 wt %

solutions at 253 K, the uptake is irreversible, and the decay in the glyoxal signal follows pseudo-first-order kinetics with the time independent  $\gamma$  values of  $1.2 \times 10^{-2}$  to  $6.2 \times 10^{-3}$ , respectively.

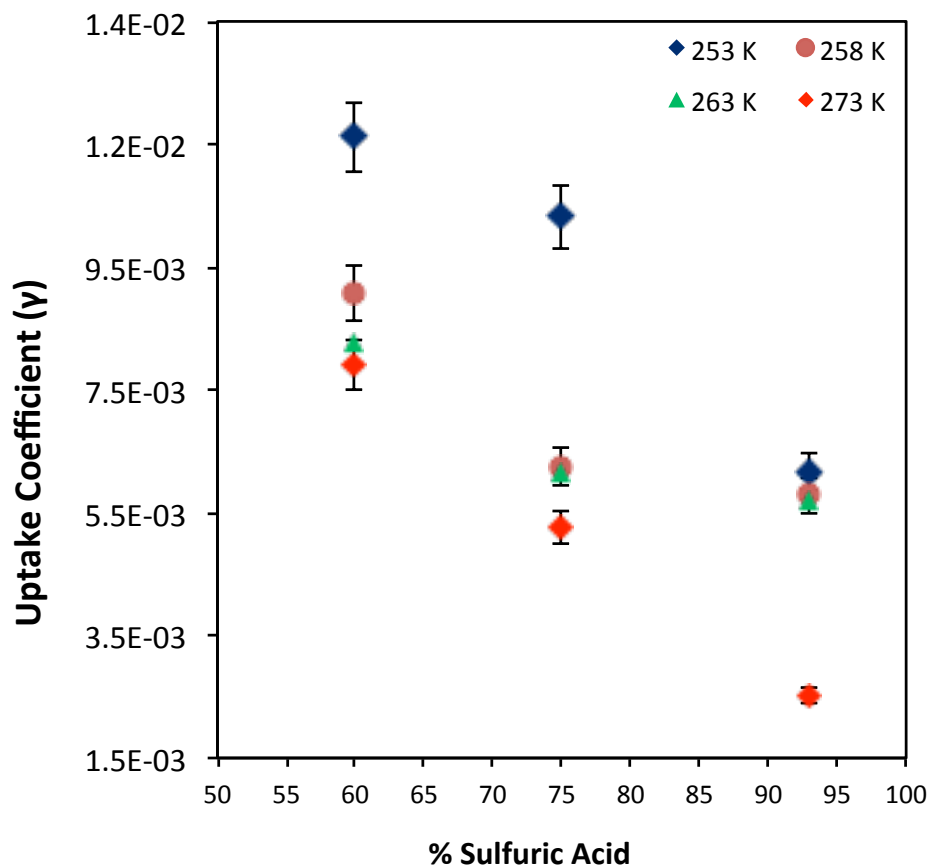


**Figure 15.** Concentration dependence of the uptake coefficient ( $\gamma$ ) of glyoxal on sulfuric acid for 60, 75, and 93 wt %  $\text{H}_2\text{SO}_4$  solutions at various temperatures. Blue diamonds, brown circles, green triangles, and red diamond correspond to measurements at 253, 258, 263, and 273 K, respectively. The error corresponds to one standard deviation ( $1\sigma$ ) for at least three uptake experiments.

For 60 and 93 wt % solutions at 258 K, the uptake coefficient decreases to  $9.1 \times 10^{-3}$  and  $5.8 \times 10^{-3}$ , respectively. The measurements of  $\gamma$  values are also summarized in Table 3.

**Table 3. Uptake coefficient ( $\gamma$ ) for the heterogeneous reaction of glyoxal on sulfuric acid for 60-93 wt% H<sub>2</sub>SO<sub>4</sub> solutions at 253 to 273 K.**

H <sub>2</sub> SO <sub>4</sub> %	T (K)	Uptake Coefficient ( $\gamma$ )
60	253	$1.2 \times 10^{-2} \pm 6 \times 10^{-4}$
75	253	$1.0 \times 10^{-2} \pm 5 \times 10^{-4}$
93	253	$6.2 \times 10^{-3} \pm 3 \times 10^{-4}$
60	258	$9.1 \times 10^{-3} \pm 4 \times 10^{-4}$
75	258	$6.3 \times 10^{-3} \pm 3 \times 10^{-4}$
93	258	$5.8 \times 10^{-3} \pm 3 \times 10^{-4}$
60	263	$8.3 \times 10^{-3} \pm 4 \times 10^{-4}$
75	263	$6.2 \times 10^{-3} \pm 3 \times 10^{-4}$
93	263	$5.7 \times 10^{-3} \pm 3 \times 10^{-4}$
60	273	$7.9 \times 10^{-3} \pm 4 \times 10^{-4}$
75	273	$5.3 \times 10^{-3} \pm 3 \times 10^{-4}$
93	273	$2.5 \times 10^{-3} \pm 1 \times 10^{-4}$

*The error corresponds to one standard deviation ( $1\sigma$ ) for at least three uptake experiments.*

Parts a and b of Figure 16 show time-dependent uptake measurements on 60 and 75 wt % solutions at 273 K, respectively. The time-dependent uptake coefficients are plotted to obtain the correlation of the inverse of  $\gamma$  as a function of the square root of the exposure time in Figure 16 c and d. From the slope of each linear regression, the  $H^*$  values at different temperatures and acid concentrations are calculated. According to Figure 16, the  $H^*$  values of  $1.7 \times 10^5$  and  $20.4 \times 10^5 \text{ M atm}^{-1}$  are derived for 75 and 60 wt % solutions at 273 K, respectively.

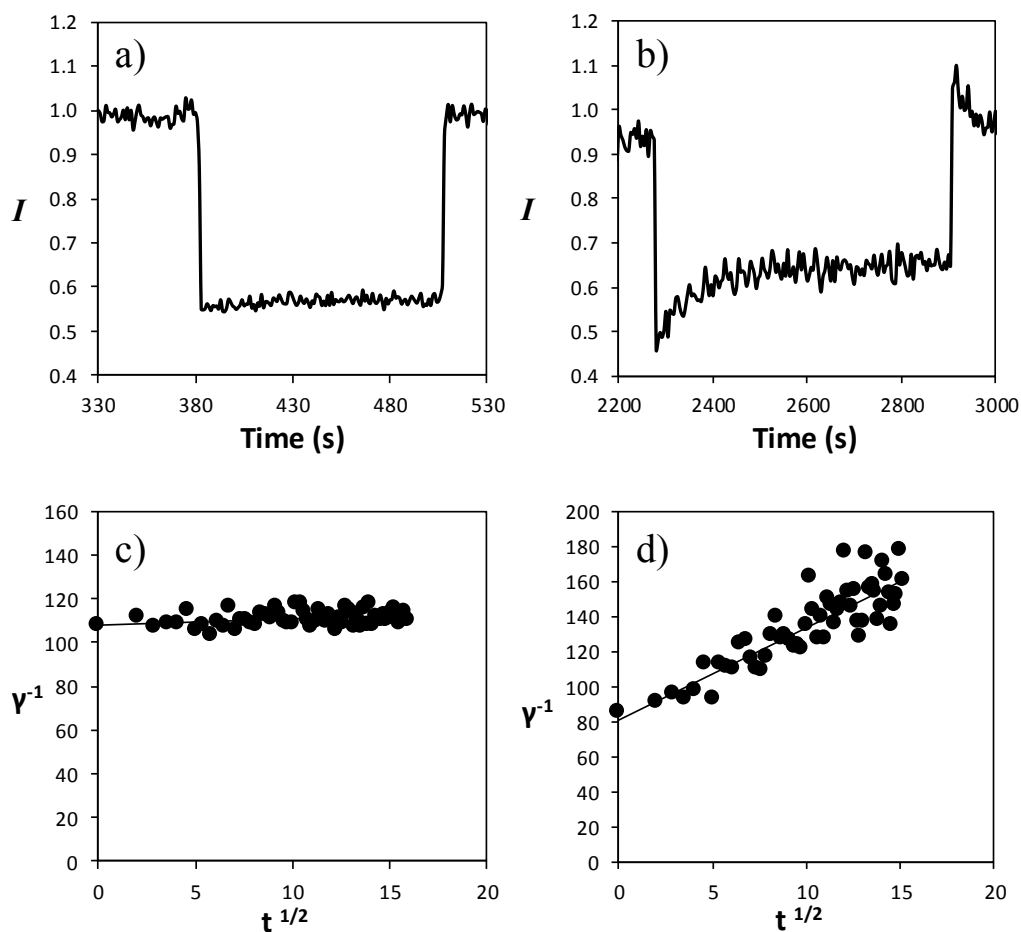


**Figure 16. (a) and (b):** Temporal profiles ( $I$ , relative intensity) of glyoxal when exposed to a 15 cm length of a vessel containing 60 and 75 wt % sulfuric acid at 273 K, respectively. (c) to (d): Plots of  $1/\gamma$  vs  $t^{1/2}$  for the temporal profiles in (a) and (b), respectively, for the exposure of the glyoxal to the acid reservoir. The lines are the linear least-square fit for each experiment.

The measurements of the  $H^*$  values are summarized in Table 4. For the 60 wt % solution, the  $H^*$  values are  $98.9 \times 10^5$  and  $20.4 \times 10^5$  M atm<sup>-1</sup> at 263 and 273 K, respectively, whereas for the 70 wt % solution the  $H^*$  values are  $60.3 \times 10^5$  and  $4.2 \times 10^5$  M atm<sup>-1</sup> at 263 and 273 K, respectively. Clearly, the measured  $H^*$  values also increase with decreasing acidity and temperature, similarly to the  $\gamma$  values.

**Table 4. Values of the  $H^*$  for glyoxal on sulfuric acid for 60-93 wt%  $H_2SO_4$  solutions at 263 and 273 K.**

$H_2SO_4$ %	T (K)	$H^*$ ( $\times 10^5$ M atm <sup>-1</sup> )
60	263	98.9 $\pm$ 4.9
70	263	60.3 $\pm$ 3.0
75	263	11.3 $\pm$ 0.6
93	263	9.9 $\pm$ 0.5
60	273	20.4 $\pm$ 1.0
70	273	4.2 $\pm$ 0.2
75	273	1.7 $\pm$ 0.1
93	273	1.6 $\pm$ 0.1

*The error corresponds to one standard deviation ( $1\sigma$ ) for at least three uptake experiments.*

Hence, our measurements show that both the uptake coefficient and Henry's Law constant for glyoxal on sulfuric acid exhibit a similar dependence with the acid concentration and temperature, consistent with our previous measurements of methylglyoxal uptake on sulfuric acid.<sup>63</sup> For comparison, the previously measured  $\gamma$  value of  $7.6 \times 10^{-3}$  for 58 wt % at 253 K and  $H^*$  value of  $15.2 \times 10^3$  M atm<sup>-1</sup> for 69 wt % at 273 K for the uptake of methylglyoxal on sulfuric acid are smaller than those values of  $1.2 \times 10^{-2}$  for 60 wt % at 253 K and  $60.3 \times 10^5$  M atm<sup>-1</sup> for 70 wt % at 273 K in our present work of uptake of glyoxal, demonstrating that glyoxal is more reactive on aqueous solutions than methylglyoxal. The reaction of smaller  $\alpha$ -dicarbonyls on sulfuric acid solutions is characterized by initial hydration to form diols and tetrols, which subsequently undergo aqueous-phase reactions to form nonvolatile oligomers.<sup>63</sup> The effect of methyl substitution in the  $\alpha$ -dicarbonyls likely inhibits hydration and oligomerization, explaining the more efficient heterogeneous reactions of glyoxal than of



methylglyoxal on sulfuric acid. Also, the amount of available water in the solution governs the equilibrium between the unhydrated and hydrated forms of the  $\alpha$ -dicarbonyls.<sup>63</sup> The hydration and oligomerization reactions are hindered in more acidic sulfuric acid solutions, because the water activity decreases,<sup>94,95</sup> leading to a solubility-limited reversible uptake. Figure 17 depicts the hydration driven oligomerization of glyoxal in sulfuric acid, and the subsequent formation of SOA.

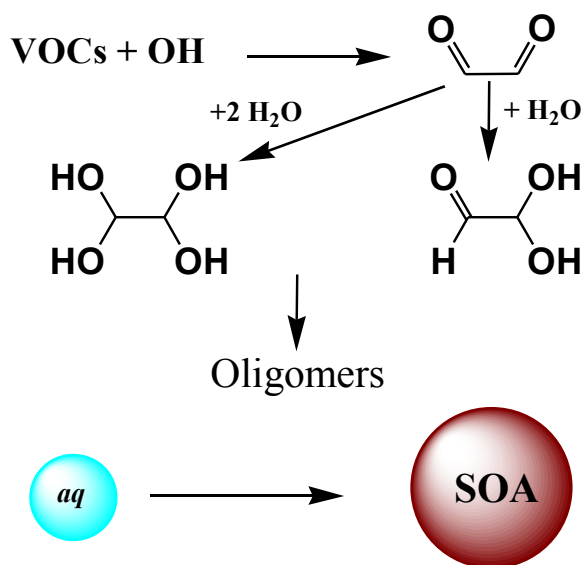


Figure 17. Depiction of the oligomerization of glyoxal and formation of SOA.

## Summary

In this work, we have measured the heterogeneous uptake of glyoxal in 60-93 wt % H<sub>2</sub>SO<sub>4</sub> and the temperature range of 253-273 K, utilizing a fast-flow low-pressure reactor coupled to an ion-drift chemical ionization mass spectrometer. The measured  $\gamma$  value of glyoxal on sulfuric acid is in the range of  $(1.2 \pm 0.06) \times 10^{-2}$  to  $(2.5 \pm 0.01) \times 10^{-3}$  for 60 - 93 wt % H<sub>2</sub>SO<sub>4</sub> and temperatures of 253-273 K. The measured  $H^*$  value is in the range from  $(98.9 \pm 4.9) \times 10^5 \text{ M atm}^{-1}$  to  $(1.6 \pm 0.1) \times 10^5 \text{ M atm}^{-1}$  for 60 - 93 wt % and the temperatures of 263-273 K. Both the uptake coefficient and Henry's Law constant increase with decreasing acid concentration and temperature. Our results show that glyoxal is more reactive than methylglyoxal on aqueous solutions and the heterogeneous reaction mechanism of smaller  $\alpha$ -dicarbonyls involves hydration followed by oligomer formation, indicating that the oligomerization of glyoxal leading to secondary organic aerosol formation is largely dependent on the particle hygroscopicity.

Our measured dependence of the  $\gamma$  and  $H^*$  values with the acidity indicates that the reactions of hydration and oligomerization for smaller  $\alpha$ -dicarbonyls are unlikely to be acid-catalyzed, in contrast to those from the previous studies.<sup>80,89</sup> For example, the  $H^*$  value of glyoxal has been found to be enhanced by less than 3 times in the presence of chloride in the range of 0.05–4.0 M ionic strength and by 50 times in the presence of sulfate at 0.03 M ionic strength.<sup>80</sup> Also, on one hand, Schweitzer et al. has explained an increased uptake of glyoxal in acidic solutions as a result of protonation prior to accommodation.<sup>84</sup> On the other hand, a previous chamber study of SOA growth by

reactive uptake of simple carbonyl compounds has shown little enhancement in particle growth with an acidic seed, suggesting that the glyoxal uptake is not a result of particle acidity but rather of ionic strength of the seed.<sup>96</sup>

For 60 wt % sulfuric acid at 273 K, our measured  $\gamma$  and  $H^*$  values are  $7.9 \times 10^{-3}$  and  $20.4 \times 10^5 \text{ M atm}^{-1}$ , respectively. Extrapolation of our measurements to a neutral solution at 273 K yields the  $\gamma$  and  $H^*$  values of  $1.7 \times 10^{-2}$  and  $8.7 \times 10^7 \text{ M atm}^{-1}$ , respectively. Our extrapolated  $H^*$  to the neutral solution at 273 K appears to be higher than that previously measured value ( $1.6 \times 10^6 \text{ M atm}^{-1}$ ) for glyoxal in water at neutral pH and at 278 K.<sup>80</sup> However, extrapolation of our measurements to a neutral solution involves a rather large concentration range, because the most diluted sulfuric acid employed in our experiments is 60 wt %. Interestingly, on the basis of the model-measurement differences, it has been suggested that the  $\gamma$  value of about  $3.7 \times 10^{-3}$  for irreversible uptake to aerosol surface area or a  $H^*$  value of  $4 \times 10^9 \text{ M atm}^{-1}$  for reversible partitioning to aerosol liquid water would be necessary to explain the missing sink for gas-phase glyoxal in Mexico city.<sup>79</sup> Clearly, our measurements support an efficient heterogeneous reaction of glyoxal on aqueous aerosols. Future laboratory measurements are needed for the heterogeneous chemistry at more relevant tropospheric conditions in urban environments, to evaluate their contributions to SOA formation and the impacts on aerosol cloud-forming and optical properties.<sup>97</sup>

CHAPTER IV  
HYGROSCOPICITY, DELIQUESCENCE, AND CLOUD CONDENSATION  
NUCLEI ACTIVITY OF ALKYLAMINIUM  
CARBOXYLATE AEROSOLS

**Introduction**

Atmospheric aerosols affect air quality, visibility, human health, and the Earth radiation balance.<sup>18</sup> In particular, aerosols impact the Earth energy budget in two distinct ways, directly by absorbing and scattering solar radiation and indirectly by acting as cloud condensation nuclei (CCN) that change the lifetime, coverage, precipitation efficiency, and albedo of clouds.<sup>18-20,98</sup> Currently, the direct and indirect radiative forcings by aerosols represent the largest uncertainty in climate projections.<sup>18</sup> The complex effects of aerosols in the atmosphere partially depend on particle size, number concentration, and chemical composition. Atmospheric aerosols are broadly categorized to be primary and secondary on the basis of their formation mechanisms.<sup>14,24</sup> In particular, secondary organic aerosols (SOA) represent one of the key chemical constituents under diverse environmental conditions. Photochemical oxidation of biogenic and anthropogenic hydrocarbons leads to formation of semi- and low-volatile products,<sup>46,50,99-101</sup> some of which may contribute to nucleation and growth of SOA. Several mechanisms have been proposed to account for SOA growth, including condensation of non-volatile or extremely low-volatile organic species, gas/particle partitioning of semi-volatile organic species, and heterogeneous reactions of volatile or

semi-volatile compounds.<sup>14,23,63,102-105</sup> Among the heterogeneous reactions leading to SOA growth is the acid-base reactions between organic acids and amines.<sup>10,14,106</sup>

Monocarboxylic and dicarboxylic organic acids are directly emitted into the atmosphere from biogenic and anthropogenic sources or are formed in the atmosphere as the products of photochemical and multi-phase reactions.<sup>107-113</sup> Carboxylic acids have been identified under diverse environmental conditions, including semi-urban sites in the northeastern US,<sup>114</sup> urban environments,<sup>115-118</sup> and remote locations.<sup>119</sup> Organic acids have been shown to contribute importantly to particle nucleation and growth.<sup>8,9,120</sup> Short aliphatic alkylamines are derivatives of ammonia, where one or more hydrogen atoms are replaced by an alkyl functional group. Alkylamines are emitted by anthropogenic and biogenic sources, and represent a significant portion of the organic nitrogen species present in the atmosphere.<sup>121</sup> The total global emissions of monomethylamine (MMA), dimethylamine (DMA), and trimethylamine (TMA) have been estimated at  $\sim 285 \pm 78$  Gg N a<sup>-1</sup>, significantly lower than the total global emissions of ammonia.<sup>121</sup> Alkylamines are highly volatile and do not undergo condensation under ambient conditions. The reaction pathways for alkylamines include gaseous oxidation reactions by OH, O<sub>3</sub>, and NO<sub>3</sub> and heterogeneous reactions, which have been shown in field measurements, modeling studies, and laboratory experiments.<sup>7,122-127</sup> In particular, due to the substitution of one or more hydrogen atoms by an alkyl functional group, alkylamines have a stronger basicity than ammonia and engage efficiently in acid-base or replacement reactions in the condensed phase.<sup>24,61,128,129</sup>

Quantum chemical calculations have shown that alkylamines bind to organic acids with a large binding energy and hydration promotes proton transfer from organic acids to alkylamines, consequently increasing the interaction strength.<sup>120,130</sup> An experimental study showed that new particle formation is enhanced in the presence of methanesulfonic acid, amines, and water.<sup>131</sup> *Smith et al.* conducted field measurements of aminium salts in Mexico, Finland, and the United States using Thermal Desorption Chemical Ionization Mass Spectrometry (TDCIMS) and Ultrafine Hygroscopicity Tandem Differential Mobility Analyzer (UHTDMA), showing that aminium salts are commonly found in ultrafine particles.<sup>132</sup> On the basis of equilibrium partitioning of organic acids, bases, and their salts, amines have been suggested to be important contributors to organic salt formation, likely explaining field and laboratory observations of the coexistence and accumulation of low-molecular weight organic acids and bases in nucleation mode particles; by reacting with organic and inorganic acids in newly formed particles, alkylamines form organic salts that yield nonvolatile ion pairs.<sup>133</sup> Reactions between alkylamines and ammonium salts have also been shown to occur efficiently in laboratory experiments.<sup>23,134-136</sup> Displacement reactions between alkylamines and ammonium sulfate or ammonium nitrate have been observed and found to proceed even in the presence of an excess amount of gaseous ammonia.<sup>23,134,135</sup> The uptake coefficients of alkylamines on ammonium nitrate and sulfate have been reported to be on the order of  $\sim 10^{-2}$  to  $10^{-3}$ , whereas the reaction between alkylamines and ammonium bisulfate has been shown to be diffusion-limited.<sup>23,134</sup> Previous kinetic measurements suggest that under atmospheric conditions alkylamines initially form a layer of

alkylammonium salts on the ammonium salt aerosol surface and its thickness increases over time.<sup>23</sup> The kinetics of the acid–base reactions between methylamine, dimethylamine, and trimethylamine on citric acid and humic acid has been investigated using a Knudsen cell reactor.<sup>137</sup> Citric acid, as a stronger acid, shows a higher reactivity for amines than humic acid, and the steric effect of amines due to methyl-substitution regulates their reactivity with organic acids.

Recent measurements of the volatility of alkylammonium carboxylate salts shows high thermal stability from the organic acid–amine reactions, with a measured vapor pressure of alkylammonium dicarboxylate salts of  $\sim 10^{-6}$  Pa.<sup>51</sup> The latter experimental results also indicate that alkylammonium monocarboxylates act as protic ionic liquids at room temperature. *Dinar et al.* have shown that the reactive uptake of ammonia on slightly soluble organic acid particles increases their CCN activity and hygroscopic growth.<sup>138</sup> *Prenni et al.* have measured the water uptake of pure dicarboxylic acid aerosols<sup>113</sup> and internally mixed particles containing ammonium sulfate and a dicarboxylic acid.<sup>139</sup> Their measurements show that the hygroscopicity of the dicarboxylic acid particles increases when the organic acid is mixed with ammonium sulfate. For instance, the hygroscopic growth factor (HGF) of pure oxalic acid particles is 1.45 at 90% RH, whereas for ammonium sulfate:oxalic acid particles the HGF is 1.70 at 90% RH. In addition, the results by *Prenni et al.*<sup>113</sup> indicate that pure adipic acid particles do not absorb water, but once mixed with ammonium sulfate the HGF increases to 1.35 at 90% RH. *Cruz and Pandis* measured the deliquescence and hygroscopicity of glutaric and pinonic acid aerosols mixed with sodium chloride and ammonium sulfate,

indicating little effect on deliquescence but enhanced water uptake by the organic portion.<sup>140</sup> Recently, *Suda et al.* investigated the influence of functional groups on the CCN activity of organic aerosols, showing that the hydroxyl group exerts the largest impact on CCN activity among several functional groups.<sup>141</sup>

In this study we measured the HGF and CCN activity for a series of atmospherically relevant aminium carboxylate aerosols. We also determined the hygroscopicity parameter ( $\kappa$  or Kappa) utilizing three methods: from the measured HGF results, from the measured CCN results, and theoretically calculated.<sup>142</sup> The dependence of the hygroscopic and deliquescent characteristics of alkylaminium carboxylate aerosols on molecular functionality, molecular weight, and acidity has been demonstrated, and relevant atmospheric implications are discussed.

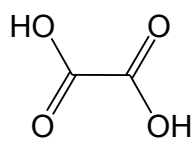
## Experimental

### *Reagents*

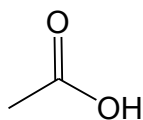
Aqueous solutions of MMA (40%), DMA (40%), and TMA (45%) were purchased from Sigma and used as received. Propanoic acid (PrA, 99%), p-toluic acid (pTA, >99%), cis-pinonic acid (cPA, >99%), oxalic acid (OxA, >99%), succinic acid (SuA, >99%), malic acid (MaA, >99%), adipic acid (AdA, 99%), and azelaic acid (AzA, >99%) were purchased from Sigma and used as received. Aqueous acetic acid (AcA, 40%) was purchased from Fisher and used as received. Figure 18 in the supplemental information shows the molecular structures of all organic acids and alkylamine bases utilized in this study.



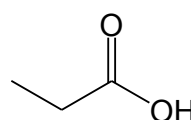
## ORGANIC ACIDS



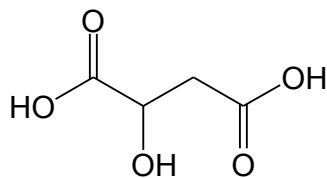
Oxalic Acid  
(OxA)



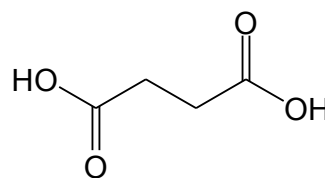
Acetic Acid  
(AcA)



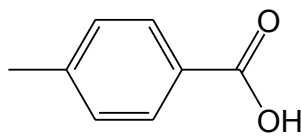
Propanoic Acid  
(PrA)



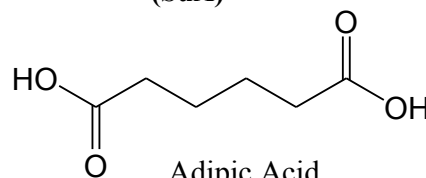
Malic Acid  
(MaA)



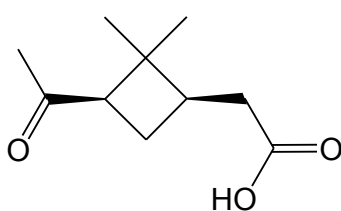
Succinic Acid  
(SuA)



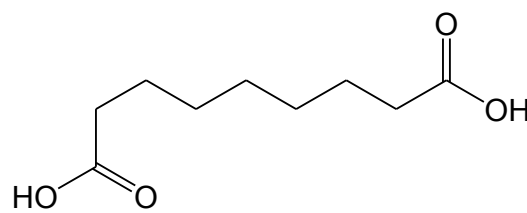
p-Toluic Acid  
(pTA)



Adipic Acid  
(AdA)

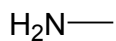


cis-Pinonic Acid  
(cPA)

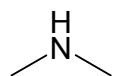


Azelaic Acid  
(AzA)

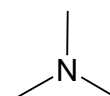
## ALKYLAMINE BASES



Methylamine  
(MMA)



Dimethylamine  
(DMA)



Trimethylamine  
(TMA)

Figure 18. Molecular structures of organic acids and alkylamine bases relevant to the alkylaminium carboxylate salts in this study.

Table 5 summarizes the solubility and density for the organic acids utilized in this study, highlighting the differences in solubility between each acid, where solubility ranges from 0.5 g/100 g in water to miscible compounds (i.e., acetic and propanoic acid).

**Table 5. Solubility and density of the weak organic acids utilized for HGF and CCN measurements.**

	Solubility (g/100 g water)	Crystal Density (g cm <sup>-3</sup> )
<b>Oxalic</b>	12	1.9
<b>Succinic</b>	8.8	1.552
<b>Malic</b>	126.3	1.61
<b>Adipic</b>	2.49	1.362
<b>Azelaic</b>	0.5	1.251
<b>Acetic</b>	miscible	1.05
<b>Propanoic</b>	miscible	0.99
<b>p-Toluic Acid</b>	Sparingly soluble	1.06
<b>cis-Pinonic</b>	0.64-0.71	0.781

#### *Aminium Carboxylate Sample Preparation*

Aqueous solutions (1 wt %) of aminium carboxylate salts were prepared in the laboratory by dissolving the relevant reagents in 300 mL of 18.2 MΩ Millipore water and used immediately. Typically, one molar equivalent of a monocarboxylic acid was mixed with one molar equivalent of the amine base and stirred vigorously in water at room temperature. For dicarboxylic acids, one molar equivalent of the acid was mixed with two molar equivalents of the amine base. The analyte solutions were prepared at stoichiometrically neutral conditions, i.e., (1:1) for monocarboxylic acids and (1:2) for

dicarboxylic acids. The acid to base ratio was increased to (4:1) for additional experiments with an increasing acid content.

### *Hygroscopic Growth Factor Measurements*

For Hygroscopicity Tandem Differential Mobility Analyzer (HTDMA) experiments, aerosols were generated with a continuous flow aerosol particle generator (TSI 3076) by atomizing the aminium carboxylate solutions. The aerosol flow was diluted with dry nitrogen gas at a 4:1 ratio. The generated poly-dispersed aerosols were heated to 343 K to reduce humidity in the aerosol flow (without thermal decomposition), and then dried using two Nafion tube bundles (PD-070–18T-12SS, Perma Pure). The particles were then neutralized using a  $^{210}\text{Po}$  radioactive source. Hygroscopic growth factors were measured using a HTDMA coupled to a condensation particle counter (CPC, TSI 3762). Size-selected aerosols with the dry diameters of 46, 81, 97, 100, and 151 nm were exposed to increasing RH in the range 10% to 90% with an approximate step of 10%. HGF is defined as the ratio of  $D_{p,\text{RH}}$  to  $D_{p,0}$ , where  $D_{p,\text{RH}}$  is the particle size separated by the second DMA<sub>2</sub> at an elevated RH and  $D_{p,0}$  is the particle size separated by the first DMA<sub>1</sub> at RH ~10% (the dry condition). The RH was actively controlled to within 2% and measured at the inlet and outlet of DMA<sub>2</sub>. Measurements were repeated at least 3 times, and the average value and standard deviation were calculated for each particle diameter and RH. 3

### *Cloud Condensation Nuclei Measurements*

CCN activation measurements were made with a continuous flow, streamwise thermal gradient DMT-CCN (Droplet Measurement Technology CCN-100) counter connected to the outlet of DMA1 of the HTDMA assembly in parallel with the CPC. Particles were generated and dried as described above. The voltage applied to DMA<sub>1</sub> was scanned and the concentration of size-classified particles was measured with the CPC and CCN counter to determine the CN and CCN spectra, respectively. The sheath-to-aerosol flow ratios in both the DMA and CCN counter were set to 10:1, and all measurements were conducted at 298 K. Nominal supersaturation ( $S$ ) values in the CCN counter were set at 0.19%, 0.37%, and 0.51%, and the corresponding activation curves were obtained at each supersaturation. The CCN counter was calibrated using ammonium sulfate particles. From the CCN and CN spectra, the CCN/CN ratio curves were obtained by taking into account doubly charged particles, if applicable. CCN activation efficiency curves were calculated, and the  $Dp_{50}$  (defined as the aerosol diameter at which 50% of the particles activated at a given supersaturation) was determined and used to calculate the hygroscopicity parameter ( $\kappa$ ).

The  $\kappa$  value was calculated using three methods: from the HGF measurements, from the CCN measurements, and from the theoretical calculation. The expressions used are summarized below, following *Petters and Kreidenweis*.<sup>142</sup> For the HGF results, the  $\kappa$  value is obtained as,

$$\kappa = \left[ \frac{1}{RH} \exp\left(\frac{A}{D}\right) - 1 \right] (HG_f^3 - 1) \quad (4.1)$$

where  $D$  is the wet particle diameter and  $A$  is 2.09 nm for water, which is calculated assuming a surface tension ( $\sigma$ ) of 72 dyne  $\text{cm}^{-1}$  at 298 K using the following expression,

$$A = \frac{4\sigma M_w}{RT\rho_w} \quad (4.2)$$

where  $M_w$  is the molecular weight of water and  $\rho_w$  is the density of water at 298 K.

The  $\kappa$  value is determined from the CCN results on the basis of the  $D_{p50}$  determined from each measurement,

$$\kappa = \frac{4A^3}{27D_{p50}^3 \ln^2 S_c} \quad (4.3)$$

where  $S_c$  is the critical supersaturation, which is obtained from the  $S$  maintained in the CCN counter.

For comparison with the values derived from the experimental data, the  $\kappa$  value is theoretically calculated by taking into account the molecular composition of the particles. Using the density and molecular weight (MW) of the components, the individual  $\kappa_i$  value for each is determined, and the  $\kappa$  value of the mixture is obtained from the linear combination of the single component values (i.e., the mixing rule),

$$\kappa_i = \frac{v_i \rho_d MW_w}{\rho_w MW_i} \quad (4.4)$$

$$\kappa = \sum_i \varepsilon_i \kappa_i \quad (4.5)$$

where  $MW_w$  is the molecular weight of water,  $\rho_d$  is the dry particle density,  $\rho_w$  is the density of water, and  $MW_i$ ,  $v_i$ , and  $\varepsilon_i$  are the molecular weight, van't Hoff factor, and volume fraction of the  $i$ th component, respectively. Equation 4 is directly used to

calculate the  $\kappa$  value for a single component species. The uncertainty in our measured HGF was typically within 10%, which resulted in a systematic error of less than 34% in HGF-derived  $\kappa$  using equation (1). Considering the possible errors associated with the CCN  $Sc$  (10%) and DMA sizing (10%), a systematic error of less than 53% was estimated for the CCN-derived  $\kappa$  using equation (3).

## Results and Discussion

### *Hygroscopic Growth Factor*

The HGF values for the aminium carboxylates of mono- and di-carboxylic acids were measured between 10% and 90% RH under stoichiometrically neutral conditions. Figures 19 (a)-(f) depicts the HGF results for aminium mono and di-carboxylates.

For the methylaminium monocarboxylates (i.e., the methylaminium salts of acetic acid, propanoic acid, p-toluic acid, and cis-pinonic acid) in Figure 19(a), AcA:MMA exhibits the highest HGF of 1.57 at 90% RH, followed by PrA:MMA and pTA:MMA that have the HGF values of 1.52 and 1.45, respectively. cPA:MMA has the lowest HGF of 1.32 at 90% RH. It is also apparent from Figure 19(a) that the methylaminium monocarboxylates do not exhibit a clear deliquescence point, since the particles show a gradual growth with increasing RH. Interestingly, pTA:MMA shows an initial decrease in particle size as the RH is increased to about 60% (possibly due to a variation in the particle morphology) and subsequent growth for RH larger than 60%, but cPA:MMA shows a gradual growth at RH higher than 50%.

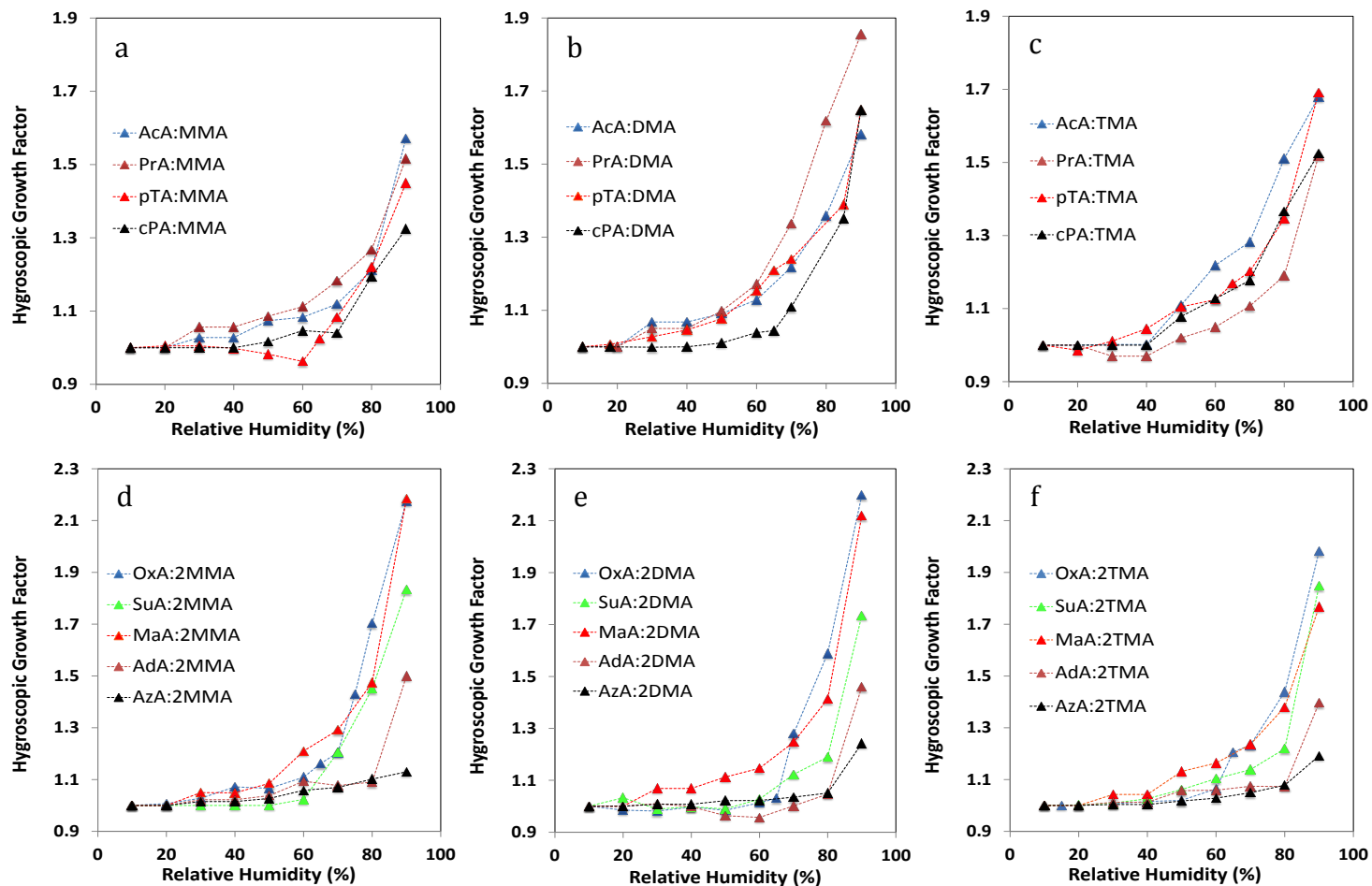


Figure 19. Hygroscopic growth factor (HGF) for alkylammonium carboxylate salts. In the RH range of 10% to 90% and the particle size range of 46 to 151 nm: (a)-(c) Mono, di, tri-methylammonium salts of acetic acid (AcA, blue triangle), propanoic acid (PrP, maroon triangle), p-toluic acid (pTA, red triangle), and cis-pinonic acid (cPA, black triangle); (d)-(f) Mono, di, tri-methylammonium salts of oxalic acid (OxA, blue triangle), succinic acid (SuA, green triangle), malic acid (MaA, red triangle), adipic acid (AdA, maroon triangle), and azelaic acid (AzA, black triangle).

As shown in Figure 19(b), the HGF values at 90% RH are 1.58, 1.64, 1.65, and 1.85 for the dimethylammonium salts of acetic acid, cis-pinonic acid, p-toluic acid, and propanoic acid, respectively. As with the methylammonium monocarboxylates, the dimethylammonium salts do not show a clear deliquescence point; the particles show a steady growth starting at about 30% RH, except for cPA:DMA, which does not grow until 50% RH. For the trimethylammonium salts of acetic acid, propanoic acid, p-toluic acid, and cis-pinonic acid in Figure 19(c), the HGF at 90% RH is 1.52, 1.52, 1.68, and 1.69 for PrA:TMA, cPA:TMA, AcA:TMA, and pTA:TMA, respectively. A steady growth is observed for pTA:TMA above 30% RH and for AcA:TMA and cPA:TMA above 40% RH. PrA:TMA exhibits a slight decrease in diameter at 30% and 40% RH (also possibly due to the particle morphology) but exhibits growth at RH above 50%.

The HGF characteristics for alkylammonium dicarboxylates under stoichiometrically neutral conditions for MMA, DMA, and TMA are shown in Figures 19(d)-(f). For the methylammonium di-acid (i.e., oxalic acid, succinic acid, malic acid, adipic and azelaic acid) OxA:2MMA and MaA:2MMA have the highest HGF of 2.18 at 90% RH, followed by SuA:2MMA with a HGF of 1.83 and AdA:2MMA with a HGF of 1.50. The lowest HGF of 1.13 is found for AzA:2MMA. It is apparent from Figure 19(d) that for the monomethylammonium salts only SuA:2MMA exhibits an apparent deliquescence point at 60% RH. For the dimethylammonium salts of oxalic acid, succinic acid, malic acid, adipic and azelaic acid in Figure 19(e), deliquescence is evident at about 60%, 80%, and 80% RH for OxA:2DMA, AdA:2DMA, and AzA:2DMA, respectively. Only MaA:2DMA shows gradual growth without a deliquescence point.



For the five dimethylamminium di-acid salts, the HGF at 90% RH is 2.19 for OxA:2DMA, 2.11 for MaA:2DMA, 1.73 for SuA:2DMA, 1.46 for AdA:2DMA, and 1.24 for AzA:2DMA. For the trimethylamminium salts of oxalic acid, succinic acid, and malic acid in Figure 19(f), steady growth is observed starting at 30% RH, except for AdA:2TMA and AzA:2TMA, which exhibit growth above 50% and 60% RH, respectively. The HGF at 90% RH is 1.98 for OxA:2TMA, 1.85 for SuA:2TMA, 1.77 for MaA:2TMA, 1.40 for AdA:2TMA, and 1.19 for AzA:2TMA.

The measurements show decreasing HGF values at 90% RH with increasing MW for di-carboxylic acids (i.e., oxalic acid, succinic acid, adipic acid, and azelaic acid) and independent of the amine base, except for malic acid. In contrast, such a HGF trend is less evident for the aminium mono-carboxylate salts. For aminium mono-carboxylates, the HGF at 90% RH increases with decreasing MW for MMA, but not consistently for DMA and TMA (e.g., AcA:DMA, cPA:DMA, PrA:TMA, and pTA:TMA). For comparison, the water solubility of pure mono- and di-carboxylic acids consistently decreases with increasing molar weight, also except for malic acid (Table 5).

Aminium di-carboxylates show similar HGF at 90% RH for the same acids but different amine types, while the HGF value at 90% RH is somewhat different for aminium mono-carboxylates of the same organic acids but different amine types. For example, the HGF values are higher for the aminium mono-carboxylates with DMA and TMA than those with MMA. Several aminium di-carboxylates (SuA:2MMA, OxA:2DMA, AdA:2DMA, and AzA:2DMA) exhibit deliquescence, but not for the aminium mono-carboxylates.

**Table 6. Molecular weight (MW), HGF at 90% RH, and  $\kappa$  values derived using three methods i.e., the mixing rule (MR) approximation, HGF results, and CCN results for aminium carboxylates. The  $\kappa$  value from the HGF results is derived at 90% RH, and the  $\kappa$  value from the CCN results is averaged at supersaturation ranging from 0.19 to 0.51%.**

Methylaminium Salts	MW	HGF	$\kappa$ (MR)	$\kappa$ (HGF)	$\kappa$ (CCN)
Acetic	91.11	1.57 ± 0.17	0.53	0.41 ± 0.04	0.19 ± 0.05
Propanoic	105.14	1.52 ± 0.11	0.45	0.53 ± 0.035	0.08 ± 0.02
p-Toluic	167.20	1.45 ± 0.12	0.31	0.34 ± 0.03	0.09 ± 0.004
cis-Pinonic	215.29	1.32 ± 0.16	0.28	0.24 ± 0.03	0.13 ± 0.005
Oxalic	152.15	2.18 ± 0.05	0.66	1.37 ± 0.03	0.46 ± .27
Succinic	180.20	1.83 ± 0.11	0.55	0.73 ± 0.04	0.16 ± 0.02
Malic	196.21	2.18 ± 0.13	0.52	1.26 ± 0.08	0.49 ± .30
Adipic	208.26	1.50 ± 0.15	0.46	0.40 ± 0.04	0.14 ± 0.01
Azelaic	250.34	1.13 ± 0.03	0.33	0.06 ± 0.002	0.11 ± 0.02
Dimethylaminium Salts	MW	HGF	$\kappa$ (MR)	$\kappa$ (HGF)	$\kappa$ (CCN)
Acetic	105.13	1.58 ± 0.15	0.43	0.59 ± 0.05	0.14 ± 0.05
Propanoic	119.16	1.85 ± 0.11	0.38	0.72 ± 0.04	0.11 ± 0.02
p-Toluic	181.22	1.65 ± 0.12	0.28	0.50 ± 0.03	0.05 ± 0.03
cis-Pinonic	229.31	1.64 ± 0.24	0.25	0.52 ± 0.07	0.09 ± 0.02
Oxalic	180.19	2.19 ± 0.05	0.49	1.32 ± 0.03	0.19 ± 0.02
Succinic	208.24	1.73 ± 0.12	0.43	0.60 ± 0.042	0.14 ± 0.02
Malic	224.25	2.11 ± 0.12	0.41	1.19 ± 0.06	0.11 ± 0.09
Adipic	236.30	1.46 ± 0.11	0.37	0.28 ± 0.02	0.18 ± 0.02
Azelaic	278.38	1.24 ± 0.04	0.28	0.12 ± 0.004	0.11 ± 0.02
Trimethylaminium Salts	MW of Salt	HGF	$\kappa$ (MR)	$\kappa$ (HGF)	$\kappa$ (HGF)
Acetic	119.16	1.68 ± 0.18	0.37	0.70 ± 0.075	0.15 ± 0.04
Propanoic	133.19	1.52 ± 0.16	0.33	0.47 ± 0.049	0.15 ± 0.02
p-Toluic	195.25	1.69 ± 0.12	0.25	0.55 ± 0.04	0.06 ± 0.03
cis-Pinonic	243.34	1.52 ± 0.08	0.22	0.36 ± 0.018	0.05 ± 0.02
Oxalic	208.15	1.98 ± 0.11	0.40	0.94 ± 0.05	0.23 ± 0.07
Succinic	236.30	1.85 ± 0.22	0.36	0.74 ± 0.07	0.17 ± 0.01
Malic	252.31	1.77 ± 0.09	0.35	0.65 ± 0.03	0.19 ± 0.07
Adipic	264.36	1.40 ± 0.08	0.32	0.24 ± 0.014	0.19 ± 0.03
Azelaic	306.44	1.19 ± 0.05	0.25	0.10 ± 0.004	0.12 ± 0.02

Each point represents the average of three experiments, and the uncertainty reflects the random error of the measurements ( $1\sigma$ ).

Table 6 summarizes our measured HGF for all aminium carboxylate salts. Each data point represents the average of the HGF for particles with selected diameters between 46 to 151 nm. Typically, there is a slight increase in the measured HGF values with increasing particle size, and the difference in the measured HGF is within 10% in our selected size range.

#### *Cloud Condensation Nuclei Activity*

Figures 20(a)-(b) depict the activation diameters ( $Dp_{50}$ ) for alkylaminium salts of selected mono- and di-carboxylic acids measured at three different  $S$  values of 0.19, 0.37, and 0.51%. For the alkylaminium salts of acetic acid, the  $Dp_{50}$  values range from 144 to 61 nm for MMA, 125 to 74 nm for DMA, and 150 to 65 for TMA. For the alkylaminium salts of cis-pinonic acid the  $Dp_{50}$  value range is 146 to 73 nm for MMA, 159 to 78 nm for DMA, and 196 to 113 nm for TMA. For the alkylaminium salts of oxalic acid, the  $Dp_{50}$  values range from 79 to 59 nm for MMA, 131 to 63 nm for DMA, and 108 to 69 nm for TMA, and for the alkylaminium salts of azelaic acid  $Dp_{50}$  values range from 152 to 81 nm for MMA salts, 143 to 79 nm for DMA salts, and 143 to 74 nm for TMA salts. For the alkylaminium carboxylates shown in Figure 20, the measured  $Dp_{50}$  value increases with decreasing supersaturation and increasing MW of the organic acids.

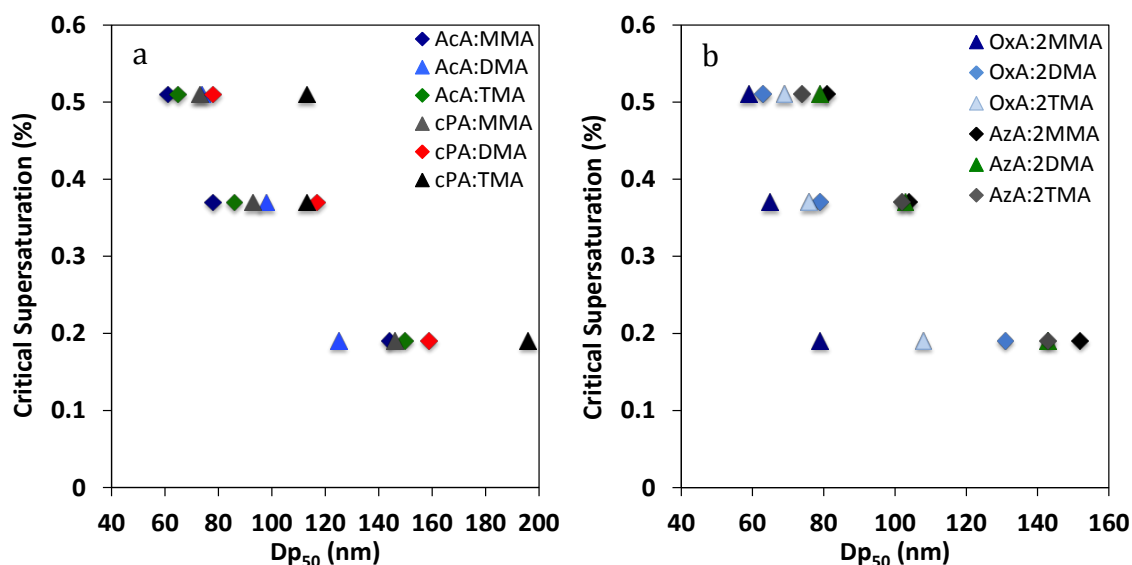


Figure 20. Activation diameters ( $Dp_{50}$ ) of alkylaminium carboxylates. CCN measured at  $S = 0.19$ ,  $0.37$ , and  $0.51\%$ : (a) for alkylaminium monocarboxylates with acetic and cis-pinonic acids (navy blue diamonds AcA:MMA, royal blue triangles for AcA:DMA, green diamonds for AcA:TMA, grey triangles for cPA:MMA, red diamonds for cPA:DMA, and black triangles for cPA:TMA); (b) for alkylaminium dicarboxylates with oxalic and azelaic acids (navy blue triangles for OxA:MMA, blue diamonds for OxA:DMA, light blue for OxA:TMA, black diamonds AzA:MMA, green triangles for AzA:DMA, and grey diamonds for AzA:TMA).

### Hygroscopicity Parameter ( $\kappa$ )

We have derived the  $\kappa$  values for all alkylaminium carboxylates utilizing three methods: i) calculated using the mixing rule approximation, ii) derived from the HGF results at 90% RH, and iii) derived from the CCN results obtained at supersaturation ranging from 0.19 to 0.51%. Figures 21(a)-(f) depict the derived  $\kappa$  values for aminium mono- and di-carboxylates using the three methods. The derived  $\kappa$  using the mixing rule for the aminium carboxylates decreases with increasing molecular weight, i.e., the calculated  $\kappa$  decreases from MMA to DMA and from DMA to TMA for the same acid.

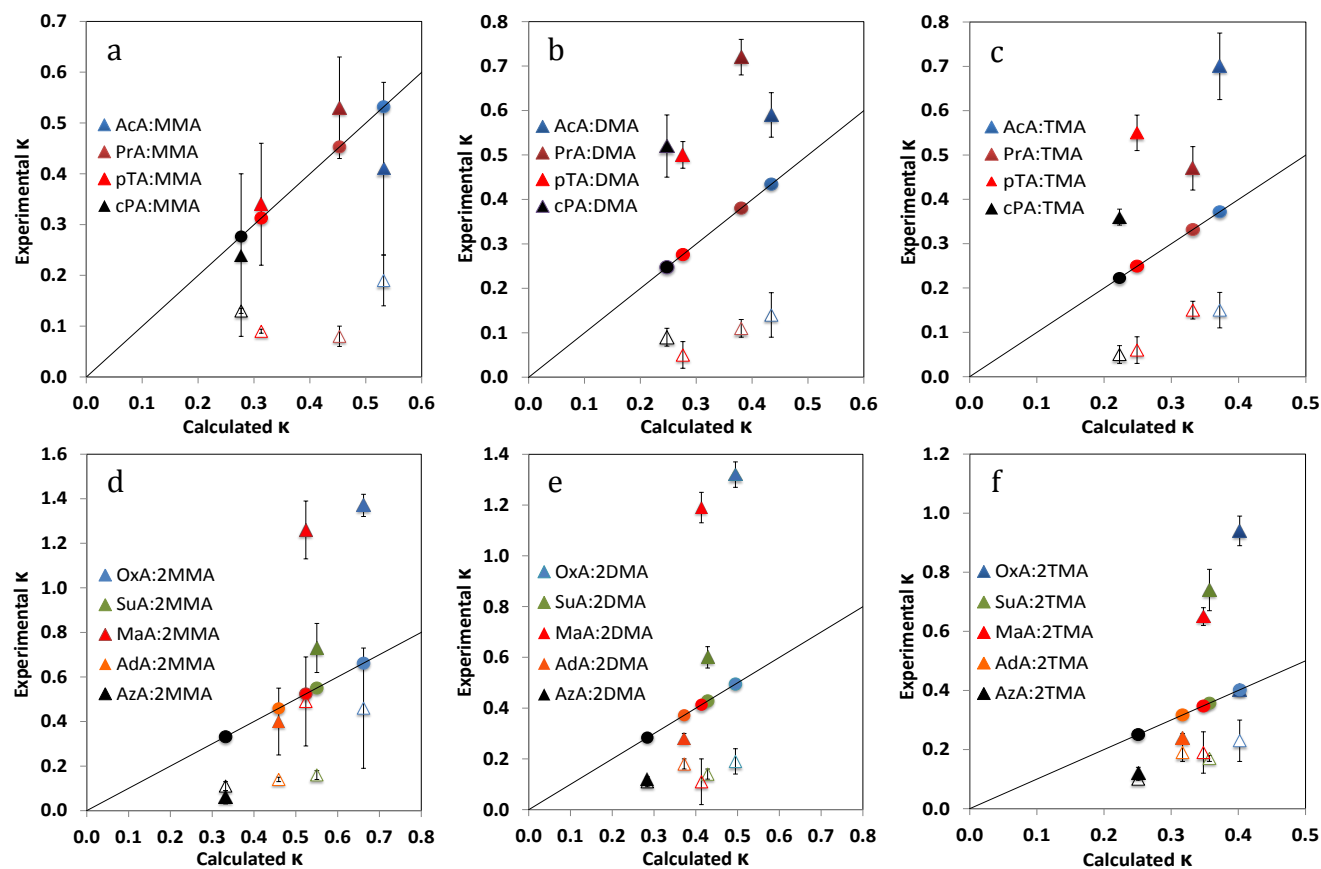


Figure 21. Comparison of the  $\kappa$  values for derived from HGF and CCN results and the mixing rule. (a)-(c) mono, di, and tri-methylaminium monocarboxylates. (d)-(f) mono, di, and tri-methylaminium dicarboxylates. Solid triangles and hollow triangle represent the  $\kappa$  values obtained from HGF and CCN measurements, respectively. The solid circles on the diagonal (1:1) line represent the  $\kappa$  values derived from the mixing rule. In (a)-(c), blue for acetic acid, maroon for propanoic acid, red for p-toluic acid, and black for cis-pinonic acid. In (d)-(f), blue for oxalic acid, green for succinic acid, red for malic acid, orange for adipic acid, and black for azelaic acid. The error bars represent the experimental random error ( $1\sigma$ ).

For example, the calculated  $\kappa$  for acetic acid is 0.53 for MMA, 0.43 for DMA, and 0.37 for TMA. On the other hand, the derived  $\kappa$  using the mixing rule for the aminium carboxylates does not vary monotonically between mono- and di-acids for the same base because of the difference in the acid/base stoichiometry for the neutral species (i.e., the difference in the molecular weight). The calculated  $\kappa$  using the mixing rule is highest for OxA:2MMA (0.66) and lowest for cPA:TMA (0.22). The HGF derived  $\kappa$  is typically higher than that derived from the mixing rule, except for AcA:MMA, cPA:MMA and the two di-acids having the higher molecular weights (adipic and azelaic acid). The CCN derived  $\kappa$  is consistently lower than those derived from the HGF results and the mixing rule. For example, the  $\kappa$  value for OxA:2MMA derived from the CCN measurements is 0.46, which is lower than 1.37 and 0.66 from the HGF and mixing rule methods, respectively.

The dependence of the  $\kappa$  value on the MW for di-acids is similar for both the HGF and CCN methods, i.e., decreasing with increasing molecular weight, except for malic acid with MMA and DMA. For example, the HGF and CCN derived  $\kappa$  values are 1.26 and 0.49 for MaA:2MMA (MW = 196.2), respectively, which are higher than 0.73 and 0.16 for SuA:2MMA (MW = 180.2) and 1.37 and 0.46 for OxA:2MMA (MW = 152.1), respectively. Similarly, the HGF and CCN derived  $\kappa$  values are 1.19 and 0.11 for MaA:2DMA (MW = 224), respectively, which are higher than 0.60 and 0.14 for succinic acid:2DMA (MW = 208) and 1.32 and 0.46 for OxA:2DMA (MW = 180), respectively. The larger hygroscopicity for malic acid is explainable because of the presence of the hydroxyl function, making it more hydrophilic. For comparison, the mixing rule predicts

the  $\kappa$  values of 0.52 for MaA:2MMA, 0.55 for SuA:2MMA, and 0.66 for OxA:2MMA, respectively, increasing with decreasing MW. The HGF and CCN derived  $\kappa$  values are 0.65 and 0.19 for MaA:2TMA (MW = 252.3), respectively, compared to 0.74 and 0.17 for SuA:2TMA (MW = 236.3). Hence, the presence of the OH functional group does not appear to appreciably enhance the hygroscopicity for TMA, likely because increasing methyl substitution induces hydrophobicity. A previous experimental study has shown that the reactivity of amines decreases with increasing numbers of methyl groups on the alkylamine.<sup>23</sup>

#### *Effect of Acidity on Hygroscopicity*

Figure 22 depicts the changes in measured HGF at 90% RH for aminium carboxylate aerosols with a varying acidity, i.e., for the pure acid, an acid to base ratio of 4:1, and the neutral salt. The HGF increases significantly with decreasing acidity, with the values of 1.25 for 4cPA:DMA and 1.65 for cPA:DMA. For comparison, *Cruz and Pandis* have reported an HGF of 1.0 for pure cis-pinonic acid at 90% RH.<sup>140</sup> Similarly, the HGF value also increases from 1.95 for 4OxA:DMA to 2.21 for OxA:2DMA at 90% RH. *Prenni et al.* have reported that pure oxalic acid particles have an approximate HGF of 1.45 at 90% RH.<sup>113</sup> From our measured HGF values and those from the literature, the  $\kappa$  values are 0.11 for pure cPA (ref 142), 0.14 for 4cPA:DMA, and 0.52 for cPA:DMA, increasing with decreasing acidity.

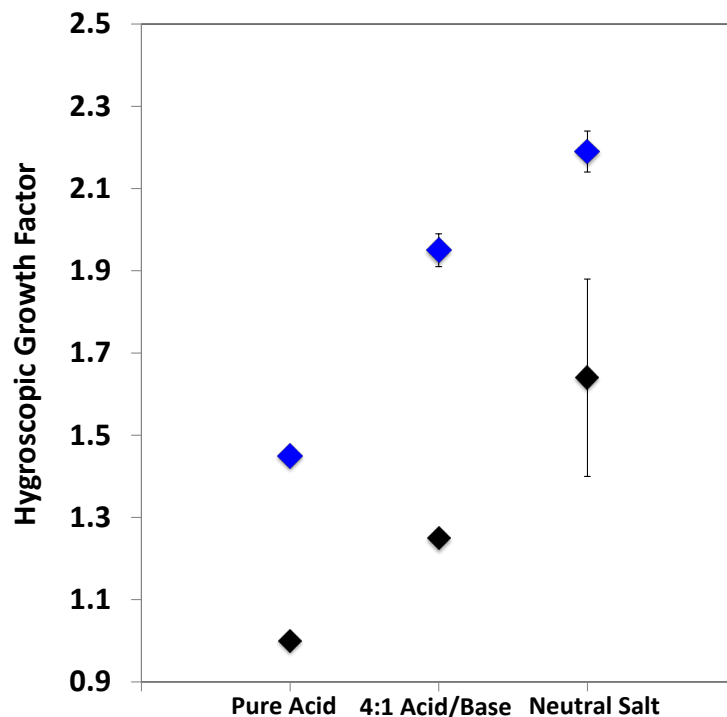


Figure 22. Measured HGF values at 90% RH as a function of acidity. Blue diamonds for pure OxA and its mixtures with DMA under acidic and neutral conditions (i.e., 4OxA:DMA and OxA:2DMA, respectively) and black diamonds for pure cPA and its mixture with DMA under acidic and neutral conditions (i.e., 4cPA:DMA and cPA:DMA, respectively). The HGF values for pure OxA and cPA are taken from refs 113 and 140, respectively. The error bars represent the experimental random error ( $1\sigma$ ).

Similarly, the  $\kappa$  values are 0.5 for pure OxA (ref 143), 0.92 for 4OxA:DMA, and 1.32 for OxA:2DMA. In comparison, the mixing rule predicts the  $\kappa$  values of 0.23 for 4cPA:DMA and 0.25 for cPA:DMA, and 0.69 for 4OxA:DMA and 0.49 for OxA:2DMA, showing no apparent trend with particle acidity as shown in figure 23.



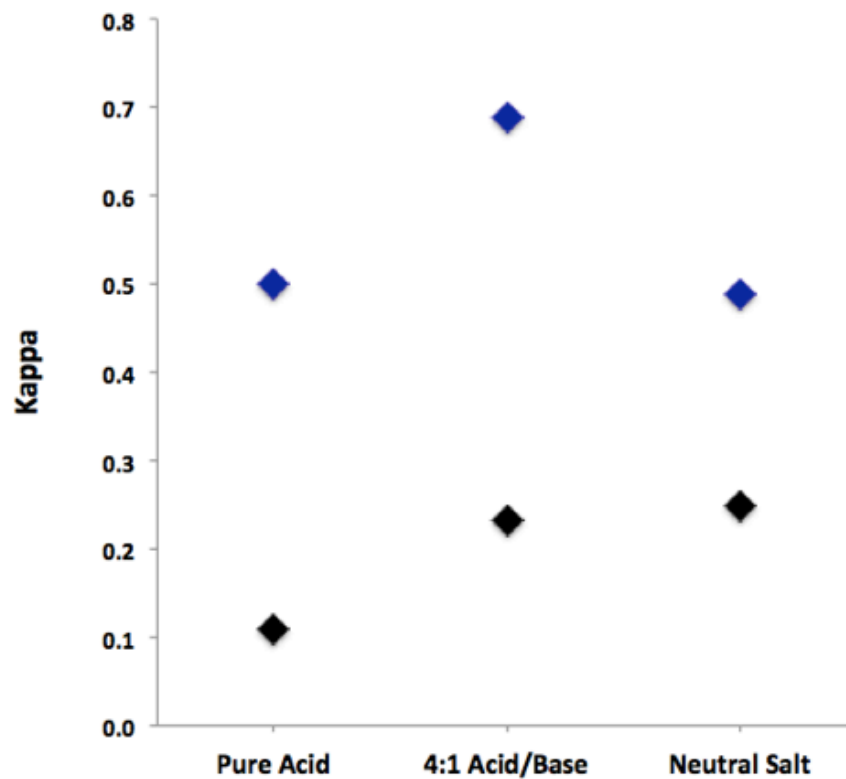


Figure 23. Mixing rule calculated  $\kappa$  values. Blue diamonds for pure OxA and its mixtures with DMA under acidic and neutral conditions (i.e., 4OxA:DMA and OxA:2DMA, respectively) and black diamonds for pure cPA and its mixture with DMA under acidic and neutral conditions (i.e., 4cPA:DMA and cPA:DMA, respectively). The  $\kappa$  values for pure OxA and cPA are obtained from Kumar et al.<sup>143</sup> and Peters and Kreindenweis,<sup>142</sup> respectively.

## Summary

Understanding the hygroscopic and deliquescent characteristics of aerosols is essential for assessing their atmospheric impacts. For example, hygroscopicity is related to the optical (i.e., scattering and absorption) properties of aerosols, which impact not only visibility and air quality but also direct radiative forcing.<sup>144</sup> The CCN activation efficiency of aerosols is relevant to cloud microphysics and precipitation efficiency as well as to the indirect radiative forcing in climate projections, which is highly uncertain.<sup>18-20,98</sup> Hygroscopicity influences the atmospheric lifetime of aerosols, since wet deposition represents one of their key removal processes.<sup>14</sup> Also, heterogeneous reactions leading to secondary aerosol formation may be dependent on hygroscopicity, such as those responsible for SOA and sulfate formation.<sup>14,63,105</sup> In addition, the presence of hygroscopic electrolytes in fine particulate matter may not only influence deposition of particles on biological tissues but also their toxicity, regulating the human health effects.<sup>14</sup> Furthermore, laboratory results of hygroscopicity for various species may assist in interpretation and identification of the chemical constituents for aerosols measured under ambient conditions.<sup>145</sup>

We have investigated the hygroscopic and deliquescent characteristics for a series of alkylammonium carboxylate aerosols, which are selected to represent those commonly found under diverse environmental conditions.<sup>24,110,115</sup> Our results demonstrate that alkylammonium carboxylate aerosols exhibit varied hygroscopicity, dependent not only on MW but also the functionality of the carboxylic acids (i.e., carboxylic or OH functional groups) and the methyl-substitution of the alkylamine bases

(i.e., MMA, DMA, or TMA). For example, aminium monocarboxylate salts exhibit a smaller range (1.3 – 1.8) in HGF at 90% RH than those for aminium dicarboxylate salts (1.1 – 2.2). Dicarboxylate salts, except for the MMA and DMA salts with malic acid, exhibit a correlation between HGF and MW, consistent with mixing rule predictions. However, such a correlation is less evident for monocarboxylate salts. For MaA:2MMA and MaA:2DMA, the measured HGF values are higher than the corresponding values for smaller di-carboxylate salts (i.e., SuA:2MMA and SuS:2DMA), indicating that the OH functional group attached to the aliphatic chain of malic acid enhances hydrophilicity. Our HGF results for MaA:2MMA and MaA:2DMA are consistent with those reported by *Suda et al.*, who have also demonstrated that the hydroxyl group produces the largest enhancement in CCN activity among the different functional groups.<sup>141</sup> However, the enhanced hydrophilicity is less evident for MaA:2TMA, likely because of the steric effect of amines that induces hydrophobicity with increasing methyl substitutions. In addition, our results show that differences in the identity of the alkylamine base correspond to a variation in hygroscopicity for monocarboxylate salts containing the same organic acid, but not for dicarboxylate salts containing the same organic acid.

Our results show that the activation diameters of aminium carboxylates range from 74 to 219 nm at the  $S$  value of 0.19%, suggesting that the aminium carboxylates can readily form cloud droplets under atmospherically relevant conditions. On the other hand, our results illustrate noticeable differences in the hygroscopicity parameter obtained from experimentally measured HGF and CCN results and calculated using the mixing rule. The  $\kappa$  value is in the range of 0.06-1.37 derived from the HGF

measurements, 0.22-0.66 calculated from the mixing rule, and 0.05 – 0.49 derived from the CCN measurements. The  $\kappa$  value obtained from the experimentally measured HGF is typically higher than that from the mixing rule (except for azelaic acid and adipic acid with MMA, DMA, and TMA, and acetic acid and cis-pinonic acid with MMA), and the  $\kappa$  obtained from the mixing rule is consistently higher than that from the CCN results. The  $\kappa$  prediction using the mixing rule is mainly dependent on the density, MW, and van't Hoff factor (i.e., eq. 4). Clearly, the observed  $\kappa$  dependence on molecular functionality (i.e., for MaA:2MMA and MaA:2DMA) from the HGF and CCN measurements is unaccounted for in the mixing rule calculation. The large difference in  $\kappa$  values derived between the measured HGF and CCN results is similar to those previously measured for multi-component organic oligomers.<sup>97</sup> Several explanations have been suggested to account for such discrepancies, including the limitations in the application of the  $\kappa$  approach using the HGF and CCN measurements.<sup>97</sup> For instance, the  $\kappa$  approach applies only for ideal solutions, which may not be appropriate for HGF and CCN measurements. Also, particles consisting of aminium carboxylates may be fractal, and water uptake may lead to additional variation in their morphology. In addition, the calculated  $\kappa$  from the mixing rule assumes that the surface tension of the aerosol solution is identical to that of water and does not vary with the particle size.

Our measurements for aminium carboxylate aerosols with a varying acidity (i.e., from pure organic acid, a 4:1 ratio of acid to base, to a neutral composition) reveal that the HGF and  $\kappa$  value increase significantly with decreasing acidity. In contrast, the  $\kappa$  value predicted from the mixing rule does not account for the acid-base reaction and the

pH dependence of the hygroscopicity. In addition, our measured HGF values of 1.98-2.19 for the three oxalic acid salts (i.e., OxA:2MMA, OxA:2DMA, and OxA:2TMA) at 90% RH are higher than that of 1.70 at 90% RH previously measured for ammonium sulfate:OxA particles,<sup>139</sup> and both are higher than that of 1.45 for pure oxalic acid particles measured by *Prenni et al.*<sup>113</sup>

Our results reveal that several aminium di-carboxylate salts e.g., SuA:2MA, OxA:2DMA, AdA:2DMA, and AzA:2DMA) exhibit an apparent deliquescence point, but not for the aminium mono-carboxylates. Hence, it is likely that these di-carboxylate salts exist in a crystalline phase under dry ambient conditions, while the aminium mono-carboxylate salts only exist in an amorphous state. Also, alkylaminium carboxylate aerosols in the atmosphere may contain impurities (i.e., internally mixed with other aerosol constituents with hygroscopic moieties) that may affect their water uptake and CCN activity. Future laboratory and field measurements are needed to evaluate the hygroscopicity of ambient aminium carboxylates containing impurities and the effects of aminium carboxylates on mixed aerosols.

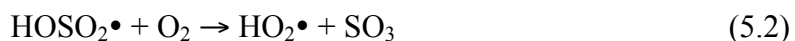
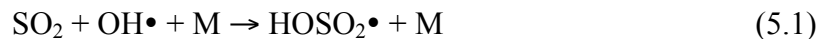
CHAPTER V  
CONVERSION OF SULFUR DIOXIDE TO SULFATE UNDER  
NITROGEN DIOXIDE AND AMMONIA CONDITIONS

**Introduction**

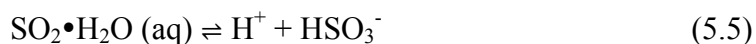
Sulfur dioxide (SO<sub>2</sub>) is a major pollutant in the atmosphere, generated by biogenic and anthropogenic sources. Biogenic sources include volcanic emissions and dimethyl sulfide (DMS) oxidation.<sup>146,147</sup> However, the main emitters are anthropogenic sources such as fossil fuel burning, industry, transoceanic shipping, and power plants.<sup>148</sup> For example, in the year 2010, the global anthropogenic emissions of sulfur dioxide were estimated at 49-55 Tg(S) yr<sup>-1</sup> with the energy and industrial sectors representing the largest contributors.<sup>149</sup> For biogenic emissions, DMS oxidation accounted for 10-40 Tg(S) yr<sup>-1</sup> and volcanic emissions contributed 4-20 Tg (S) yr<sup>-1</sup>.<sup>60</sup>

As a major atmospheric pollutant, sulfur dioxide has detrimental impacts on the ecosystem and human health. For instance, sulfur dioxide is a major precursor of acid rain (acid deposition) thereby affecting water bodies, soil, forests, buildings, and monuments.<sup>150</sup> In addition, sulfur dioxide represents the main source of atmospheric sulfate (SO<sub>4</sub><sup>2-</sup>) aerosols, which constitute a large fraction of fine particulate matter around the globe. As part of atmospheric particulate matter, sulfate aerosols may exert direct and indirect effects on climate and the global energy balance and act as cloud condensation nuclei.<sup>60</sup>

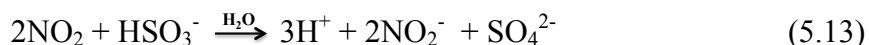
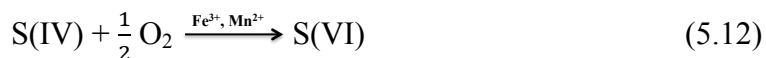
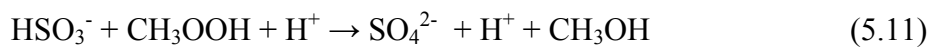
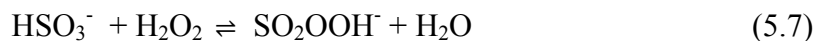
In the atmosphere, sulfur dioxide undergoes gas-phase oxidation by OH radicals as follows:



with a reaction rate constant of  $8.9 \times 10^{-13} \text{ cm}^3 \text{ molecule}^{-1} \text{ s}^{-1}$  for the oxidation of sulfur dioxide by the OH radical.<sup>2</sup> Under average global OH radical concentrations of ( $\sim 1 \times 10^6$  molecules  $\text{cm}^{-3}$ ) sulfur dioxide has an average lifetime of approximately one week, and therefore may undergo oxidation to sulfate during long-range transport.<sup>151</sup> In addition, sulfur dioxide undergoes oxidation into sulfate through heterogeneous reactions in the aqueous phase of fog, aerosols, and clouds.<sup>14</sup> Such aqueous-phase conversion of sulfur dioxide into sulfate is a two-step process. First, sulfur dioxide must dissolve, leading to the formation of the following species: hydrated sulfur dioxide ( $\text{SO}_2 \cdot \text{H}_2\text{O}$ ), the bisulfite ion ( $\text{HSO}_3^-$ ), and the sulfite ion ( $\text{SO}_3^-$ ). The dissolved sulfur dioxide may then exist as different chemical species according to the pH of the system. At a pH range of 2-7, the dominant specie is  $\text{HSO}_3^-$  whereas for  $\text{pH} < 2$ , sulfur dioxide exists in its hydrated form:  $\text{SO}_2 \cdot \text{H}_2\text{O}$ . At  $\text{pH} > 7$ ,  $\text{SO}_3^{2-}$  becomes the dominant form:



Second, aqueous-phase reactions involving atmospheric oxidants such as hydrogen peroxide, ozone, OH radical, organic peroxides, and nitrogen dioxide may convert dissolved sulfur dioxide (S(IV)) into sulfate (S(VI)):



However, the reaction yield for the oxidation of S(IV) by oxygen is insignificant, but can be significantly enhanced under the presence of metal catalysts such as Fe (III) and Mn (II).<sup>14</sup>

The heterogeneous oxidation of S(IV) into S(VI) by nitrogen dioxide is severely limited by the low solubility of nitrogen dioxide (Henry's Law Constant =  $1.0 \times 10^{-2}$  M atm<sup>-1</sup>) in water.<sup>2</sup> Therefore, under typical cloud conditions, the oxidation of S(IV) by nitrogen dioxide may not be a significant source of sulfate in the atmosphere. Nevertheless, in environments with elevated concentrations of nitrogen dioxide and neutralizing species such as ammonia (NH<sub>3</sub>), S(IV) may be efficiently oxidized into S(VI) due to the increased dissolution of sulfur dioxide in the aqueous phase of clouds, fog, or aerosols.<sup>152</sup> Furthermore, under the presence of neutralizing species such as

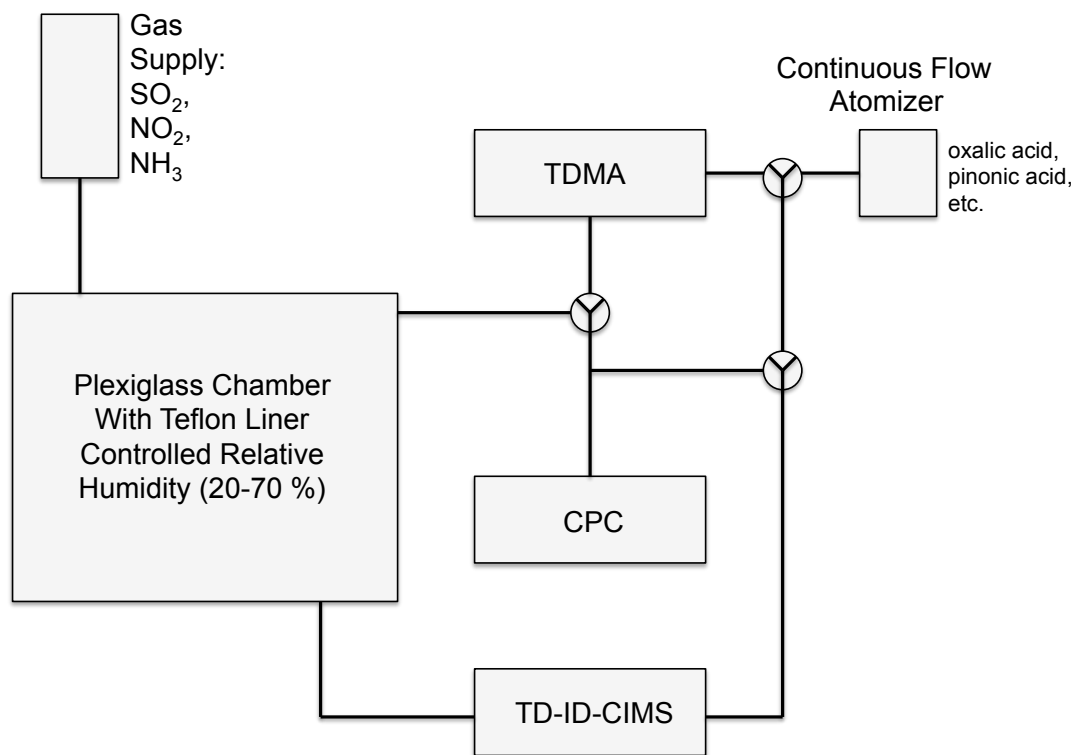


ammonia, the bisulfite ion may undergo complete dissociation into sulfite and then subsequent oxidation to sulfate. Behra et al. have studied the effect of ammonia on the oxidation of aqueous sulfur dioxide by ozone, determining that the reaction rate increases with increasing pH.<sup>153</sup> Therefore, in polluted urban environments (Beijing, China) with high relative humidity and increased levels of nitrogen dioxide and ammonia, the conversion of S(IV) into S(VI) may provide a significant source of sulfate in the atmosphere. Once formed in the aqueous phase of fog, clouds, and aerosols, sulfate may interact with atmospheric ammonia to form highly hygroscopic ammonium sulfate, which upon formation may mix with existing aerosols producing particle growth. Thus, the formation of sulfate from the oxidation of S(IV) by nitrogen dioxide may increase the formation of haze in highly polluted environments. Guo et al. have recently reported a direct correlation between atmospheric levels of sulfur dioxide, nitrogen dioxide, ammonia, PM, and elevated relative humidity levels prior to the formation of dense haze in Beijing, China.<sup>145</sup> Lee and Schwarz have investigated the oxidation of S(IV) by nitrogen dioxide, and reported that the reaction rate constant for the conversion of  $\text{HSO}_3^-$  to  $\text{SO}_4^{2-}$  is pH-dependent.<sup>154</sup>

In this chapter, we will discuss results from our chamber experiments aimed at exploring the conversion of sulfur dioxide into sulfate ( $\text{SO}_4^{2-}$ ) under the presence of nitrogen dioxide and ammonia. Such experiments may help explain the formation of haze and growth of PM in highly polluted environments such as Beijing, China.

## Experimental

Our experiments on the heterogeneous conversion of sulfur dioxide to sulfate in the aqueous phase of aerosols were conducted utilizing a 1 m<sup>3</sup> Plexiglass chamber equipped with Teflon film liner. Our chamber was equipped with a water based humidifier to control the internal relative humidity. Figure 24 illustrates the general arrangement of our instrumental system and its major components.



Tandem Differential Mobility Analyzer (TDMA)  
Thermal Desorption Ion-Drift Chemical Ionization Mass Spectrometer (TD-ID-CIMS)  
Condensation Particle Counter (CPC)

**Figure 24. Schematic representation of the 1 m<sup>3</sup> Teflon lined Plexiglass chamber connected to TDMA, CPC, and TD-ID-CIMS.**

In these experiments, the chamber was connected to a H-TDMA equipped with a CPC counter to measure the concentration and size distribution of the aerosols before and after treatment with sulfur dioxide, nitrogen dioxide, and ammonia. Furthermore, the chamber was also connected to our TD-ID-CIMS to measure the chemical composition of the aerosols before and after addition of the gases, and the concentration of newly formed sulfate. Therefore, our experimental setup allows for the simultaneous quantification of the particle concentration and measurement of the size distribution along with analysis of the chemical composition of the particles. However, for our experiments, our set up was operated in two modes: seeding mode and scanning mode.

#### *Seeding Mode*

For operation under seeding mode, size-selected (45 nm) oxalic acid particles were used as aerosol seeds in the chamber to provide particulate matter for the heterogeneous conversion of sulfur dioxide to sulfate. In seeding mode, the particles travelled from the atomizer to the TDMA for size selection, then to the chamber where the particles would remain for pre-determined periods of time to allow for the aerosols to react with the gaseous species. Thereafter, the aerosols would flow through the electrostatic particle collector (EPC) component of our TD-ID-CIMS and finally to the CPC. The oxalic acid aerosols were generated utilizing a continuous flow aerosol particle generator (TSI 3076) to atomize the aqueous solution of oxalic acid (1 wt%). The aerosol flow was diluted with dry nitrogen gas at a 4:1 ratio. After generation of the poly-dispersed aerosols and prior to entering the TDMA system for size discrimination,

the particles were heated to 343 K to remove excess humidity from the aerosol flow. The aerosol flow was then further dried using two Nafion tubes (PD-070-18T-12SS, Perma Pure). The particles were then charged by a  $^{210}\text{Po}$  radioactive source. For particle concentration measurements, a condensation particle counter (CPC, TSI 3762) was utilized. The relative humidity of the chamber was controlled using a 5 gallon water reservoir equipped with a water heater set at 307 K. Thereafter, a 2 SLPM nitrogen flow was passed through the water reservoir to produce humidified nitrogen that was subsequently introduced into the chamber. The RH in the chamber was monitored using a 24 V (DC) RH probe located downstream of the chamber. Typically, the size selected particle number concentration inside the chamber was elevated to  $5 \times 10^4 \text{ cm}^{-3}$  particles before gases were injected. Sulfur dioxide was obtained from Sigma-Aldrich whereas nitrogen dioxide and ammonia were obtained from Matheson. Gas samples of sulfur dioxide and nitrogen dioxide were injected into the chamber from pressurized lecture bottles utilizing a mass flow controller to monitor the flow of gas into the chamber. The concentrations in the lecture bottles were prepared by diluting sulfur dioxide or nitrogen dioxide with dry nitrogen to a nominal concentration of  $1 \times 10^3$  ppm. Ammonia ( $2 \times 10^3$  ppm) was used as received without dilution. Typically, sulfur dioxide or nitrogen dioxide were injected into the chamber at a flow rate of 0.1 SLPM for 2 minutes to add enough gas to equal 0.25 ppm in the chamber. Ammonia was added at a flow rate of 0.1 SLPM for 5 minutes to amount to a concentration of 1 ppm in the chamber. The particle and gas mixture was allowed to react for at least 45 minutes before setting the instruments to scanning mode to measure the size distribution of the particles after

exposure to the gases. For control purposes, we conducted separate experiments adding only one of the gases to oxalic acid particles using the concentrations mentioned above. We also conducted experiments in dark conditions, by wrapping the chamber in aluminum foil to eliminate the possibility of photo-driven oxidation of sulfur dioxide into sulfate. In addition, we also conducted experiments where one of the gases was reduced to 50% of the nominal concentration to measure the impact of reduced gas concentrations on the growth of the oxalic acid seed particles.

### *Scanning Mode*

For scanning mode, the flow lines were modified through the use of three-way valves to change the direction of the aerosol flow from the chamber to the TDMA. Subsequently, the aerosol flow was directed to the EPC component of our TD-ID-CIMS and finally to the CPC. Typically, after the “incubation” time of 45 minutes was complete, the humidified nitrogen flow was set at 2 SLMP to push the particles in the chamber unto the TDMA. The TDMA instrument was set to scan from 12 to 600 nm to measure the size distribution of the chemically modified aerosols. Considering that the concentration of particles in the chamber is significantly lower than the output given by the continuous flow atomizer, for scanning mode analysis the aerosol flow was generated by injection of humidified nitrogen at a flow of 2 SLPM into the chamber. After incubation, the aerosol particles in the chamber were into the TDMA system for size discrimination. Consistent with the seeding mode, the aerosol particles were heated to 343 K to remove excess humidity from the aerosol flow. The aerosol flow was then

further dried using two Nafion tubes (PD-070–18T-12SS, Perma Pure). The particles were then charged by a  $^{210}\text{Po}$  radioactive source. For particle concentration measurements, a condensation particle counter (CPC, TSI 3762) was utilized.

#### *Particle Collection and Chemical Analysis by TD-ID-CIMS*

The chemical composition of the aerosols was analyzed using our TD-ID-CIMS instrument. Our TD-ID-CIMS is equipped with an EPC capable of collecting aerosols from 2 to 200 nm. We have discussed the joint collection of aerosols in our EPC and the operation of our TD-ID-CIMS and in full detail in chapter II. For our sulfate production experiments, the aerosol flow crossed the EPC at 1.5 SLPM with a dry nitrogen sheath flow of 0.3 SLPM. The particle flow passed through the EPC for 45 minutes and particles were collected using a collecting voltage of 3300 V (DC) on our platinum based collection/desorption filament. After collection, the aerosol sample was introduced into the ionization chamber and the filament was heated to 600 K to evaporate the sample by applying a 2 V (AC) voltage. Chemical ionization was achieved utilizing a  $\text{CO}_3/\text{CO}_4^-$  ionization scheme to generate negative ions for negative mode mass spectrometry. Mass spectrometry experiments were conducted on a triple quadrupole (QqQ) Extrel ELQ 400 instrument utilizing Selected Ion Monitoring (SIM) for the ions of interest (i.e. sulfate, oxalic acid)

## Results and Discussion

For these experiments, we have focused our analysis on the heterogeneous conversion of sulfur dioxide into sulfate under the presence of nitrogen dioxide and ammonia. Considering that the heterogeneous conversion of sulfur dioxide to sulfate may take place in the aqueous phase of fog, clouds, and aerosols, the detection of sulfate in oxalic acid particles serves as an indicator for the heterogeneous conversion of sulfur dioxide into sulfate in aerosols. This in turn is representative of the formation of sulfate in PM in polluted environments with high levels of nitrogen dioxide, ammonia and sulfur dioxide.

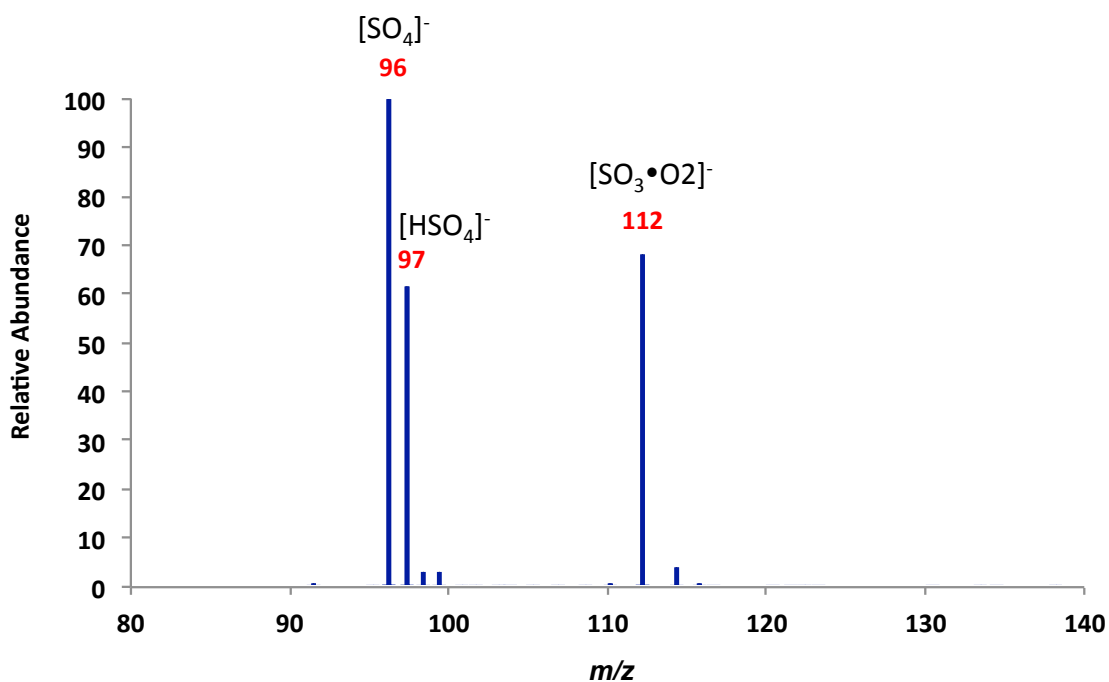
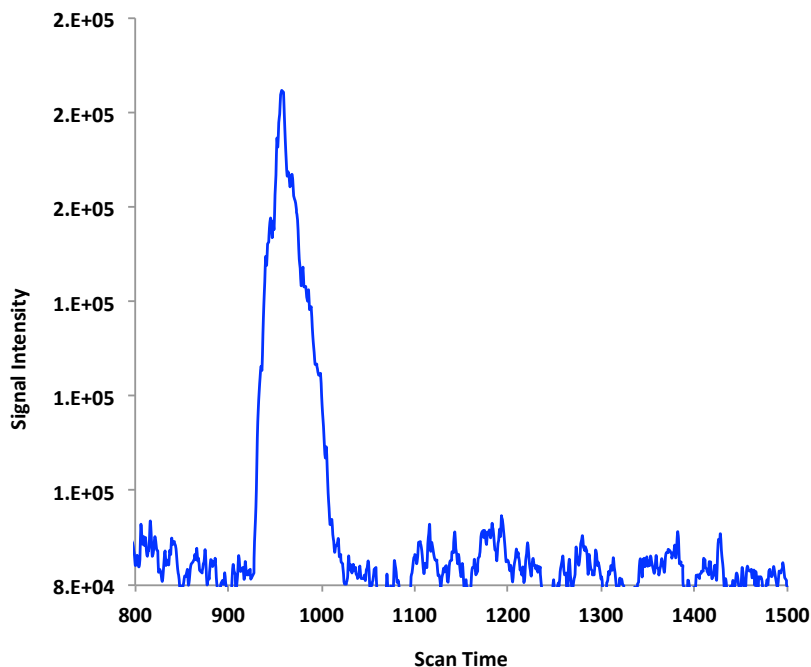


Figure 25. TD-ID-CIMS spectrum of ammonium sulfate standard solution.

For the detection of newly formed sulfate, we have utilized our TD-ID-CIMS instrument to analyze the chemical composition of oxalic acid particles after exposure to the gas mixture. Figure 25 illustrates the mass spectrometry analysis for an ammonium sulfate standard solution, which shows three major peaks: first the sulfate ion  $[\text{SO}_4]^-$  at  $m/z = 96$ , second the bisulfate ion  $[\text{HSO}_4]^-$  at  $m/z = 97$ , and finally the oxygen adduct of  $[\text{SO}_3 \cdot \text{O}_2]^-$  at  $m/z = 122$ . The ion at  $m/z = 96$  is thus our reference ion.

In our particle collection experiments, we have detected the presence of the sulfate ion in oxalic acid particles after the particles have grown inside the chamber. Figure 26 shows a representative ionogram for the sulfate ion as measured by our TD-ID-CIMS instrument in the negative ion mode.



**Figure 26. TD-ID-CIMS ionogram of sulfate in collected nanoparticles. Collection time = 40 minutes. Selected Ion Monitoring (SIM) for the sulfate ion at  $m/z$  96.**



Figure 27 depicts the TD-ID-CIMS analysis of oxalic acid nanoparticles after exposure to the gas mixture at 65 % RH, with a change in diameter from 45 to 75 nm. Comparison of the mass spectra reveals an exact match for the observed ions. Our mass spectrometry analysis shows that the oxalic acid particles contained sulfate and oxalic acid. The mass spectrum shows ions at  $m/z = 89, 96, 97, 112,$  and  $122$  for [Oxalic Acid-H]<sup>-</sup>, SO<sub>4</sub><sup>-</sup>, HSO<sub>4</sub><sup>-</sup>, [SO<sub>3</sub>•O<sub>2</sub>]<sup>-</sup> and [Oxalic Acid•O<sub>2</sub>]<sup>-</sup> respectively.

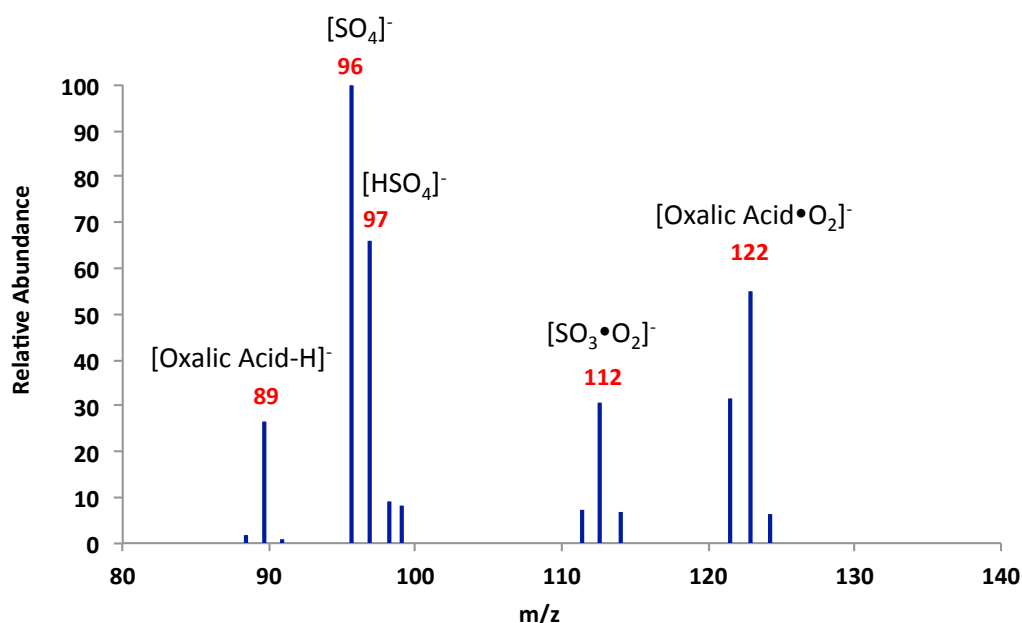


**Figure 27. TD-ID-CIMS of oxalic acid nanoparticles after exposure to sulfur dioxide, nitrogen dioxide, and ammonia at 65 % RH. Particle diameter increased from 45 to 75 nm.**

These results indicate that sulfate forms inside the chamber as a result of the heterogeneous oxidation of sulfur dioxide by nitrogen dioxide under the presence of ammonia, leading to particle growth. We have monitored particle growth by parametrizing the particle growth factor (GF) utilizing a TDMA system, coupled to our chamber and

TD-ID-CIMS. Therefore, in these preliminary experiments we have also analyzed the effects of changes to the concentration levels of sulfur dioxide, ammonia, and nitrogen dioxide on the GF of the oxalic acid aerosols. Furthermore, we have also analyzed the effect of light on particle growth due to sulfate production. Figure 28 depicts the effect of gas concentration on the oxalic acid particle GFs. Our data shows that the concentration of the gasses exerts a direct effect on particle growth. For example, when sulfur dioxide and nitrogen dioxide were each added at a concentration of 0.25 ppm inside the chamber, with ammonia added at a concentration of 1 ppm, the growth factor (GF) for 45 nm oxalic acid nanoparticles was approximately 1.56 at 65% RH. However, when the concentration of sulfur dioxide was reduced by 50% (i.e. 0.13 ppm) and the concentrations of nitrogen dioxide and ammonia were kept constant, the growth factor for 45 nm oxalic acid nanoparticles decreased to approximately 1.33. Such results suggest that the growth of PM due to the conversion of sulfur dioxide to sulfate is synergetic in nature, and thus, that as more sulfate is generated by the presence of nitrogen dioxide and ammonia in the system, PM diameter increases.

Furthermore, Figure 28 shows that when oxalic acid nanoparticles are exposed only to sulfur dioxide, without the presence of nitrogen dioxide nor ammonia, the GF is equal to 1, showing that there is no particle growth. Interestingly, Figure 28 also shows that after the concentration of nitrogen dioxide was reduced by 50% while the concentration of sulfur dioxide and ammonia were kept constant, the GF was approximately 1.56 at 65% RH.

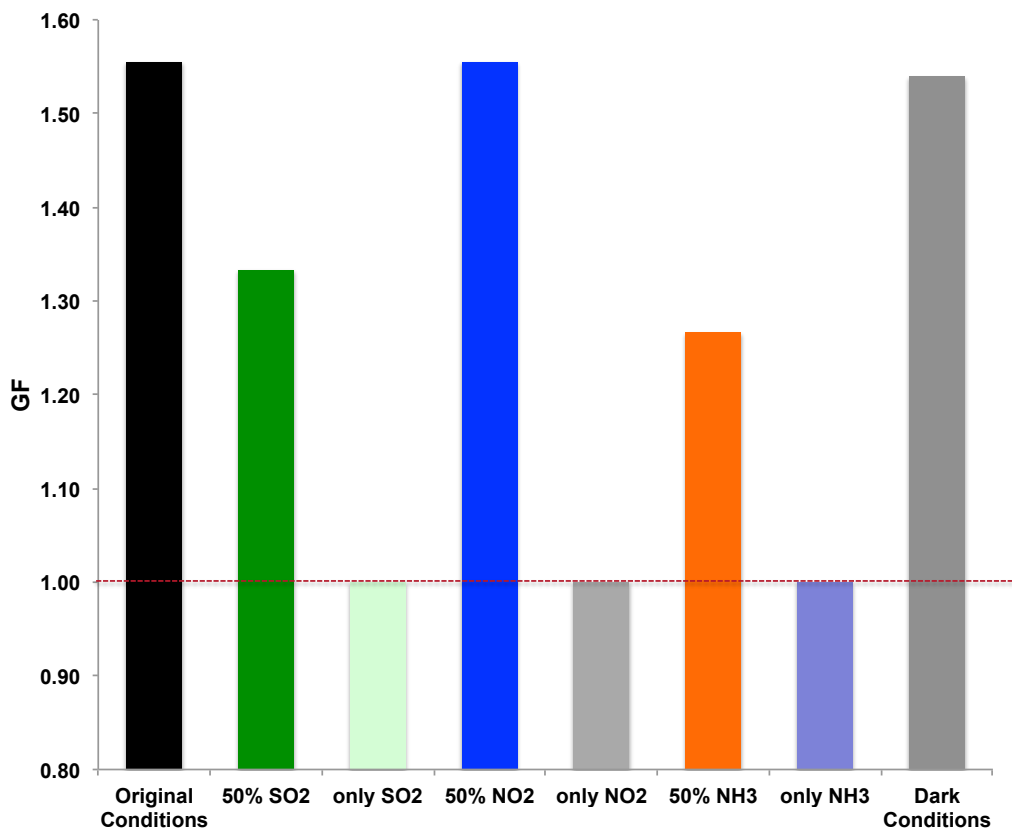


**Figure 28.** Comparison of growth factor for 45 nm oxalic acid nanoparticles after exposure to gases at 65% RH. The black bar represents the experiments carried with all gases at original conditions (2.6 ppm SO<sub>2</sub> and NO<sub>2</sub>, 10 ppm Ammonia). The green bar represents experiments with the concentration of sulfur dioxide reduced by 50%. The light green bar represents experiments with only sulfur dioxide added to oxalic acid particles. The blue bar represents experiments with nitrogen dioxide reduced by 50%. The light gray bar represents experiments with only nitrogen dioxide added to oxalic acid particles. The orange bar represents experiments with ammonia reduced by 50%. The purple bar represents experiments with only ammonia added to oxalic acid particles. The dark grey bar represents experiments with the chamber wrapped in aluminum foil to prevent light from entering the chamber.

However, when only nitrogen dioxide was added to the oxalic acid particles, the GF was 1. For ammonia, when the concentration of sulfur dioxide and nitrogen dioxide was maintained at 2.6 ppm, but the concentration of ammonia was reduced by 50 %, the GF for the oxalic acid particles was approximately 1.27 at 65% RH.

Additionally, when only ammonia was added to the oxalic acid seeds in the chamber, the particles did not grow, and therefore the GF was equal to 1. As the particles did not grow after exposure to ammonia only, it is clear that the growth of the particles is due to the formation of sulfate and not by the acid-base reaction of oxalic acid and ammonia. Considering that Prenni et al. have demonstrated that internally mixed particles containing ammonium sulfate and oxalic acid are hygroscopic, with HGF of  $\approx 1.2$  at 65 % RH,<sup>139</sup> the formation of internally mixed aerosols could lead to bias in our results. But such extent of growth could not explain our observed GF as recorded by our TDMA at  $\approx 1.5$  at 65 % RH respectively. However, as the oxalic acid particles did not grow after exposure to ammonia only, the potential growth of the oxalic acid particles due to the acid-base reaction with ammonia is therefore discarded. In addition, we conducted experiments in dark conditions in order to explore the effect of light on the synergetic formation of sulfate. Under dark conditions, the GF for the oxalic acid particles was approximately 1.54 at 65 % RH. Our data then suggests that the formation of sulfate from sulfur dioxide, nitrogen dioxide, and ammonia at 65 % RH proceeds unaltered by the presence or absence of light. Therefore, our results indicate that the growth of particulate matter requires the combined presence of SO<sub>2</sub>, NO<sub>2</sub>, NH<sub>3</sub>, and high RH conditions.

To provide further confirmation regarding the production of sulfate inside the chamber, we have also analyzed the aqueous condensation accumulated inside the chamber utilizing our TD-ID-CIMS instrument in the negative ion mode. Figure 29 depicts the mass spectrum of the analyzed chamber water.

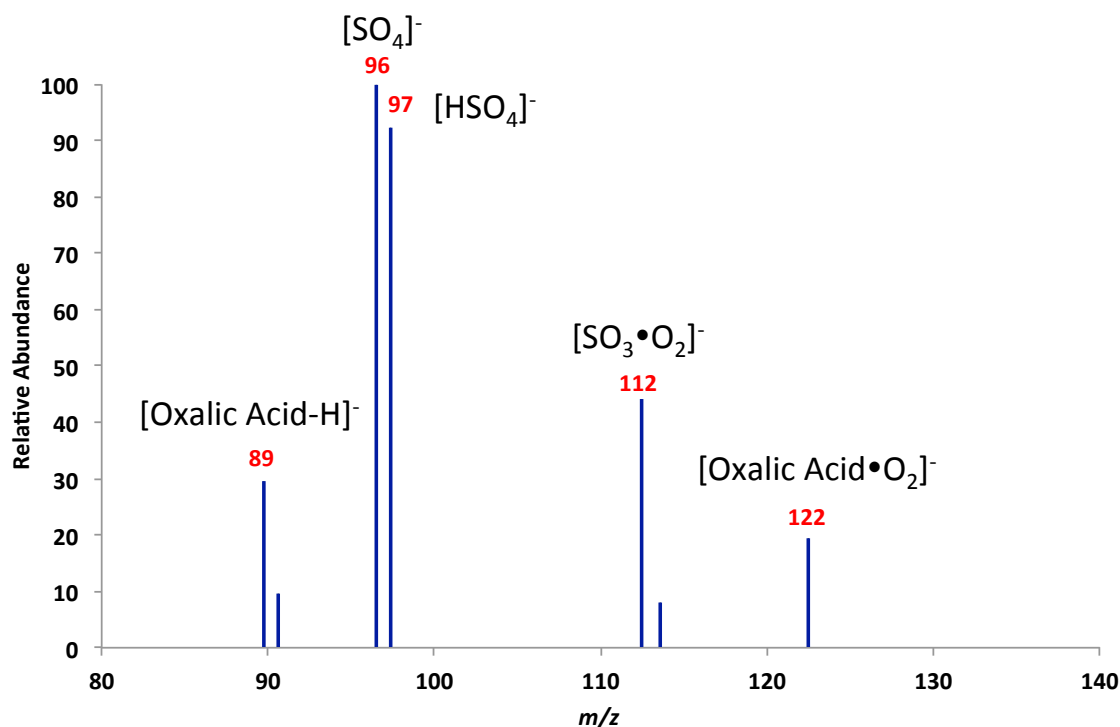


**Figure 29. TD-ID-CIMS analysis of the aqueous condensation inside the Teflon Chamber.**

Our mass spectrometry analysis of the chemical composition of the aqueous condensation inside the chamber shows the presence of sulfate and oxalic acid on the water sample. Thus, our mass spectrometry data confirms that the gaseous sulfur dioxide is converted to sulfate under the presence of nitrogen dioxide and ammonia inside the chamber. In addition, the TD-ID-CIMS analysis of chamber water matches the mass spectra of collected oxalic acid particles after exposure to the gas mixture.

Our TDMA and TD-ID-CIMS data indicate that the heterogeneous conversion of sulfur dioxide to sulfate under the presence of nitrogen dioxide and ammonia is sensitive to the concentrations of the gases. Furthermore, such concentration dependence also translates to particle growth for pre-existing aerosols (i.e. the oxalic acid seeds). In turn,

such observations suggest a synergetic effect linking the  $\text{NO}_2$  driven heterogeneous generation of sulfate to particulate matter growth for environments with high levels of ammonia. Thus, our results provide insight into the formation of haze in polluted environments where particulate matter is exposed to high levels of sulfur dioxide, nitrogen dioxide, and ammonia under high RH conditions leading to significant particle growth as reported by Guo et al.<sup>145</sup>

### Summary

Seinfeld and Pandis have written that under typical cloud conditions, the  $\text{NO}_2$  mediated conversion of S(IV) to S(VI) is limited by the low solubility of nitrogen dioxide in water.<sup>2</sup> Here, we demonstrate that if the environment contains elevated levels of ammonia and high % RH, the production of sulfate is not only enhanced, but it also produces significant particle growth for pre-existing aerosols. Such findings may help explain the accelerated formation and growth of particulate matter in polluted environments such as Beijing, China.

In Beijing, sulfur dioxide, nitrogen dioxide, ammonia, and organic particulate matter consistently exceed healthy atmospheric concentration levels, leading to respiratory and cardiovascular diseases, low visibility, and poor air quality. Furthermore, it has been reported that in Beijing, haze formation events are accompanied by increased levels of  $\text{SO}_2$ ,  $\text{NO}_2$ , and  $\text{NH}_3$  under high relative humidity conditions.<sup>145</sup> In this chapter, we have provided evidence that sulfate produced by the heterogeneous oxidation of gaseous sulfur dioxide by nitrogen dioxide under the presence of ammonia may lead to

significant SOA growth. Our results indicate that pre-existing aerosol particles significantly grown in size when exposed to sulfur dioxide, nitrogen dioxide, and ammonia at high RH (i.e. 65%). Furthermore, our results also show that sulfate is present not only on the particles, but also on the accumulated aqueous condensation inside the chamber.

In our laboratory experiments, our representative SOA particles grew faster than in Beijing (1 vs. 4 hr),<sup>145</sup> but such difference in time-scale maybe explained by the higher concentrations utilized in our study with respect to typical atmospheric conditions (ppb vs. ppm) in Beijing. Moreover, our experiments were conducted utilizing pure oxalic acid particles, whereas in Beijing, SOA may contain a wide array of organic compounds; thus, future experiments may address the effect of utilizing multicomponent particles (i.e. m-toluic, cis-pinonic, succinic, malic, adipic, etc) as particle seeds on SOA growth. However, our utilized concentrations are lower than the maximum permissible sulfur dioxide exposure concentrations (5 ppm) allowed by the United States Department of Labor Occupational Safety & Health Administration (OSHA) for industrial activity.<sup>155</sup> Therefore, our experiments indicate that the potential impact of the conversion of sulfur dioxide to sulfate on SOA and air quality is significant, even below the current regulations for human exposure to sulfur dioxide.

Our experiments also show that the heterogeneous formation of sulfate as performed inside the chamber is dependent on the concentration of the gaseous species. For example, reducing the concentration of either SO<sub>2</sub> or NH<sub>3</sub> decrease the GF of the particles significantly. On the other hand, decreasing NO<sub>2</sub> did not seem to decrease the

GF of the seed aerosols, suggesting the  $\text{SO}_2$  is the limiting reagent in this chemical reaction. Our data also supports a synergetic effect for the growth of the particles, as individual injection of each gaseous species did not produce particle growth. Thus, we can conclude that the production of sulfate from the heterogeneous oxidation of sulfur dioxide by nitrogen dioxide under the presence of ammonia and high relative humidity leads to rapid growth of particular matter representative of Beijing haze.



## CHAPTER VI

### CONCLUSIONS

Atmospheric aerosols represent a monumental challenge in science. Their effects on human health and the planetary radiation balance pose global challenges that demand scientific answers based on rigorous experimentation. In this dissertation, we have discussed experimental results aimed at better understanding the composition, formation, growth, and physicochemical properties of SOA. Our novel TD-ID-CIMS provides analysis of the chemical composition of aerosols with different diameters, ranging from the nucleation to the accumulation mode. For example, our TD-ID-CIMS has proven useful in analyzing the chemical composition of sulfuric acid particles after exposure to organic epoxide compounds providing evidence for the acid catalyzed formation of oligomers responsible for particle growth.

The new TD-ID-CIMS has also proven capable to analyze the chemical composition of alkylammonium carboxylate aerosols after evaporation, showing that alkylammonium carboxylates retain their chemical composition without dissociating into the acid and base precursors after thermal desorption. TD-ID-CIMS has also proven useful in studying the chemical composition of 2 nm aerosol particles, which are near the diameter of the critical nuclei clusters necessary for new particle formation. Our TD-ID-CIMS has shown that the oxidation of alpha-pinene generates several oxidation products, and that such organic compounds are found in 2 nm particles. Such organic products may hydrogen bond to form heterodimers, depending on their molecular

structure and functional groups. Therefore, with the formation of various organic acids, the possible combinations for the formation of heterodimers increase, leading to new particle formation. Therefore, TD-ID-CIMS represents a significant development for the analysis of SOA formation, growth, and composition.

In this dissertation, we have also explored the chemistry of carbonyl compounds on acidic surfaces. Carbonyl compounds are ubiquitous in the atmosphere, and represent a significant fraction of organic particulate matter in polluted environments such as Mexico City. Thus, we have discussed the heterogeneous chemistry of gaseous glyoxal on sulfuric acid solutions. Our results indicate that the uptake coefficient and Henry's Law constant are dependent not only on temperature, but also on acid concentration. Our results support a hydration driven mechanism where glyoxal may be converted to diols and tetrols, which in turn may oligomerize and then lead to SOA formation. Such mechanism may then offer insight into the discrepancy between the measured and predicted glyoxal levels in Mexico City, where a "missing sink" for glyoxal has been the focus of investigation by other laboratories.

Atmospheric alkylamines represent a significant fraction of nitrogen containing atmospheric particulate matter. However, due to the substitution of one or more hydrogen atoms by an alkyl group, alkylamines have higher basicity than ammonia. Such high basicity generates highly efficient acid-base reactions between alkylamines and weak organic acids found in the atmosphere. In turn, those acid-base reactions may lead to formation of various alkylammonium salts, each with unique hygroscopicity and cloud condensation nuclei activity. Our measurements have shown that the

alkylammonium salts are more hygroscopic than their pure organic acid counterparts; and that the hygroscopicity is closely dependent on the molecular weight of the acid precursor. Our results indicate that the hygroscopicity of alkylammonium carboxylates decreases with molecular weight. For example, small organic acids such as oxalic or succinic acid mixed with an alkylamine generate highly hygroscopic salts with HGF values  $> 2$  at 90 % RH. On the other hand, larger molecules such as azelaic acid generate salts with low hygroscopicity with HGF close to 1.1 at 90% RH. In our work, we have also derived the hygroscopicity parameter ( $\kappa$ , kappa) under three methods: HGF, CCN, and the mixing rule approximation. Our calculations indicate that the HGF derived  $\kappa$  is higher than the mixing rule approximation  $\kappa$ ; whereas the CCN derived  $\kappa$  values are lower than the mixing rule approximation  $\kappa$  values. Such discrepancy may be partially attributed to the differences in the physicochemical properties of the alkylammonium salts such as surface tension, density, and molecular structure. However, such discrepancy also reflects the limitations of the current mathematical model to describe hygroscopicity, as it does not include molecular structure (i.e. functional groups) in its approximations and may therefore underestimate the magnitude of  $\kappa$  for compounds containing hydrophilic functional groups.

In this dissertation, we have also discussed chamber experiments regarding the conversion of sulfur dioxide into sulfate under the presence of nitrogen dioxide and ammonia and high relative humidity conditions. Our results suggest that this oxidation pathway is dependent on gas concentrations and the presence of ammonia. Therefore, this conversion pathway may be a significant source of sulfate in the aqueous-phase of

clouds and aerosols where ammonia levels are high. At the same time, the increased production of sulfate may promote the growth of PM, as reflected by the size changes of 45 nm oxalic acid aerosols observed in our chamber experiments under different chemical conditions. Therefore, our results suggest that for highly polluted environments (i.e. Beijing, China) the elevated levels of sulfur dioxide, nitrogen dioxide, and ammonia, combined with elevated relative humidity and existing PM offer the “right” conditions for the accelerated conversion of sulfur dioxide into sulfate. In turn, the increased conversion of sulfur dioxide into sulfate in the aqueous-phase of clouds and aerosols may promote the formation of haze by increasing the size and concentration of particulate matter in the atmosphere.

Currently, secondary organic aerosols (SOA) represent one of the most complex challenges in analytical chemistry and atmospheric science. Such challenging nature is not only due to the chemical composition and physicochemical properties of SOA; but also due to their impact on the planetary radiation balance, climate interactions, pollution, and human health. Thus, the analysis and investigation of the chemical properties of SOA requires the synergy of state of the art instrumentation, relevant experiments, and the continuous development of new techniques that can provide a better understanding regarding SOA and their formation.

The present dissertation has discussed experimental work that opens exciting future studies in the field of atmospheric chemistry focused on SOA formation, composition, and properties. For instance, our TD-ID-CIMS instrument may be utilized to analyze the chemical composition of critical nuclei clusters composed of weak

organic acids mixed with alkylamines and/or sulfuric acid. Once the chemical composition of the critical nuclei cluster is determined, the nucleation parameter may be calculated from the properly calibrated gas-phase concentration of the nucleating species and the formation of  $< 2$  nm particles measured by a nano-DMA assembly. In addition, as a continuation of our chamber experiments, our TD-ID-CIMS may also be coupled to a reaction chamber to study the effect of molecular structure on new particle formation efficiency for organic acids mixed with sulfuric acid, ammonia, water, and amines. Furthermore, the combination of our TD-ID-CIMS and a TDMA assembly may be applied to study the interactions of newly formed sulfate aerosols with size selected soot particles. Such experiments would serve to complement our chamber work on sulfate generation and its interaction with pre-existing atmospheric aerosols. Considering that soot is not hygroscopic, the extent of any growth may be attributed only to the gain of sulfate by the particle, without the risk of growth bias due to the increased hygroscopicity of sulfate aerosols.

Future experiments may also extend our measurements utilizing a low-pressure laminar fast flow reactor coupled to ID-CIMS to study the heterogeneous chemistry of gas-phase glyoxal and ammonium or alkylammonium-carboxylate surfaces. Such studies would help to elucidate the extent of reaction between gas-phase dicarbonyls and nitrogen containing particulate matter under different conditions of humidity and concentration. Finally, laboratory measurements regarding the effect of inorganic impurities such as sodium chloride on the cloud forming potential of alkylammonium carboxylate aerosols may provide insight into the interactions of sea salt aerosols with

highly hygroscopic SOA. Such measurements may in turn provide a better understanding of the climate implications of SOA mixed with naturally occurring aerosols. In addition, it would be interesting to explore the extent and timescale of sulfate driven growth of aerosols composed of other organic acids such as cis-pinonic, malic, adipic, azelaic, or toluic acid and mixtures therein. Such studies could provide insight on the synergetic mechanism behind Beijing haze formation.

In closing remarks, this dissertation provides experimental results regarding the development and application of advanced instrumentation to study the molecular composition and physicochemical properties of SOA and their formation. Our results demonstrate that the chemical composition of SOA can now be measured for particles as small as 2 nm. Such capability provides analysis of the chemical composition of critical nuclei clusters, essential for new particle formation, as well as other chemical systems involved in SOA formation and growth. Our results also demonstrate that the chemical composition of SOA directly affects the physicochemical properties of the particle such as hygroscopicity and CCN, thereby affecting the direct and indirect effects of aerosols on the global radiation balance. In addition, our results discuss two novel reaction pathways in the atmosphere that may lead to formation of SOA, one dealing with carbonyls and the other dealing with sulfur dioxide. The experiments discussed in this dissertation are aimed at providing a better understanding on the formation and composition of SOA so that we, as a society may ensure the quality of the air we breathe today, and for generations to come.

## REFERENCES

1. Zhang, R. Getting To The Critical Nucleus Of Aerosol Formation. *Science* **2010**, 328, 1366-1367.
2. Seinfeld, J.H.; Pandis, S.N. *Atmospheric Chemistry and Physics: From Air Pollution to Climate Change*. 2nd ed. Wiley: New York, **2006**.
3. Preining, Othman, Davis, E. J. (Eds) *History of Aerosol Science. Proceedings of the Symposium on the History of Aerosol Science*. Verlag der Österreichische Akademie der Wissenschaften: Vienna, **2000**.
4. Schröder, W.; Wiederkehr, K. H.; Johann Kiessling. The Krakatoa Event And The Development Of Atmospheric Optics After 1883. *Notes Rec. R. Soc. Lond.* **2000**, 54, 2, 249-258.
5. Seinfeld, J.H.; Pankow, J.F. Organic Atmospheric Particulate Material. *Annu. Rev. Phys. Chem.* **2003**, 54, 121-140.
6. Hallquist, M.; Wenger, J.C. Baltensperger, U.; Rudich, Y.; Simpson. D. et al. The Formation, Properties, And Impact Of Secondary Organic Aerosol: Current And Emerging Issues. *Atmos. Chem. Phys.* **2009**, 9, 5155-5236.
7. Zhang, R. Y.; Khalizov, A.; Wang, L.; Hu, M.; Xu, W. Nucleation And Growth Of Nanoparticles In The Atmosphere. *Chem. Rev.* **2012**, 112, 1957-2011.
8. Zhang, R.; Suh, I.; Zhao, J.; Zhang, D.; Fortner, E.C. et al. Atmospheric New Particle Formation Enhanced By Organic Acids. *Science* **2004**, 304, 1487-1490.

9. Zhang, R.; Wang, L.; Khalizov, A.F.; Zhao, J.; Zheng, J. et al. Formation Of Nanoparticles Of Blue Haze Enhanced By Anthropogenic Pollution. *Proc. Natl. Acad. Sci. USA* **2009**, 106, 17650-17654.
10. Wang, L.; Khalizov, A.F.; Zheng, J.; Xu, W.; Ma, Y. et al. Atmospheric Nanoparticles Formed From Heterogeneous Reactions Of Organics. *Nature Geosci.* **2010**, 3, 238-242.
11. McMurry, P.H.; Fink, M.; Sakurai, H.; Stolzenburg, R. L.; Mauldin, J. N. et al. A Criterion For New Particle Formation In The Sulfur-Rich Atlanta Atmosphere. *J. Geophys. Res.* **2005**, 110, D22S02.
12. Kulmala, M.; Vehkamäki, H.; Petäjä, T.; Dal Maso, M.; Lauri, A. et al. Formation and growth rates of ultrafine atmospheric particles; a review of observations. *J. Atmos. Chem. Phys.* **2004**, 35, 2, 143-176.
13. Spracklen, D.V.; Carslaw, K.S.; Merikanto, J.; Mann, G. W.; Reddington, C. L.; et al. Explaining Global Surface Aerosol Number Concentrations In Terms Of Primary Emissions And Particle Formation. *J. Atmos. Chem. Phys.* **2010**, 10, 4475-4793.
14. Zhang, R.; Wang, G.; Guo, S.; Zamora, M. L.; Ying, Q. et al. Formation Of Urban Fine Particulate Matter. *Chem. Rev.* **2015**, 115, 10, 3803-3855.
15. Kleinstreuer, C.; Zhang, Z.; Donohue, J.F. Targeted Drug-Aerosol Delivery In The Human Respiratory System. *Annu. Rev. Biomed. Eng.* **2008**, 10, 195-220.
16. Pope, C. A.; Ezzati, M.; Dockery, D.W. Fine-Particulate Air Pollution And Life Expectancy In The United States. *New. J. Engl. Med.* **2009**, 360, 376-386.



17. Sun, J.; Ariya, P.A. Atmospheric Organic And Bio-Aerosols As Cloud Condensation Nuclei (CCN): A Review. *Atmos. Environ.* **2006**, *40*, 795-820.
18. Intergovernmental Panel on Climate Change (IPCC). Climate Change 2013: The Physical Science Basis. Contribution of Working Group I to the Fifth Assessment Report of the Intergovernmental Panel on Climate Change; Cambridge University Press: Cambridge, U.K. and New York, U.S.A., **2013**, (<http://www.ipcc.ch/report/ar5/wg1/>).
19. Fan, J.; Zhang, R.; Tao, W.-K.; Mohr, K. Effects Of Aerosol Optical Properties On Deep Convective Clouds And Radiative Forcing. *J. Geophysical. Res.* **2008**, *113*, D8.
20. Li, G.; Wang, Y.; Zhang, R. Implementation Of A Two-Moment Bulk Microphysics Scheme To The WRF Model To Investigate Aerosol-Cloud Interaction. *J. Geophysical. Res.* **2008**, *113*, D15.
21. Zhang, R.; Li, G.; Fan, J.; Wu, D. L.; Molina, M. J. Intensification Of Pacific Storm Track Linked To Asian Pollution. *Proceedings of the National Academy of Sciences* **2007**, *104*, 13, 5295-5299.
22. Pope III, C. A.; Douglas W. D. Health Effects Of Fine Particulate Air Pollution: Lines That Connect. *Journal of the air & waste management association* **2006**, *56*, 6, 709-742.
23. Qiu, C.; Wang, L.; Lal, V.; Khalizov, A. F.; Zhang, R. Heterogeneous Reactions Of Alkylamines With Ammonium Sulfate And Ammonium Bisulfate. *Environmental Sci. Technol.* **2011**, *45*, 11, 4748-4755.

24. Qiu, C.; Zhang, R. Multiphase Chemistry Of Atmospheric Amines. *Phys. Chem. Chem. Phys.* **2013**, *15*, 5738-5752.
25. Lu, C.; Rashinkar, S. M.; Dasgupta, P. K. Semicontinuous Automated Measurement of Organic Carbon in Atmospheric Aerosol Samples. *Analytical Chemistry* **2010**, *82*, 4, 1334-1341.
26. Pratt, A.K.; Prather, K. A. Mass Spectrometry Of Atmospheric Aerosols-Recent Developments And Applications. Part I: Off-Line Mass Spectrometry Techniques. *Mass Spectrom. Reviews* **2012**, *31*, 1, 1-16.
27. Pratt, A.K.; Prather, K. A. Mass Spectrometry Of Atmospheric Aerosols—Recent Developments And Applications. Part II: On - Line Mass Spectrometry Techniques. *Mass Spectrom. Reviews* **2012**, *31*, 1, 17-48.
28. Johnston, M. V. Sampling And Analysis Of Individual Particles By Aerosol Mass Spectrometry. *J. Mass Spectrom.* **2000**, *35*, 5, 585–595.
29. Murphy, D. M. The Design Of Single Particle Laser Mass Spectrometers. *Mass Spectrom. Rev.* **2007**, *26*, 2, 150–165.
30. Lee, S. H.; Allen, H. C. Analytical Measurements Of Atmospheric Urban Aerosol. *Anal. Chem.* **2012**, *84*, 3, 1196–1201.
31. Nash, D. G.; Baer, T.; Johnston, M. V. Aerosol Mass Spectrometry: An Introductory Review. *Int. J. Mass Spectrom.* **2006**, *258*, 1-3, 2–12.

32. Wexler, A. S.; Johnston, M. V. What have we learned from highly time-resolved measurements during EPA's Supersites Program and related studies?. *J. Air & Waste Manage. Assoc.* **2008**, *58*, 2, 303–319.
33. Prather, K. A.; Hatch, C. D.; Grassian, V. H. Analysis of atmospheric aerosols. *Annu. Rev. Anal. Chem.* **2008**, *1*, 485–514.
34. Zelenyuk, A.; Imre, D. Single particle laser ablation time-of-flight mass spectrometer: an introduction to SPLAT. *Aerosol Sci. Technol.* **2005**, *39*, 6, 554–568.
35. Drewnick, F. Speciation analysis in on-line aerosol mass spectrometry. *Anal. Bioanal. Chem.* **2012**, *404*, 8, 2127–2131.
36. Jayne, J. T.; Leard, D. C.; Zhang, X. F.; Davidovits, P.; Smith, K. A.; Kolb, C. E.; Worsnop, D. R. Development of an aerosol mass spectrometer for size and composition analysis of submicron particles. *Aerosol Sci. Technol.* **2000**, *33*, 1-2, 49–70.
37. Aiken, A. C.; de Foy, B.; Wiedinmyer, C.; DeCario, P. F.; Ulbrich, I. M.; et al. Mexico city aerosol analysis during MILAGRO using high resolution aerosol mass spectrometry at the urban supersite (T0)–Part 2: Analysis of the biomass burning contribution and the non-fossil carbon fraction. *Atmos. Chem. Phys.* **2010**, *10*, 5315–5341
38. He, L. Y.; Huang, X. F.; Xue, L.; Hu, M.; Lin, Y.; et al. Submicron aerosol analysis and organic source apportionment in an urban atmosphere in Pearl River

- Delta of China using high-resolution aerosol mass spectrometry. *J. Geophys. Res.* **2011**, *116*, DOI: 10.1029/2010JD014566, D12304.
39. Wang, S.; Zordan, C. A.; Johnston, M. V. Chemical characterization of individual, airborne sub-10-nm particles and molecules. *Anal. Chem.* **2006**, *78*, 6, 1750-1754.
40. Voisin, D.; Smith, J. N.; Sakurai, H.; McMurry, P. H.; Eisele, F. L. Thermal desorption chemical ionization mass spectrometer for ultrafine particle chemical composition. *Aerosol Sci. Technol.* **2003**, *37*, 6, 471-475.
41. Smith, J. N.; Moore, K. F.; McMurry, P. H.; Eisele, F. L. Atmospheric measurements of sub-20 nm diameter particle chemical composition by thermal desorption chemical ionization mass spectrometry. *Aerosol Sci. Technol.* **2004**, *38*, 2, 100-110.
42. Smith, J. N.; Rathbone, G. J. Carboxylic acid characterization in nanoparticles by thermal desorption chemical ionization mass spectrometry. *Int. J. Mass Spectrom.* **2008**, *274*, 1-3, 8-13.
43. Held, A.; Rathbone, G. J.; Smith, J. N. A thermal desorption chemical ionization ion trap mass spectrometer for the chemical characterization of ultrafine aerosol particles. *Aerosol Sci. Technol.* **2009**, *43*, 3, 264-272.
44. De Gouw, J.; Warneke, C.; Karl, T.; Eerdekens, G.; van der Veen, C.; Fall, R. Sensitivity and specificity of atmospheric trace gas detection by proton-transfer-reaction mass spectrometry. *Int. J. Mass Spectrom.* **2003**, 223-224, 365-382.

45. Zhang, R.; Leu, M.T.; Keyser, L.F. Hydrolysis of  $\text{N}_2\text{O}_5$  and  $\text{ClONO}_2$  on the  $\text{H}_2\text{SO}_4/\text{HNO}_3/\text{H}_2\text{O}$  ternary solutions under stratospheric conditions. *Geophys. Res. Lett.* **1995**, *22*, 1493-1496.
46. Zhao, J.; Zhang, R.; Misawa, K.; Shibuya, K. Experimental product study of the OH-initiated oxidation of m-xylene. *J. Photoch. Photobio. A: Chem.* **2005**, *176*, 1-3, 199-207.
47. Fortner, E. C.; Zhao, J.; Zhang, R. Development of ion drift-chemical ionization mass spectrometry. *Anal. Chem.* **2004**, *76*, 18, 5436-5440.
48. Zheng, J.; Khalizov, A.; Wang, L.; Zhang, R. Atmospheric pressure-ion drift chemical ionization mass spectrometry for detection of trace gas species. *Anal. Chem.* **2010**, *82*, 17, 7302-7308.
49. Xu, W.; Gomez-Hernandez, M.; Guo, S.; Secrest, J.; Marrero-Ortiz, W.; Zhang, A.L.; Zhang, R. Acid-catalyzed reactions of epoxides for atmospheric nanoparticle growth. *J. Am. Chem. Soc.* **2014**, *136*, 44, 15477-15480.
50. Ma, Y.; Brooks, S. D.; Vidaurre, G.; Khalizov, A. F.; Wang, L.; Zhang, R. Rapid modification of cloud-nucleating ability of aerosols by biogenic emissions. *Geophys. Res. Lett.* **2013**, *40*, 23, 6293-6297.
51. Lavi, A.; Segre, E.; Gomez-Hernandez, M.; Zhang, R.; Rudich, Y. Volatility of Atmospherically Relevant Alkylammonium Carboxylate Salts. *J. Phys. Chem.* **2015**, *119*, 19, 4336-4346.
52. Levy, M.; Zhang, R.; Zheng, J.; Zhang, A.; Xu, W.; Gomez-Hernandez, M.; Wang, Y.; Olaguer, E. Measurements of nitrous acid (HONO) using ion drift-

- chemical ionization mass spectrometry during the 2009 SHARP field campaign. *Atmos. Environ.* **2014**, *94*, 231-240.
53. Zhao, J.; Zhang, R. Proton transfer reaction rate constants between hydronium ion ( $\text{H}_3\text{O}^+$ ) and volatile organic compounds. *Atmos. Environ.* **2004**, *38*, 14, 2177-2185.
54. Morrison, R.T.; Boyd, R. N. *Organic Chemistry*. 6th. ed. Prentice Hall: New Jersey, **1992**.
55. Molina, M. J.; Rowland, F. S. Stratospheric sink for chlorofluoromethanes - chlorine atomic-catalyzed destruction of Ozone. *Nature* **1974**, *249*, 28, 810-812.
56. Molina, M. J.; Zhang, R.; Broekhuizen, K.; Lei, W.; Navarro, R.; Molina, L.T. Experimental study of intermediates from OH-initiated reactions of toluene. *J. Am. Chem. Soc.* **1999**, *121*, 43, 10225-10226.
57. Molina, M. J.; Ivanov, A. V.; Trakhtenberg, S.; Molina, L. T. Atmospheric evolution of organic aerosol. *Geophys. Res. Lett.* **2004**, *31*, L22104.
58. Molina, M. J.; Zhang, R.; Wooldridge, P. J.; McMahon, J. R.; Kim, J. E.; Chang, H. Y.; Beyer, K. D. Physical-Chemistry of the  $\text{H}_2\text{SO}_4/\text{HNO}_3/\text{H}_2\text{O}$  system - implications for polar stratospheric clouds. *Science* **1993**, *261*, 5127, 1418-1423.
59. Molina, M. J.; Molina, L.T.; Zhang, R.; Meads, R.; Spencer, D. The Reaction Of  $\text{ClONO}_2$  With Hcl On Aluminum Oxide. *Geophys. Res. Lett.* **1997**, *24*, 13, 1619-1622.
60. Solomon, S.; Qin, D.; Manning, M.; Alley, R. B.; Berntsen, T. et al. Technical Summary. In: Climate Change 2007: The Physical Science Basis. *Contribution of*

*Working Group I to the Fourth Assessment Report of the Intergovernmental Panel on Climate Change*. Cambridge University Press. Cambridge, United Kingdom and New York, NY. USA. 2007.

61. Wang, L.; Lal, V.; Khalizov, A. F.; Zhang, R. Heterogeneous chemistry of alkylamines with sulfuric acid: Implications for atmospheric formation of alkylammonium sulfates. *Environ. Sci. Technol.* **2010**, *44*, 7, 2461-2465.
62. Lal, V.; Khalizov, A. F.; Lin, Y.; Galvan, M. D.; Connell, B. T.; Zhang, R. Heterogeneous reactions of epoxides in acidic media. *J. Phys. Chem. A.* **2012**, *116*, 24, 6078-6090.
63. Zhao, J.; Levitt, N. P.; Zhang, R.; Chen, J. Heterogeneous reactions of methylglyoxal in acidic media: Implications for Secondary Organic Aerosol formation. *Environ. Sci. Technol.* **2006**, *40*, 24, 7682-7687.
64. Zhao, J.; Levitt, N. P.; Zhang, R. Heterogeneous chemistry of octanal and 2, 4-hexadienal with sulfuric acid. *Geophys. Res. Lett.* **2005**, *32*, 9, L09802.
65. Jang, M.; Carroll, B.; Chandramouli, B.; Kamens, R. M. Particle growth by acid-catalyzed heterogeneous reactions of organic carbonyls on preexisting aerosols. *Environ. Sci. Technol.* **2003**, *37*, 17, 3828-3837.
66. Lei, W.; Derecskei-Kovacs, A.; Zhang, R. Ab initio study of OH addition reaction to isoprene. *J. Chem. Phys.* **2000**, *113*, 13, 5354-5360.
67. Cocker, D.R. III.; Mader, B. T.; Kalberer, M.; Flagan, R. C.; Seinfeld, J. H. The effect of water on gas-particle partitioning of Secondary Organic Aerosol: II. m-

- xylene and 1,3,5-trimethylbenzene photooxidation systems. *Atmos. Environ.* **2001**, *35*, 35, 6073-6085.
68. Kleindienst, T. E.; Conner, T. S.; McIver, C. D.; Edney, E. O. Determination of Secondary Organic Aerosol products from the photooxidation of toluene and their implications in ambient PM<sub>2.5</sub>. *J. Atmos. Chem.* **2004**, *47*, 1, 79-100.
69. Shepson, P. B.; Edney, E. O.; Corse, E. W. Ring fragmentation reactions on the photooxidations of toluene and o-xylene. *J. Phys. Chem.* **1984**, *88*, 18, 4122-4126.
70. Motta, F.; Higo, G.; Tonachini, G. Oxidative degradation of benzene in the troposphere. Theoretical mechanistic study of the formation of unsaturated dialdehydes and dialdehyde Epoxides. *J. Phys. Chem. A.* **2002**, *106*, 17, 4411-4422.
71. Suh, I.; Zhang, D.; Zhang, R.; Molina, L. T.; Molina, M. J. Theoretical study of OH addition reaction to toluene. *Chem. Phys. Lett.* **2002**, *364*, 5-6, 454-462.
72. Suh, I.; Zhang, R.; Molina, L.T.; Molina, M. J. Oxidation mechanism of aromatic peroxy and bicyclic radicals from OH-toluene reactions. *J. Am. Chem. Soc.* **2003**, *125*, 41, 12655-12665.
73. Yu, J.; Jeffries, H. E.; Le Lacheur, R. M. Identifying airborne carbonyl compounds in isoprene atmospheric photooxidation products by Their PFBHA oximes using a Gas Chromatography/Ion Trap Mass Spectrometry. *Environ. Sci. Technol.* **1995**, *29*, 8, 1923-1932.



74. Spaulding, R. S.; Schade, G. W.; Goldstein, A. H.; Charles, M. J. Characterization of secondary atmospheric photooxidation products: Evidence for biogenic and anthropogenic sources. *J. Geophys. Res.* **2003**, *108*, D8, 4247.
75. Munger, J. W.; Jacob, D. J.; Danube, B. C.; Horowitz, L. W.; Keene, W. C.; Heikes, B. G. Formaldehyde, Glyoxal, And Methylglyoxal In Air And Cloudwater At A Rural Mountain Site In Central Virginia. *J. Geophys. Res.* **1995**, *100*, D5, 9325-9333.
76. Ho, S. S. H.; Yu, J. Z. Feasibility Of Collection And Analysis Of Airborne Carbonyls By On-Sorbent Derivatization And Thermal Desorption. *Anal. Chem.* **2002**, *74*, 6, 1232-1240.
77. Volkamer, R.; Molina, L. T.; Molina, M. J.; Shirley, T.; Brune, W. H. DOAS Measurement Of Glyoxal As An Indicator For Fast VOC Chemistry In Urban Air. *Geophys. Res. Lett.* **2005**, *32*, L08806.
78. Fu, T. M.; Jacob, D. J.; Wittrock, F.; Burrows, J. P.; Vrekoussis, M.; Henze, D. K. Global Budgets Of Atmospheric Glyoxal And Methylglyoxal, And Implications For Formation Of Secondary Organic Aerosols. *J. Geophys. Res.* **2008**, *113*, D15, 1984-2012.
79. Volkamer, R.; Martini, F. S.; Molina, L. T.; Salcedo, D.; Jimenez, J. L.; Molina, M. J. A Missing Sink For Gas-Phase Glyoxal In Mexico City: Formation Of Secondary Organic Aerosol. *Geophys. Res. Lett.* **2007**, *34*, L19807.

80. Ip, H.S.S.; Huang, X. H. H.; Yu, J. Z. Effective Henry's Law Constants Of Glyoxal, Glyoxylic Acid, And Glycolic Acid. *Geophys. Res. Lett.* **2009**, *36*, L01802.
81. Kampf, C. J.; Waxman, E. M.; Slowik, J. G.; Dommen, J.; Pfaffenberger, L.; Praplan, A. P.; Prévôt, A. S. H.; Baltensperger, U.; Hoffman, T.; Volkamer, R. Effective Henry's Law Partitioning And The Salting Constant Of Glyoxal In Aerosols Containing Sulfate. *Environ. Sci. Technol.* **2013**, *47*, 9, 4236-4244.
82. De Haan, D. O.; Corrigan, A. L.; Smith, K. W.; Stroik, D. R.; Turley, J. J.; Lee, F. E.; Tolbert, M. A.; Jimenez, J. L.; Cordova, K. E.; Ferrell, G. R. Secondary Organic Aerosol-Forming Reactions Of Glyoxal With Amino Acids. *Environ. Sci. Technol.* **2009**, *43*, 8, 2818-2824.
83. Carlton, A. G.; Turpin, B. J.; Altieri, K. E.; Seitzinger, S.; Reff, A.; Lim, H. J.; Ervens, B. Atmospheric Oxalic Acid And SOA Production From Glyoxal: Results Of Aqueous Photooxidation Experiments. *Atmos. Environ.* **2007**, *41*, 35, 7588-7602.
84. Corrigan, A. L.; Hanley, S. W.; De Haan, D. O. Uptake Of Glyoxal By Organic And Inorganic Aerosol. *Environ. Sci. Technol.* **2008**, *42*, 12, 4428-4433.
85. Schwier, A. N.; Sareen, N.; Mitroo, D.; Shapiro, E. L.; McNeill, V. F. Glyoxal-Methyglyoxal Cross-Reactions In Secondary Organic Aerosol Formation. *Environ. Sci. Technol.* **2010**, *44*, 16, 6174-6182.

86. Liggio, J.; Li, S. M.; McLaren, R. Heterogeneous reactions of glyoxal on particulate matter: Identification of acetals and sulfate esters. *Environ. Sci. Technol.* **2005**, *39*, 6, 1532-1541.
87. Zhou, S.; Gonzalez, L.; Leithead, A.; Finewax, Z.; Thalman, R.; Vlasenko, A.; Vagle, S.; Miller, L. A.; Li, S. M.; Bureekul, S.; Furutani, H.; Uematsu, M.; Volkamer, R.; Abbatt, J. Formation of gas-phase carbonyls from heterogeneous oxidation of polyunsaturated fatty acids at the air-water interface and of the sea surface microlayer. *Atmos. Chem. Phys.* **2014**, *14*, 1371-1384.
88. Liggio, J.; Li, S.-M.; McLaren, R. Reactive uptake of glyoxal by particulate matter. *J. Geophys. Res.* **2005**, *110*, D10.
89. Schweitzer, F.; Magi, L.; Mirabel, P.; George, C. Uptake rate measurements of methanesulfonic acid and glyoxal by aqueous droplets. *J. Phys. Chem. A.* **1998**, *102*, 3, 593-600.
90. Betterton, E. A. Henry's law constants of soluble and moderately soluble organic gases: Effects of aqueous phase chemistry. *Adv. Environ. Sci. Technol.* **1992**, *24*, 8, 1-50.
91. Zhang, R.; Jayne, J. T.; Molina, M. J. Heterogeneous interactions of nitryl hypochlorite and hydrogen chloride with sulfuric acid tetrahydrate: Implications for the stratosphere. *J. Phys. Chem.* **1994**, *98*, 3, 867-874.
92. Zhang, R.; Leu, M. T.; Keyser, L. F. Heterogeneous chemistry of HONO on liquid sulfuric acid: A new mechanism of chlorine activation on stratospheric sulfate aerosols. *J. Phys. Chem.* **1996**, *100*, 1, 339-345.

93. Klassen, J. K.; Lynton, J.; Golden, D. M.; Williams, L. R. Solubility of acetone in low-temperature (210-240 K) sulfuric acid solutions. *J. Geophys. Res.* **1999**, *104*, D21, 26355-26361.
94. Zhang, R.; Wooldridge, P.J.; Abbatt, J.P.D.; Molina, M.J. Physical chemistry of the H<sub>2</sub>SO<sub>4</sub>/H<sub>2</sub>O binary system at low temperatures: Implications for the stratosphere. *J. Phys. Chem.* **1993**, *97*, 28, 7351-7358.
95. Zhang, R.; Wooldridge, P.J.; Abbatt, J.P.D.; Molina, M.J. Vapor pressure measurements for the H<sub>2</sub>SO<sub>4</sub>/HNO<sub>3</sub>/H<sub>2</sub>O and H<sub>2</sub>SO<sub>4</sub>/HCl/H<sub>2</sub>O systems: Incorporation of stratospheric acids into background sulfate aerosols. *J. Phys. Chem.* **1993**, *97*, 8541-8548.
96. Kroll, J. H.; Ng, N. L.; Murphy, S. M.; Varutbangkul, V.; Flagan, R. C.; Seinfeld, J. H. Chamber studies of secondary organic aerosol growth by reactive uptake of simple carbonyl compounds. *J. Geophys. Res.* **2005**, *110*, D23.
97. Xu, W.; Guo, S.; Gomez-Hernandez, M.; Lev, M.; Secret, J.; Marrero-Ortiz, W.; Zhang, A. L.; Collins, D. R.; Zhang, R. Cloud forming potential of oligomers relevant to Secondary Organic Aerosols. *Geophys. Res. Lett.* **2014**, *41*, 18, 6538-6545.
98. Fan, J.; Zhang, R.; Li, G.; Tao, W.-K. Effects of aerosols and relative humidity on cumulus clouds. *J. Geophys. Res.* **2007**, *112*, D14204, doi:10.1029/2006JD008136.
99. Lei, W. F.; Zhang, R. Y.; McGivern, W. S.; Derecskei-Kovacs, A.; North, S. W. Theoretical study of isomeric branching in the isoprene-OH reaction:

- implications to final product yields in isoprene oxidation. *Chem. Phys. Lett.* **2000**, *326*, 1-2, 109-114.
100. Zhang, R. Y.; Suh, I.; Lei, W.; Clinkenbeard, A. D.; North, S. W. Kinetic studies of OH-initiated reactions of isoprene. *J. Geophys. Res.* **2000**, *105*, D20, 24627-24635.
101. Yu, Y.; Ezell, M. J.; Zelenyuk, A.; Imre, D.; Alexander, L.; Ortega, J.; D'Anna, B.; Harmon, C. W.; Johnson, S. N.; Finlayson-Pitts, B. J. Photooxidation of alpha-pinene at high relative humidity in the presence of increasing concentrations of NO<sub>x</sub>. *Atmos. Environ.* **2008**, *42*, 20, 5044-5060.
102. Pankow, J. F. An absorption model of gas/particle partitioning of organic compounds in the atmosphere. *Atmos. Environ.* **1994**, *28*, 2, 185-188.
103. Pankow, J. F. An absorption model of the gas/aerosol partitioning involved in the formation of secondary organic aerosol. *Atmos. Environ.* **1994**, *28*, 2, 189-193.
104. Donahue, N. M.; Robinson, A. L.; Stanier, C. O.; Pandis, S. N. Coupled Partitioning, Dilution, and Chemical Aging of Semivolatile Organics. *Environ. Sci. Technol.* **2006**, *40*, 8, 2635-2643.
105. Gomez, M. E.; Lin, Y.; Guo, S.; Zhang, R. Heterogeneous Chemistry of Glyoxal on Acidic Solutions. An Oligomerization Pathway for Secondary Organic Aerosol Formation. *J. Phys. Chem. A.* **2015**, *119*, 19, 4457-4463.
106. Wang, L.; Xu, W.; Khalizov, A.F.; Zheng, J.; Qiu, Q.; Zhang, R. Laboratory investigation on the role of organics in atmospheric nanoparticle growth. *J. Phys. Chem.* **2011**, *115*, 32, 8940-8947

107. Paulot, F.; Wunch, D.; Crounse, J. D., et al. Importance of secondary sources in the atmospheric budgets of formic and acetic acids. *Atmos. Chem. Phys.* **2011**, *11*, 5, 1989-2013.
108. Martin, R.; Westberg, H.; Allwine, E., et al. Measurement of isoprene and its atmospheric oxidation products in a central Pennsylvania deciduous forest. *J. Atmos. Chem.* **1991**, *13*, 1, 1-32.
109. Talbot, R. W.; Beecher, K. M.; Harriss, R. C., et al. Atmospheric Geochemistry of Formic and Acetic Acids at a Mid-Latitude Temperate Site. *J Geophys Res - Atmos.* **1988**, *93*, D2, 1638-1652.
110. Chebbi, A.; Carlier, P. Carboxylic acids in the troposphere, occurrence, sources, and sinks: A review. *Atmos. Environ.* **1996**, *30*, 24, 4233-4249.
111. Kesselmeier, J.; Bode, K.; Gerlach, C., et al. Exchange of atmospheric formic and acetic acids with trees and crop plants under controlled chamber and purified air conditions. *Atmos. Environ.* **1998**, *32*, 10, 1765-1775.
112. Graedel, T.; Eisner, T. Atmospheric formic acid from formicine ants: a preliminary assessment. *Tellus B.* **1988**, *40*, 5, 335-339.
113. Prenni, A.J.; DeMott, P.J.; Kreidenweis, S.; Sherman, D.E.; Russell, L. M.; Ming, Y. The effects of low molecular weight dicarboxylic acids on cloud formation. *J. Phys. Chem. A.* **2001**, *105*, 50, 11240-11248.
114. Khwaja, H.A. Atmospheric concentrations of carboxylic acids and related compounds at a semiurban site. *Atmos. Environ.* **1995**, *29*, 1, 127-139.

115. Kawamura, K.; Ikushima, K. Seasonal changes in the distribution of dicarboxylic acids in the urban atmosphere. *Environ. Sci. Technol.* **1993**, *27*, 10, 2227-2235.
116. Kawamura, K.; Kaplan, I. R. Motor exhaust emissions as a primary source for dicarboxylic acids in Los Angeles ambient air. *Environ. Sci. Technol.* **1987**, *21*, 1, 105-110.
117. Sempéré, R.; Kawamura, K. Comparative distributions of dicarboxylic acids and related polar compounds in snow, rain and aerosols from urban atmosphere. *Atmos. Environ.* **1994**, *28*, 3, 449-459.
118. Kerminen, V.; Ojanen, C.; Pakkanen, T.; Hillamo, R.; Aurela, M.; Meriläinen, J. Low-molecular-weight dicarboxylic acids in an urban and rural atmosphere. *J. Aerosol Sci.* **2000**, *31*, 3, 349-362.
119. Kawamura, K.; Kasukabe, H.; Barrie, L.A. Source and reaction pathways of dicarboxylic acids, ketoacids and dicarbonyls in arctic aerosols: One year of observations. *Atmos. Environ.* **1996**, *30*, 10-11, 1709-1722.
120. Xu, W.; Zhang, R. Theoretical investigation of interaction of dicarboxylic acids with common aerosol nucleation precursors. *J. Phys. Chem. A.* **2012**, *116*, 18, 4539-4550.
121. Ge, X.; Wexler, A. S.; Clegg, S. L. Atmospheric amines-Part I. A review. *Atmospheric Environment.* **2011**, *45*, 3, 524-546.
122. Yu, F.; Luo, G. Modeling of gaseous methylamines in the global atmosphere: Impacts of oxidation and aerosol uptake. *Atmos. Chem. Phys.* **2014**, *14*, 22, 12455–12464,.

123. Angelino, S.; Suess, D. T.; Prather, K. A. Formation of Aerosol Particles from Reactions of Secondary and Tertiary Alkylamines: Characterization by Aerosol Time-of-Flight Mass Spectrometry. *Environ. Sci. Technol.* **2001**, *35*, 15, 3130-3138.
124. Silva, P. J.; Erupe, M. E.; Price, D.; Elias, J.; G. J. Malloy, Q.; Li, Q.; Warren, B.; Cocker, D. R. Trimethylamine as Precursor to Secondary Organic Aerosol Formation via Nitrate Radical Reaction in the Atmosphere. *Environ. Sci. Technol.* **2008**, *42*, 13, 4689-4696.
125. Sorooshian, A.; Murphy, S. M.; Hersey, S.; Gates, H.; Padro, L. T.; Nenes, A.; Brechtel, F. J.; Jonsson, H.; Flagan, R. C.; Seinfeld, J. H. Comprehensive Airborne Characterization of Aerosol from a Major Bovine Source. *Atmos. Chem. Phys.* **2008**, *8*, 3, 10415-10479.
126. Wang, X.; Gao, S.; Yang, X.; Chen, H.; Chen, J.; Zhuang, G.; Surratt, J. D.; Chan, M. N.; Seinfeld, J. H. Evidence for High Molecular Weight Nitrogen-Containing Organic Salts in Urban Aerosols. *Environ. Sci. Technol.* **2010**, *44*, 12, 4441-4446.
127. Yu, H.; McGraw, R.; Lee, S.-H. Effects of Amines on Formation of Sub-3 nm Particles and Their Subsequent Growth. *Geophys. Res. Lett.* **2012**, *39*, 2, L02807.
128. Clegg, S.L.; Qiu, C.; Zhang, R. The deliquescence behaviour, solubilities, and densities of aqueous solutions of five methyl- and ethyl-aminium sulphate salts. *Atmos. Environ.* **2013**, *73*, 145-158.



129. Qiu, C.; Zhang, R. Physiochemical properties of alkylaminium sulfates: Hygroscopicity, thermostability, and density. *Environ. Sci. Technol.* **2012**, 46, 8, 4474-4480.
130. Xu, W.; Zhang, R. A theoretical study of hydrated molecular clusters of amines and dicarboxylic acids. *J. Chem. Phys.* **2013**, 139, 6, 064312, doi:10.1063/1.4817497.
131. Dawson, M. L.; Varner, M. E.; Perraud, V.; Ezell, M. J.; Gerber, R. B.; Finlayson-Pitts, B. J. Simplified mechanism for new particle formation from methanesulfonic acid, amines, and water via experiments and ab initio calculations. *Proc. Natl. Acad. Sci. U.S.A.* **2012**, 109, 46, 18719-18724.
132. Smith, J.; Barsanti, K. C.; Friedli, H. R.; Ehn, M.; Kulmala, M.; Collins, D. R.; Scheckman, J. H.; Williams, B. J.; McMurry, P. H. Observations of aminium salts in atmospheric nanoparticles and possible climatic implications. *Proc. Natl. Acad. Sci. USA.* **2010**, 107, 15, 6634-6639.
133. Barsanti, K.C.; McMurry, P. H.; Smith, J. N. The potential contribution of organic salts to new particle formation. *Atmos. Chem. Phys.* **2009**, 9, 9, 2949-2957.
134. Lloyd, J. A.; Heaton, K. J.; Johnston, M. V. Reactive uptake of trimethylamine into ammonium nitrate particles. *J. Phys. Chem. A.* **2009**, 113, 17, 4840-4843.
135. Bzdek, B. R.; Ridge, D. P.; Johnston, M. V. Amine exchange into ammonium bisulfate and ammonium nitrate nuclei. *Atmos. Chem. Phys.* **2010**, 10, 8, 3495-3503.

136. Bzdek, B. R.; Ridge, D. P.; Johnston, M. V. Size-dependent reactions of ammonium bisulfate clusters with dimethylamine. *J. Phys. Chem. A.* **2010**, *114*, 43, 11638-11649.
137. Liu, Y.; Ma, Q.; He, H. Heterogeneous uptake of amines by citric acid and humic acid. *Environ. Sci. Technol.* **2012**, *46*, 11112-11118.
138. Dinar, E.; Antilla, T.; Rudich, Y. CCN activity and hygroscopic growth of organic aerosols following reactive uptake of ammonia. *Environ Sci Technol.* **2008**, *42*, 3, 793-799.
139. Prenni, A. J.; DeMott, P. J.; Kreidwenweis, S. M. Water uptake of internally mixed particles containing ammonium sulfate and dicarboxylic acids. *Atmos Environ.* **2003**, *37*, 30, 4243-4251.
140. Cruz, C. N.; Pandis, S. N. Deliquescence and hygroscopic growth of mixed inorganic-organic atmospheric aerosol. *Environ. Sci. Technol.* **2000**, *34*, 20, 4313-4319.
141. Suda, S. R.; Petters, M.D.; Yeh, G. K.; Strollo, C.; Matsunaga, A.; Faulhaber, A.; Ziemann, P.J.; Prenni, A. J.; Carrico, C. M.; Sullivan, R. C.; Kreidwenweis, S.M. Influence of functional groups on organic aerosol cloud condensation nucleus activity. *Environ Sci Technol.* **2014**, *48*, 17, 10182–10190.
142. Petters, M. D.; Kreidenweis, S. M. A single parameter representation of hygroscopic growth and cloud condensation nucleus activity. *Atmos Chem Phys.* **2007**, *7*, 8, 1961-1971.

143. Kumar, P.; Nenes, A.; Sokolik, I. N. Importance of adsorption for CCN activity and hygroscopic properties of mineral dust aerosol. *Geophys. Res. Lett.* **2009**, *36*, 24, L24804, 1-6.
144. Wang, Y.; Khalizov, A.; Levy, M.; Zhang, R. New Directions: Light absorbing aerosols and their atmospheric impacts. *Atmos. Environ.* **2013**, *81*, 713-715.
145. Guo, S.; Hu, M.; Zamora, M.L.; Peng, J.; Shang, D.; Zheng, J.; Du, Z.; Wu, Z.; Shao, M.; Zeng, L.; Molina, M.J.; Zhang, R. Elucidating severe urban haze formation in China. *Proc. Natl. Acad. Sci. USA* **2014**, *111*, 49, 17373–17378.
146. Dentener, F.; Kinne, S.; Bond, T.; Boucher, O.; Cofala, J. et al. Emissions of primary aerosol and precursor gases for the years 2000 and 1750, prescribed data sets for AeroCom. *Atmos. Chem. Phys.* **2006**, *6*, 4321-4344.
147. Boucher, O.; Moulin, C.; Belviso, S.; Aumont, O.; Bopp, L. et al. DMS atmospheric concentrations and sulphate aerosol indirect radiative forcing: a sensitivity study to the DMS source representation and oxidation. *Atmos. Chem. Phys.* **2003**, *3*, 1, 49-65.
148. Lamarque, J. F.; Bond, T. C.; Eyring, V.; Granier, C.; Heil, A. et al. Historical (1850-2000) gridded anthropogenic and biomass burning emissions of reactive gases and aerosols: methodology and application. *Atmos. Chem. Phys.* **2010**, *10*, 15, 7017-7039.
149. Klimont, Z.; Smith, S. J.; Cofala, J. The last decade of global anthropogenic sulfur dioxide: 2000-2011 emissions. *Environ, Res. Lett.* **2013**, *8*, 1, 014003.

150. Schneidemesser, E. V.; Monks, P. S.; Allan, J. D.; Bruhwiler, L.; Forster, P. et al. Chemistry and the linkages between air quality and climate change. *Chem. Rev.* **2015**, 115, 10, 3856–3897.
151. Rohde, H.; Crutzen, P.; Vanderpol, A. Formation of sulfuric and nitric-acid in the atmosphere during long-range transport. *Tellus* **1981**, 33, 2, 132-141.
152. Pandis, S. N.; Seinfeld, J. H.; Mathematical modeling of acid deposition due to radiation fog. *J. Geophys. Res.* **1989**, 94, D10, 12911-12923.
153. Behra, P.; Sigg, L.; Werner, S. Dominating influence of NH<sub>3</sub> on the oxidation of aqueous SO<sub>2</sub>: The coupling of NH<sub>3</sub> and SO<sub>2</sub> in atmospheric water. *Atmos. Environ.* **1989**, 23, 12, 2691-2707.
154. Lee, Y, N.; Schwartz, S. E.; In *Precipitation Scavenging, Dry Deposition and Resuspension*; Pruppacher, H. R.; Semonin, R. G.; Slinn, W. G. N. eds. Elsevier: New York, **1983**; Vol. 1.
155. Occupational Safety & Health Administration. United States Department of Labor. *OSHA Permissible Exposure Limit (PEL)-General Industry*. 29 CFR 1910.1000 Table Z-1.  
[https://www.osha.gov/dts/chemicalsampling/data/CH\\_268500.html](https://www.osha.gov/dts/chemicalsampling/data/CH_268500.html)

## APPENDIX

### VITA

Mario E. Gomez Hernandez was born in Guatemala City, Guatemala in 1980. He received a Bachelor of Science degree in chemistry in 2003 from Texas A&M University-Kingsville. He also received a Master of Science degree with focus on organic chemistry at Texas A&M-Kingsville in 2006. He joined the graduate program at Texas A&M University in College Station, Texas in the year 2006 earning a Master of Science degree in 2011. He joined the laboratory of Prof. Renyi Zhang in the summer of 2011 to study the molecular composition, formation, and physicochemical properties of secondary organic aerosols through mass spectrometry and other techniques. Mario has participated in several projects resulting in various publications collaborating with colleagues from Israel and China. He married Heydi Morales on July 5<sup>th</sup>. 2014 in Quetzaltenango, Guatemala. Mario enjoys reading military history, comparative theology, and watching sports. He can be reached at the Advanced Mass Spectrometry Facility of the Department of Chemistry and Biochemistry at Florida International University, Miami, Florida, Modesto A. Maidique Campus, CP-174 11200 Southwest 8<sup>th</sup> Street Miami, FL 33199.

### **Publications**

**Heterogeneous Chemistry of Glyoxal on Acidic Solutions -An Oligomerization Pathway for Secondary Organic Aerosol Formation.**

Gomez Hernandez, Mario; Lin, Yun; Guo, Song; Zhang, Renyi.  
*J. Phys. Chem. A.* 118. DOI: 10.1021/jp509916r. **2015.**

**On the Volatility of Atmospherically Relevant Alkylammonium Carboxylate Salts.** Lavi, Avi; Segre, Enrico; Gomez Hernandez, Mario; Zhang, Renyi; Rudich, Yinon. *J. Phys. Chem. A*. 118. DOI: 10.1921/jp2014-07320v. **2015.**

**Acid-Catalyzed Reactions of Epoxides for Atmospheric Nanoparticle Growth.** Xu, Wen; Gomez Hernandez, Mario; Guo, Song; Secret, Jeremiah; Marrero-Ortiz, Wilmarie, Zhang, Annie, L; Zhang, Renyi. *J. Am. Chem. Soc.* 136, 15477-15480. DOI: 10.1021/ja508989a. **2014.**

**Cloud Forming Potential of Oligomers Relevant to Secondary Organic Aerosols.**

Xu, Wen; Guo, Song; Gomez Hernandez, Mario; Levy, Misti; Secret, Jeremiah; Marrero Ortiz, Wilmarie; Zhang, Annie, L.; Collins, Donald; Zhang, Renyi. *Geophys. Res. Lett.* 41, 6538-6545. DOI:10.1029/2014GL061040. **2014.**

**Measurements of Nitrous Acid (HONO) Using Ion-Drift Chemical Ionization Mass Spectrometry During the 2009 SHARP Field Campaign.**

Levy, Misti; Zhang, Renyi; Zheng, Jun; Zhang, Annie; Xu, Wen; Gomez Hernandez, Mario; Wang, Yuan; Olaguier, Eduardo. *Atmos. Environ.* 94, 231-240. **2014.**

**Thermal Desorption Ion Drift Chemical Ionization Mass Spectrometry for the Analysis of Nucleation to Accumulation Mode Aerosols. (In preparation) 2015.** Gomez Hernandez, Mario; Khalizov, Alexei; Xu, Wen.; Qiu, Chong; Zhang, Renyi.

**Cloud Forming Potential of Ammonium Carboxylate Aerosols. (In preparation 2015).**

Gomez Hernandez, Mario; Xu, Wen; McKeown, Megan; Taylor, Nathan; Lavi, Avi; Rudich, Yinon, Collins, Donald; Zhang, Renyi.

**Longitudinal Surface Plasmon Resonance Based Gold Nanorod Biosensors for Mass Spectrometry.**

Castellana, Edward T.; Gamez, Roberto C.; Gomez, Mario E.; Russell, David H. *Langmuir*. 26(8), 6066-6070. **2010.**

**Theoretical investigation of the proton affinity and gas-phase basicity of neutral x,y-dihydroxybenzoic (DHB) acid and its derivatives.**

Rebber BL, Halfacre JA, Beran KA, Gomez M, Beller NR, Bashir S, Giannakopoulos AE, Derrick PJ. *European Journal of Mass Spectrometry*, 276, 385-396, **2006.**